國立交通大學

材料科學與工程學系

碩士論文

突起缺陷及應力對新型矽氧氮SiO_xN_y薄膜用於有機發光二極體之水氣阻障探討

The Effects of Hillock Defect and Stress on the Moisture Resistance of Novel SiO_xN_y Passivation Layer for OLED Applications

研 究 生：陳怡臻

指導教授：呂志鵬　博士

中 華 民 國 九十七 年 六 月

突起缺陷及應力對新型矽氧氮SiO_xN_y薄膜用於有機發光二極體之水氣阻障探討

The Effects of Hillock Defect and Stress on the Moisture Resistance of Novel SiO_xN_y Passivation Layer for OLED Applications

研 究 生：陳怡臻　　Student：Yi-Jen Chen

指導教授：呂志鵬　　Advisor：Dr. Jihperng (Jim) Leu

國 立 交 通 大 學

材 料 科 學 與 工 程 學 系

碩 士 論 文

A Thesis

Submitted to Department of Materials Science and Engineering

College of Engineering

National Chiao Tung University

in partial Fulfillment of the Requirements

for the Degree of

Master

in

Materials Science and Engineering

June 2008

Hsinchu, Taiwan, Republic of China

中華民國九十七年六月

突起缺陷及應力對新型矽氧氮SiO_xN_y薄膜用於有機發光二極體之水氣阻障探討

學生:陳怡臻　　指導教授:呂志鵬 博士

國立交通大學材料與工程學系碩士班

摘要

有機發光二極體(OLED)顯示器因其擁有自體發光之能力而不需背向光源之調節，以及快速的反應時間（<10 ms)、廣視角（170°以上)、色彩逼真、優良的對比與亮度、低操作電壓(3-10 V)以及省電等優點，故在過去幾年快速成長。然而，其有機物及電極對水氣及氧氣非常敏感，在無保護的情況下，水氣及氧氣會迅速降低OLED元件的性能。在此現況下，本研究動機在尋找低成本、製程簡單且高可靠性，用於OLED的氮氧化物或氮化物基底（oxynitride or nitride）之薄膜阻障層。我們利用一套新穎的蒸鍍系統(Ar ion beam evaporation technique)進行薄膜沉積，首先探討氮氧化矽阻障層之成分組成、微觀結構及表面形貌，並且改變其基材溫度及氣體流速來探討其SiO_xN_y/Al薄膜的表面形貌及薄膜應力之影響。此外，並調查水氣阻障與薄膜缺陷(突起缺陷及Al晶界)之關係。最後,探討突起密度以及其高度對於水氣阻障能力之影響。

從實驗的結果發現氮氧化矽薄膜呈現非晶結構，其 Si: O: N 成分比例為 1: 2: 0.67。鋁薄膜呈現柱狀結構，其晶粒分布介於 50 到 100 奈米。吾人發現，Al 突起缺陷是造成阻障層高水氣穿透的主要原因，同時並提出一套突起密度及其高度的可能機制。突起密度和鋁晶粒大小有關，而凸起高度和薄膜應力有正向關係。在高基材溫度、高氣體流速的情況下，其突起缺陷密度會較少但是其高度會較高;在低基材溫度、低氣體流速的情況下，其突起缺陷密度會較多但是其高

度會較低。因此，如果使用一層阻障層的情況下，高溫高流速的阻氣能力會較低溫低流速的來的佳。但是，如果以層數為考量的話，低溫低流速因其缺限高度較低，所以只需要較少之阻障層數即可把缺陷完全癒合而高溫高流速則需較多的層數。總結來說，藉由改變鍍膜參數(氣體流量及基材溫度)來控制突起缺陷的形成，對於阻障層的阻氣能力有絕對的關係。

The Effects of Hillock Defect and Stress on the Moisture Resistance of Novel SiO_xN_y Passivation Layer for OLED Applications

Student: Yi-Jen Chen Advisor: Dr. Jihperng (Jim) Leu

Department of Materials Science and Engineering

National Chiao Tung University

Abstract

Organic light-emitting-diode displays (OLED) have gained momentum in the past few years because it was an emissive system creating its own light rather than relying on modulating a backlight. In addition, OLED possessed fast response time (<10ms, 100 times faster than TFT-LCD), wide view angle (>170°), true colors, excellent contrast ratio, brightness, low operating voltage and potentially less power consumption. However, its broad adoption has been hindered by the sensitivity of organic and electrode to the moisture and oxygen, which can quickly degrade the device performance if not properly protected. This motivated us to explore a simple, cheap, but reliable oxynitride-based thin film barrier for OLED in this study.

The composition, microstructure and morphology of SiO_xN_y barrier layers deposited by a modified Ar ion beam evaporation system were first investigated. Then, the effects of substrate temperatures (60-90 ^oC) and gas flow rates (300-480 sccm) on the morphology and stress of SiO_xN_y/Al stack were examined. In addition, the roles of defects such as hillocks and grain sizes of Al films was studied and correlated with the moisture resistance of SiO_xN_y barrier films. Finally, the moisture barrier performance in terms of hillock density and hillock height was further discussed if multiple-layered

passivation was warranted.

In this study, SiO_xN_y layers were amorphous and the composition of Si: O: N was in the ratio of 1: 2: 0.67. Al films exhibited columnar structure with grain size distribution 50 to 100 nm after the deposition of SiO_xN_y. Al hillock was found to be the culprit of high moisture permeation in the passivation layer. A model of hillock formation in SiO_xN_y/Al was proposed in this thesis to illustrate the causes for their difference in hillock density and height. The hillock density was related to the initial Al grain size, while the hillock height was primarily derived by SiO_xN_y stress. The tallest height of hillock affected greatly on the numbers of barrier layers for complete sealing of defects. Therefore, high substrate temperature and high N_2 gas flow rate deposition process yielded barrier films with less hillocks and improved moisture resistance if single layer of passivation was employed, while lower deposition temperature and low N_2 gas flow rate were preferred for least number of layers if multiple-layer structure was adopted. In summary, defect control of Al hillocks was essential for controlling the moisture barrier performance in the practical OLED stack.

Acknowledgements

得以完成本論文，首先感謝呂志鵬老師兩年來細心且認真的指導，除了研究上的幫助外，老師亦不吝於與學生分享休閒興趣，帶領我們參與馬拉松 ing、一探司馬庫斯之美等，在此向老師致上最誠摯的謝意。感謝交通大學張立教授、潘扶民教授及許鉦宗教授於口試期間，細心且親切的指正本論文疏失缺漏之處，並提供許多寶貴意見，使本論文更加完整。

在兩年的研究生活中，由衷的感謝徐國原學長不厭其煩的與我討論研究內容與問題，由於學長的幫助，使本論文能順利完成。感謝 NIP 實驗室的夥伴們，牧龍學長、昱涵學長、明義學長、幸玲學姊、泰印學長、弘恩學長、欣源學長、鈞元學長、季高學長、冠宇學長、王智同學與少農同學的照顧與指點，尉霖學長的 TEM 相助，以及尹瀅學妹、茹瑛學妹、詩雅學妹及晉誠學弟的協助與陪伴，使這兩年的研究生活不再枯燥。感謝我的朋友明慧、靜雯、全雯、文馨等人的陪伴與包容，在我心情不好的時候，給我鼓勵及安慰。感謝華映的計畫贊助，得以讓論文能順利完成。

最後，由衷的感謝我的家人及男朋友博傑，在我背後無條件的支持與關心，使我能完成這篇論文，在此向他們獻上我最深的感激。

Contents

List of Tables

List of Figures

Chapter 1 Introduction

1.1 Background

Organic light emitting devices (OLED) have gained momentum in flat-panel display in the past few years for its fast response time (<10ms), wide view angle (>170°), low operating voltage (3-10 V), excellent contrast and brightness compared to those of LCD-TFT or LED. [1] However, their device performance degraded drastically by permeated moisture and O_2 through the oxidation of the cathode and/or active OLED polymers. [2, 3] The conventional encapsulation package of the OLEDs by metal or glass lid to prevent gas permeation has been widely used with excellent result with built-in desecrator. [4] However, the weight issue and high cost associated with difficult manufacturing processes, such as the permeation of oxygen and moisture through the glue, the impossible application to flexible display using polymer substrate, and the difficulty of large area application restricted the use of metal or glass lid in the flexible OLED displays. [4] Therefore, thin film package for FOLED's application was necessitated to prevent the permeation of water vapor and oxygen practically for long service time. Although inorganic thin films like oxide- or nitride- based have been studied as barrier layers for oxygen and water vapor, these researches still showed too high water vapor transmission rate (WVTR) and oxygen transmission rate (OTR) to apply to display industries. [5, 6] Moreover, the permeation mechanism of water vapor has not been well known yet.

In general, WVTR should be lower than 10^{-6} g/m^2-day and OTR should be lower than 10^{-5} g/m^2-day in OLED's applications. Recently, Barrix^{TM}, comprised of alternating layers of polymer and ceramic film deposited in vacuum to about 3 μm, was announced by Vitex System (USA) that Barrix^{TM} layers can achieve the requirements of WVTR for OLED's applications. [7, 8] However, the cost and

thermo-mechanical integrity of such ceramic/polymer multiple-layer structure (Barrix^{TM} layer) remained a lingering problem.

For OLED passivation and packaging, the deposition temperature cannot exceed 100 ℃ in order not to degrade OLED's small molecules or polymers. However, low substrate-temperature was expected to greatly affect the microstructure, morphology (pinhole) and even the stress of barrier films because of its low atomic surface mobility and diffusion. [9] Besides, plasma damage during the passivation layer deposition shall be avoided if films deposited by sputtering or plasma-enhanced chemical vapor deposition (PECVD). Hence, evaporation techniques were often employed. But, conventional thermal evaporation often produced films with loose microstructure due to the low atom mobility. As a result, a modified Ar ion beam evaporation technique [46] was employed in this study for the deposition of light-emitting organic, Alq_3, aluminum film as cathode and moisture barrier layer for its high deposition rate and reasonable particle energy (~25 eV) reaching the surface of substrate. More importantly, the objective of this study was to develop reliable inorganic oxynitride- barrier films with low moisture permeability for the hermetic sealing of OLED packaging using a silicon oxynitride/Al/Alq_3/glass multiple-layered structure. Specifically, the composition, microstructure and morphology of barrier were investigated. Then, the effects of substrate temperature and gas flow rates on the morphology and residual stress of SiOxNy onto Al electrode were first studied. Then, the roles of defects such as hillocks and grain sizes of Al films associated with the water permeation in inorganic barrier films were investigated and discussed. Finally, the moisture barrier performance in terms of hillock density and hillock height was further discussed if multiple-layered passivation is warranted.

1.2 Overview

This thesis was organized into five chapters. Following a concise introduction in Chapter 1, Chapter 2 reviewed the OLED package, the mechanisms of OLED device degradation, methodologies for measuring water vapor transmission rate (WVTR), and microstructure of thin films deposited at various temperature and pressures. Chapter 3 described the modified Ar ion beam evaporation system, sample preparation, experimental procedures, instrumentation and methodologies for characterizing the composition of SiO_xN_y passivation layer, Al hillock, its density, and height, and the thermal stress of SiO_xN_y/Al. Chapter 4 described key results and discussion. Specifically, the relationship between moisture permeation and defects such as hillock was investigated. The mechanism for the formation of hillocks and the root-causes for different hillock density or hillock height were examined and proposed. Then key results and conclusion of this thesis were summarized in Chapter 5.

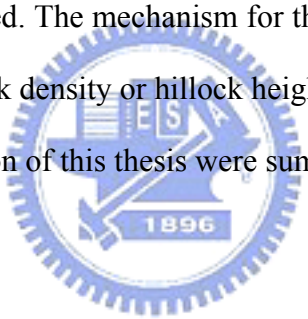

Chapter 2 Literature Review

2.1 Introduction of OLED

The next great emerging technology in the display industry was expected to come from organic light-emitting-diode (OLED). [12] A typical OLED device structure was shown in Fig. 2.1, in which organic material such as Alq_3 was presented in the form of thin film with a thickness not exceeding the depth of the ink on the paper. OLED have gained momentum in the past few years because it was an emissive system creating its own light rather than relying on modulating a backlight. In addition, OLED possessed fast response time (<10 ms), wide view angle (>170°), true colors, excellent contrast ratio, brightness, low operating voltage (3-10 V) and potentially less power consumption compared to those of LCD or LED. [1] As a result, OLED had the opportunity to replace LED or LCD in display industry. [1] However, its broad adoption has been hindered by several issues; namely (1) poor production yields which makes the product not cost attractive and deter investments and (2) device lifetime and reliability due to its sensitive to moisture and oxygen, which can quickly degrade the device performance and produce the black spots if unprotected. [2, 3]

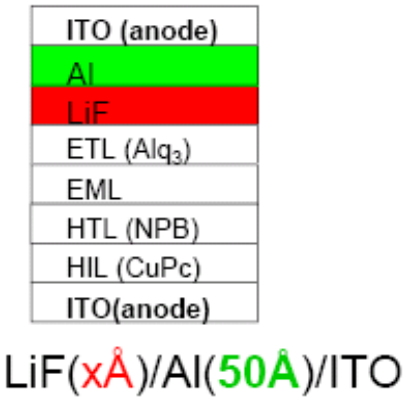

Figure 2.1 The film stack and structure of OLED device.

2.1.1 Mechanisms of Degradation

Although organic light-emitting diodes (OLEDs) had many above-mentioned advantages, the short lifetime was still a critical issue to be addressed. Many mechanisms have been proposed and reported for the decay in luminance, ranging from crystallization of the organic molecules,[13, 14] decomposition of Alq_3 molecules, [15] delamination at the cathode/Alq_3 interface, [13, 16, 17] and electrochemical reactions at the organic/electrode interfaces. [17, 18]

H. Aziz *et al.* [13] proposed the Alq_3 molecules became crystalline clusters by exposing to humidity and delamination occurred between cathode/Alq_3 interface because the crystalline Alq_3 clusters was thicker than the surrounding amorphous regions and lead the cathode/Alq_3 contact isolated. F. Papadimitrakopoulos *et al.* [15] suggested a series of probable reaction for the failure of Alq_3-based OLEDs as shown in Fig.2.2. Reaction (1) showed water acts as a catalyst to hydrolyze Alq_3 to become freed 8-hydroxyquinoline (8-Hq) and then (2) an oxidative condensation reacted with yielding a nonemissive polymeric byproduct.

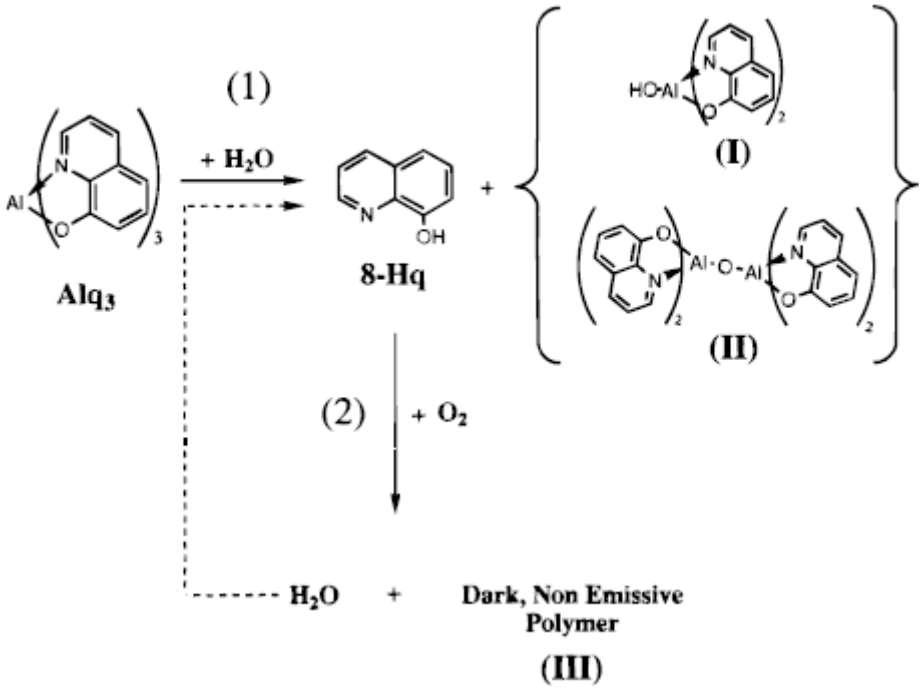

Figure 2.2 Scheme of (1) Trans-Complexation of 8-Hq with Water in the Alq_3

Complex and (2) Oxidative Polymerization of 8-Hq. [15]

M. Schaer *et al.* [17] presented two different degradation mechanisms under moisture and oxygen environments as shown in Figs.2.3 (a) and (b), respectively. Fig.2.3 (a) showed water vapor entered from the defects, such as cracks, pinholes etc. and diffused to the cathode/organic interface. When the device was working, water was then reduced at the cathode and yielded hydrogen gas. The electrochemical reduction was:

$$2H_2O+2e^- \rightarrow H_2+2OH^- \quad (2.1)$$

Then, the bubbles were formed by the evolving hydrogen gas and the organic/electrode interfaces were separated. In contrast, Fig. 2.3 (b) showed oxygen enters from the defects and diffuses to the cathode/organic interface. As the metal layer was oxidized at the cathode/organic interface, the molecular volume which increased of the oxide led to interface delamination.

In summary, organic layers and metal cathodes of OLEDs were sensitive to moisture and oxygen, no matter what mechanism was involved. Therefore, preventing moisture and oxygen permeation in OLED was an immediate solution to extend the life time of devices.

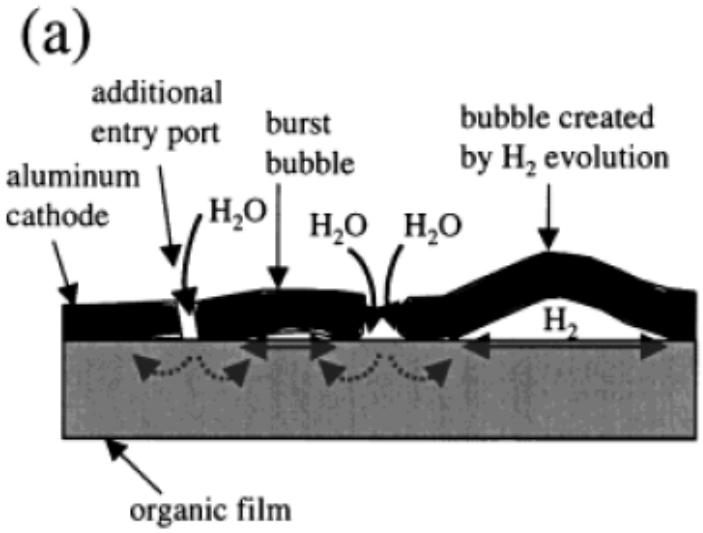

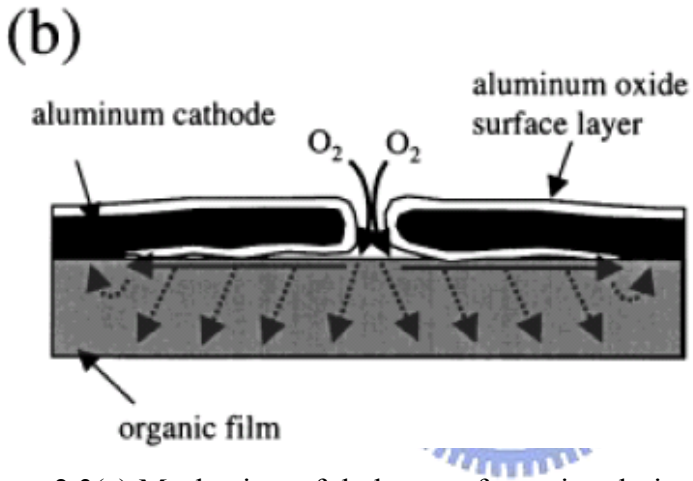

Figure 2.3(a) Mechanism of dark spots formation during operation under water vapor environment. (b) Mechanism of dark spots formation for an unbiased device under a pure oxygen atmosphere. [17]

2.1.2 Requirements of WVTR and OTR

Fig. 2.4 showed the water vapor transmission rate (WVTR) and oxygen transmission rate (OTR) required for various organic electronic devices. [19] Among these devices ranging from LCD, solar cell to OLED, the requirements for OLED application was most stringent. In general, water vapor transmission rate (WVTR) should be lower than 10^{-6} g/m^2-day and oxygen transmission rate (OTR) should be lower than 10^{-5} g/m^2-day for OLED's applications. The WVTR requirements for TFTs

or LCD were not as critical as those for OLEDs. The sensitivity to moisture and oxygen in OLED was much more than 10000 times in LCD. Apparently, oxygen and moisture permeation was a serious issue for developing OLED applications.

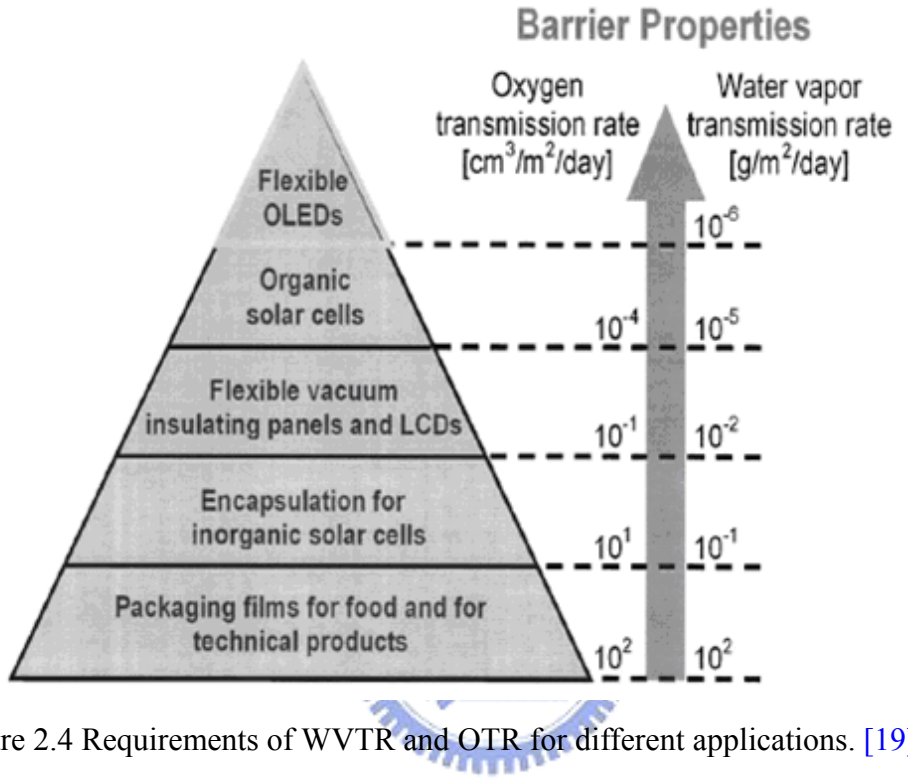

Figure 2.4 Requirements of WVTR and OTR for different applications. [19]

2.1.3 Methods for Measuring WVTR

There were many methods for measuring WVTR, which have been developed in the past few years. These methods and their detection principles were listed in Table 2.1, along with their merits and disadvantage. Among these methods, optical calcium degradation test was the most commonly used for flexible OLED's applications, which was often named as the "Ca test" or "Ca button test". This method was based on the corrosion of calcium films and subjected at a fixed temperature and humility. At the start, the calcium film was a reflecting metallic layer as shown in Fig. 2.5(a). As water and oxygen permeated into metallic calcium, calcium would convert to a transparent oxide or hydroxide salt as shown in Fig. 2.5(b).

The related chemical reactions of calcium with H_2O and O_2 were assumed to be the following:

$2Ca+O_2 \rightarrow 2CaO,$ (2.2)

$Ca+H_2O \rightarrow CaO+H_2,$ (2.3)

$CaO+H_2O \rightarrow Ca(OH)_2$. (2.4)

Then, the reacted sites can be observed as spots on the Ca film. Although it did not distinguish between oxygen and water permeation and it was more qualitative comparison, it was still a simple and direct method to compare the permeability of different materials.

Table 2.1 Summary of WVTR measuring methods, their detection principles and advantages and disadvantages.

Method	**Detection principle**	**Advantage**	**Disadvantage**	**Reference**
Gravimetric	loss of water or gain of water on P_2O_5	Easy、direct	Low sensitivity	
Spectroscopy	mass spectroscopy, fluorescence quenching	High sensitivity	expensive	
Calcium degradation	optical density	Simple、easy、cheap	Low sensitivity	[20]
	change in resistance	easy data-point acquisition	Ca storage	[21]
Radioactive	tritiated water (HTO) or CO	direct high sensitivity (~10^{-8}g/ m^2day)	expensive	[22]

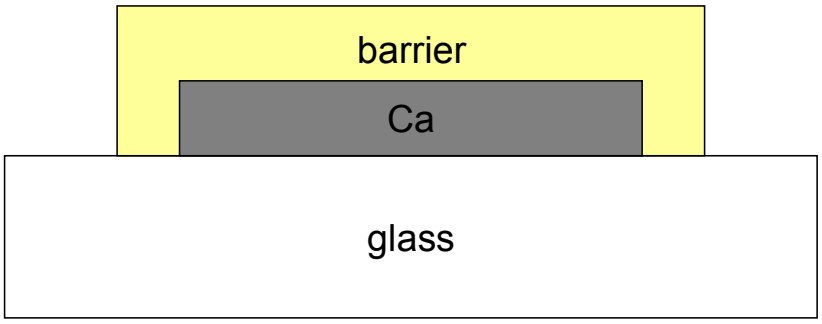

(a)

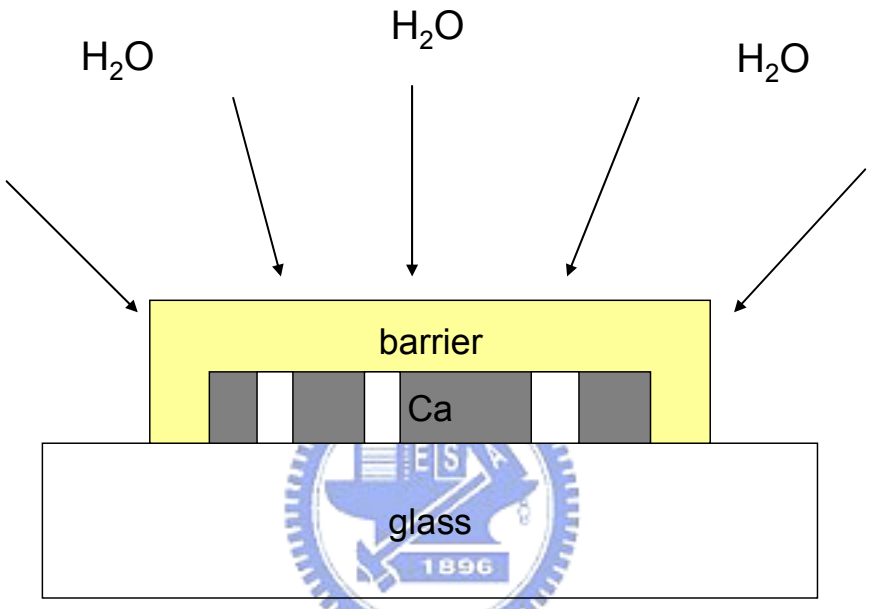

(b)

Figure 2.5(a) Illustration of the structure for Ca test before testing, (b) the structure changed after H_2O permeating.

2.2 Passivation and Packaging Technologies in OLED Devices

2.2.1 Glass Packaging

To protect the OLED's organic thin film materials and cathode metal from the oxidation or reaction, display manufacturers first employed glass as substrate and then glue a metal can or glass lid on the back of OLED display to keep out moisture and oxygen as illustrated by Fig. 2.6, first reported by Burrow *et al*, [4] which was the

same packaging method as in LED. However, minute quantity of moisture still permeated through the gluing epoxy and the sensitivity to moisture and oxygen in OLED. As a result, a desiccative was implemented inside the display between the glass substrate and glass lid to getter moisture. Still, glass packaging has several critical disadvantages such as cracks and impact resistance, in addition to weight and high cost concern. For example, as to cell-phone display, a glass lid, glue and a desiccative that add up cost about 1.2 dollars. It marked about three dollars of cost not including the cost of electronic device. If it still used glass packaging in OLED which were the same as LED, it was hard to compete with LED. Hence, it was necessary to develop the thin film packaging in OLED. [23]

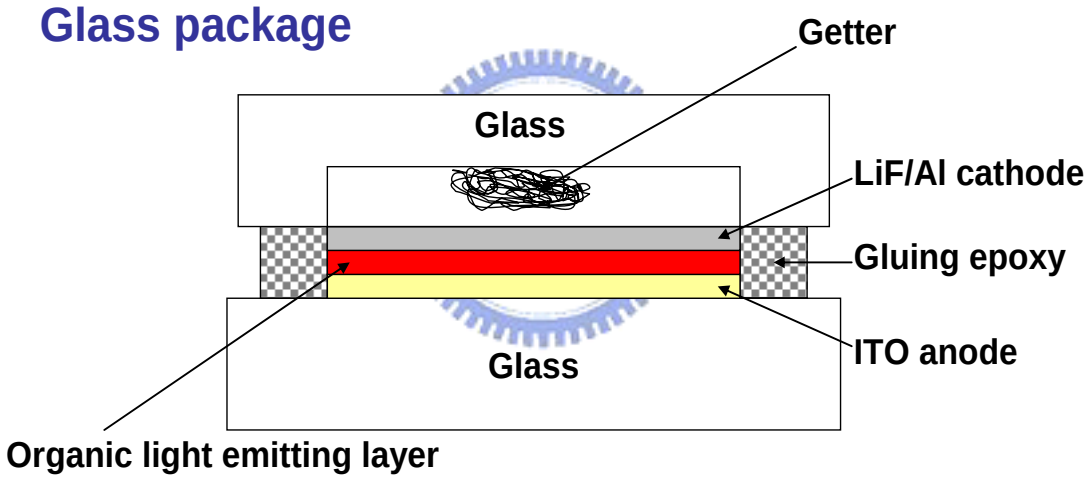

Figure 2.6 Schematic diagram of glass package in OLED technology.

2.2.2 Thin Film Packaging

In order to reduce the weight and cost while maintaining equal or better moisture/oxygen resistance, recent thrusts in OLED packaging focused on the development of a thin-film barrier such as polymers, ceramics or their composites as

illustrated in Fig. 2.7. The selection of polymers included parylenes, cyclotene, etc. [24, 25] and the selection of ceramics included oxide- or nitride- base barrier films such as SiO_x, AlO_x, SiN_x, SiO_xN_y, etc. [25-34]

Thin film barriers have usually been formed on Al or other metal layers. Traditionally, bulk oxides and Al were effectively impermeable to oxygen and moisture, as perfect barrier films. [26, 35, 36] But traditional single thin film barrier layers did not provide the moisture/oxygen resistance we wished, whether deposited by plasma-enhanced chemical vapor deposition (PECVD), sputtering, or e-beam evaporation and Table 2.2 showed some reported water vapor resistance properties of passivation layers. [30-34] However, these reported barrier films still showed too high WVTR and OTR for OLED's applications. This limit was attributed to defects or pinholes contained in the thin films during deposition compared to the bulk of the barrier film. [26]

Table 2.2 Some reported water vapor resistance properties of passivation layers.

Material	**Deposition method**	**Thickness (nm)**	**WVTR (g/m^2-day)**	**Reference**
SiOx	Reactive evaporation	70	0.3	[30]
SiOx	PECVD	12	0.15	[31]
SiNx	PECVD	30	0.15	[32]
AlOxNy	Sputter	55	0.1	[33]
AlOx	Ebeam	30	0.17	[34]

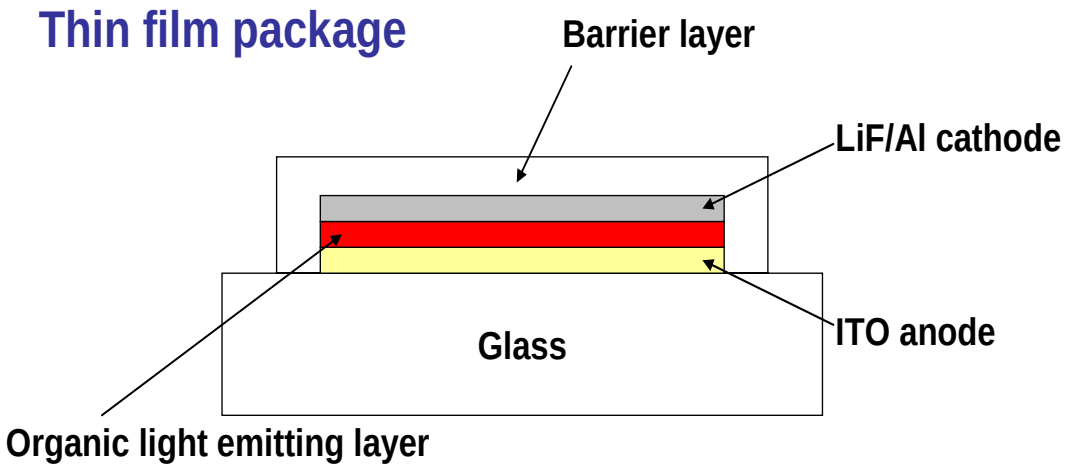

Figure 2.7 Schematic diagram of thin-film barrier package in OLED technology.

To overcome the deficiency of thin film inorganic barrier, Vitex System Inc. announced a novel barrier, [7, 8] Barrix™ comprised of alternating layers of polymer and ceramic film deposited in vacuum to achieve very low moisture and oxygen permeation through the filling of pinhole and defects in inorganic layers by polymer and the tortuous path in the stacking as shown in Fig. 2.8. By stacking multi-layer of organic and inorganic thin films to about 3 μm, Barrix™ layers can meet the requirements of WVTR for OLED applications. However, the deposition process as shown in Fig.2.9 seemed very complicated and needed many procedures. Hence, the cost and thermo-mechanical integrity of such ceramic/polymer multiple-layer structure (Barrix™ layer) remained a lingering issue.

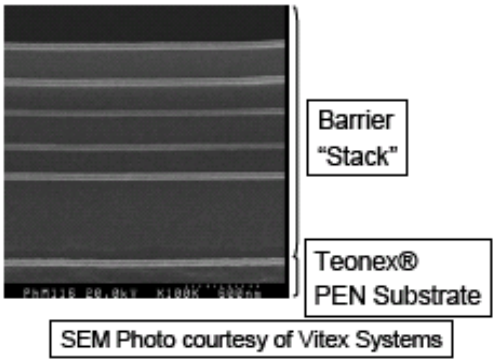

Figure 2.8 Organic/inorganic multi-layer structure from Vitex Systems. (Reproduced courtesy of Vitex Systems.)[7, 8]

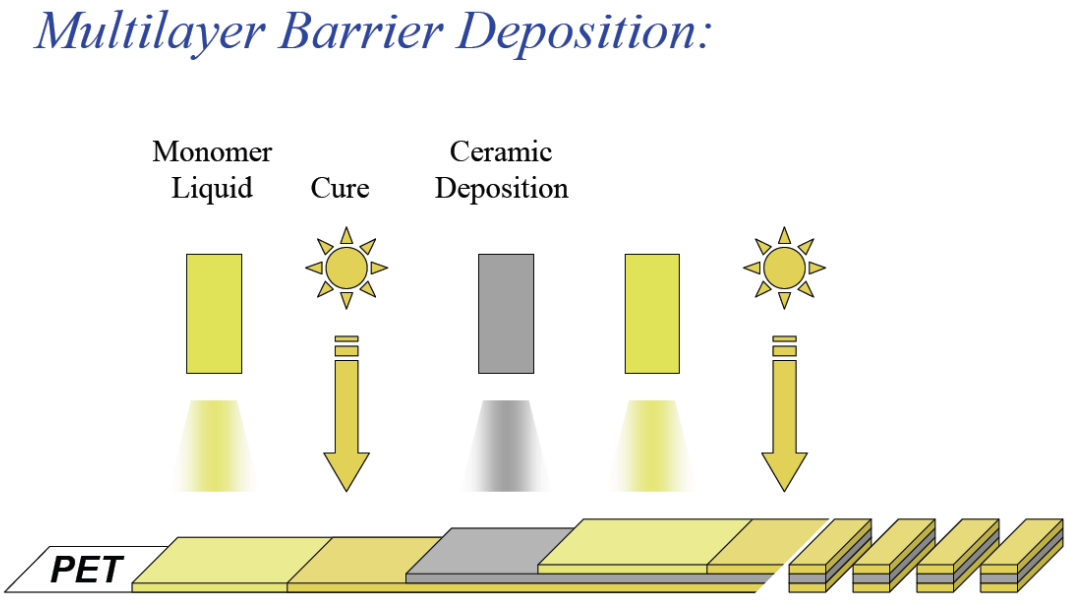

Figure 2.9 The deposition process of Barrix^{TM} layers. [7, 8]

2.3 Microstructure of Thin Films

The quality of thin films in the OLED stack was closely related to its effectiveness as moisture and oxygen barriers. [26, 37] Hence, the growth process of thin film needed to be understood and reviewed below. Thin films were usually formed by deposition which was a process through continuous stages as shown in Fig.

2.10. [38, 39] First, deposited particles arrived to the substrate surface. Then nucleation was generated on the substrate surface and islands grow. Next, islands were coalesced by surface diffusion and eventually a continuous layer was formed. Either layer-by-layer (epitaxial) or island (nonepitaxial) growth of thin layers would be chose by the interfacial energy of deposited atom-deposited atom and deposited atom-substrate atom. If the interfacial energy between deposited atom and deposited atom was higher, island growth would be favored. If the interfacial energy between deposited atom and substrate surface was higher, epitaxial growth would be favored. In conclusion, the evolution of the structure in thin films was very complicated and presented different features in different stages of thin film growth.

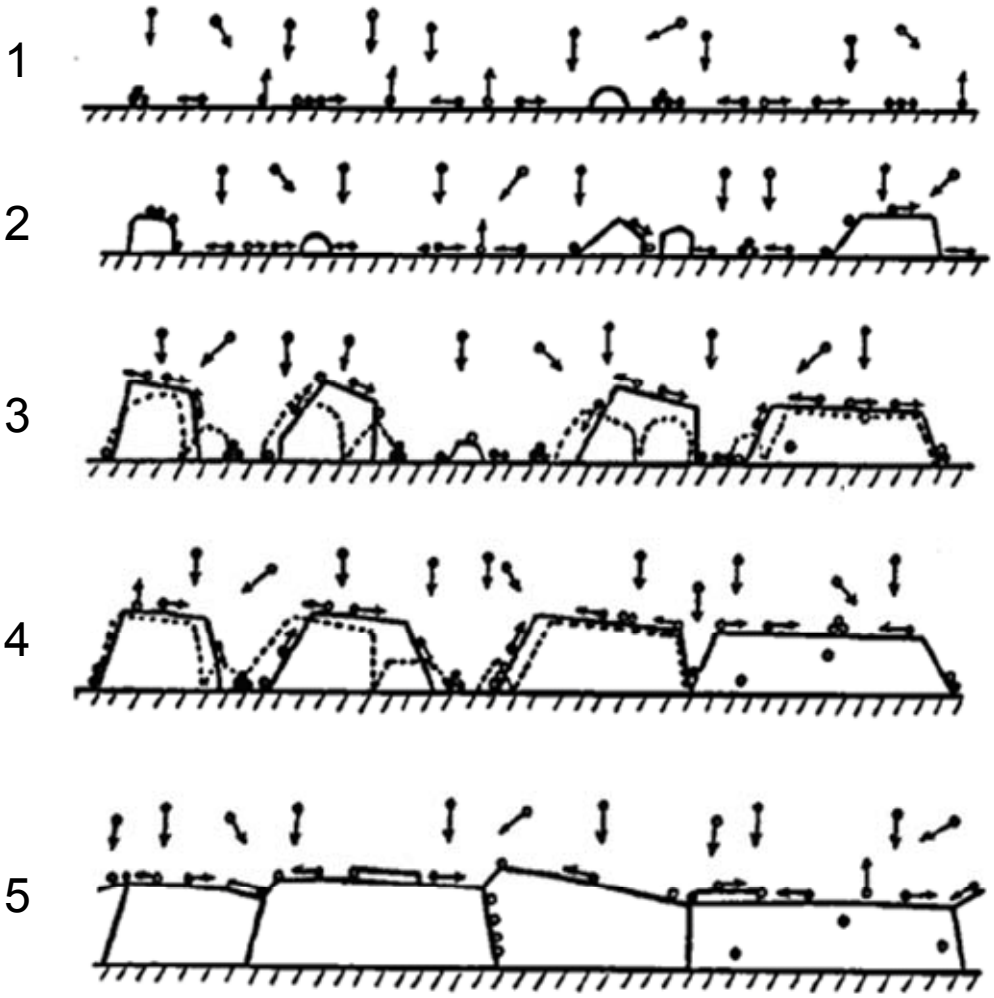

Figure 2.10 Schematic diagram illustrating fundamental growth processes. The growth of thin films progresses through consecutive stages: stage1 is nucleation, stage

2 is island growth, stage 3 is coalescence of islands, stage 4 is formation of polycrystalline islands and channels, and stage 5 is development of continuous structure and thickness growth. [39]

The microstructure of the developing film would be characterized by the shape of its grain structure. The grain structure was affected by the growing environment such as substrate temperature, surface roughness, chamber pressure, the cleanliness levels, etc. [9, 40-42] For example, low substrate temperature led the grain growth to amorphous or polycrystalline. Thornton [9] presented a diagram which considered the effect of chamber pressure and substrate temperature on the structures of PVD films as shown in Fig. 2.11. There were four types of grain structure shapes as a function of substrate temperature and chamber pressure. In Zone I, the layer was either amorphous or fiber shape, the texture was random, and crystallite size was about 5–20 nm diameter. In Zone T, the grains had quite different sizes with increasing temperature. The structure was inhomogeneous along the film thickness. Near the substrate, the microstructure consists of randomly small grains and out of which was V-shaped columns with the favored orientations. Voids existed both in Zone I and T. In Zone II**,** the homogeneous grain structure was columnar shape and the diameter increases with film thickness. Zone III represented the globular structure which was developed by lateral grain growth and this structure was usually grew in the high substrate temperature range. [9, 38, 39]

According to the above discussion, it was well known that the morphology of thin film and its grain structure can be controlled by the deposition parameters. On the moisture and oxygen resistance issue, the dense films with amorphous structure and low defects were desired to serve as the passivation layer in the OLED packaging.

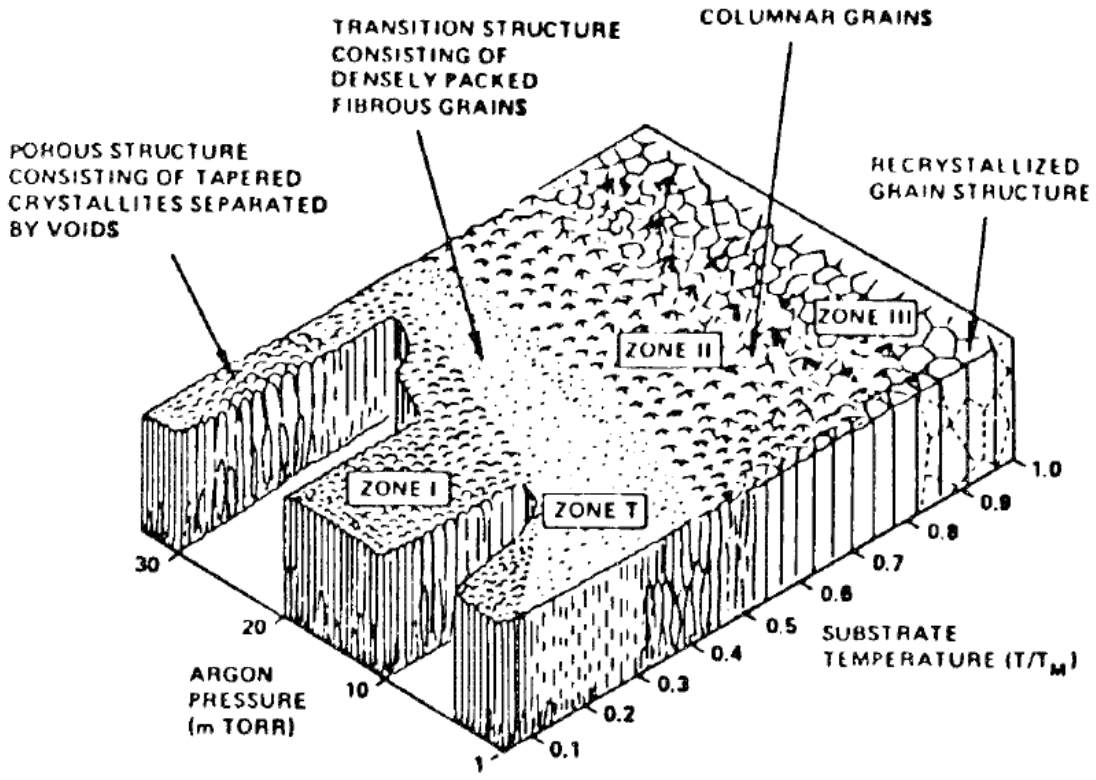

Figure 2.11 Structural zones in PVD films as a function of substrate temperature and chamber pressure. [9]

2.4 Thin Film Stress

The source of thin film stress included intrinsic stress and thermal stress which depends on their cause mechanisms. [10, 11] Intrinsic stress was caused during thin film deposition and lattice parameters mismatch of the film and substrate. Therefore, the value of intrinsic stress can be controlled by changing the deposition parameters. It may be affected by the defects in thin film, ion bombardment to the surface of films, and different atomic arrangement, etc. However, the definition of intrinsic stress was still under discussion.

Thermal stress was contributed by CTE mismatch and temperature difference. When the temperature was changed of a thin film on a substrate, a strain was introduced because of the different thermal expansion coefficients and the expression

is

$$\varepsilon_{film} = \left(\alpha_{film} - \alpha_{substrate}\right)\Delta T \tag{2.5}$$

where α_{film} and $\alpha_{substrate}$ are the thermal expansion coefficients of the film and substrate, respectively. Then, stress in the thin film can be determined by the expression (2.6)

$$\sigma = E\varepsilon \tag{2.6}$$

Finally, the calculation of the strain in (2.5) can be used in (2.6) to derive the thermal stress in thin films.

Chapter 3 Experimental

3.1 Deposition System

For the deposition of Al cathode or passivation film onto OLED, conventional sputtering could cause serious radiation damage to the underlying organic layer in OLEDs due to the energetic ions, electrons and x-rays produced during deposition, while plasma-enhanced chemical vapor deposition (PECVD) method can readily damage OLED device because of the toxic, reacting gases and high deposition temperature involved in the deposition process. Therefore, evaporation technique has been widely adopted in the deposition of the passivation layer for the OLEDs to avoid thermal decomposition or plasma damage. [43-45] However, in order to reduce the coast in production, the deposition rate should be high and the required number of barrier layers shall be the minimum. Therefore, an Ar ion beam evaporation system designed for continuous process was chosen for almost all layers and organic layer such as Alq_3 in the preparation of OLED. [46]

The schematic diagram of the Ar ion beam evaporation system for depositing moisture barrier layers and Al films devices in this study was illustrated in Fig. 3.1. The vacuum chamber was vacated until the pressure was lower than 1.0×10^{-4} Pa before deposition was initiated. Argon and nitrogen gases were injected into the chamber, and the pressure was about 0.1 Pa. Argon gas was injected into arc plasma generator and the argon gas became arc discharge plasma by applying appropriate power. SiO_2 or Al ingots were evaporated by arc discharge plasma onto crucibles, and the SiO_xN_y films and Al films were then deposited on glass substrates. The deposition temperature was controlled by the distance between source and glass plate, and the horizontally moving speed of glass plate. Furthermore, the particle energy arriving to the surface of OLED structure was about 25 eV. This was lower than the energy from

the sputter system which was more than 100 eV as shown in Fig. 3.2. Thereby, this system would not damage the underlying Alq_3 layer and could be practically used for OLED manufacturing.

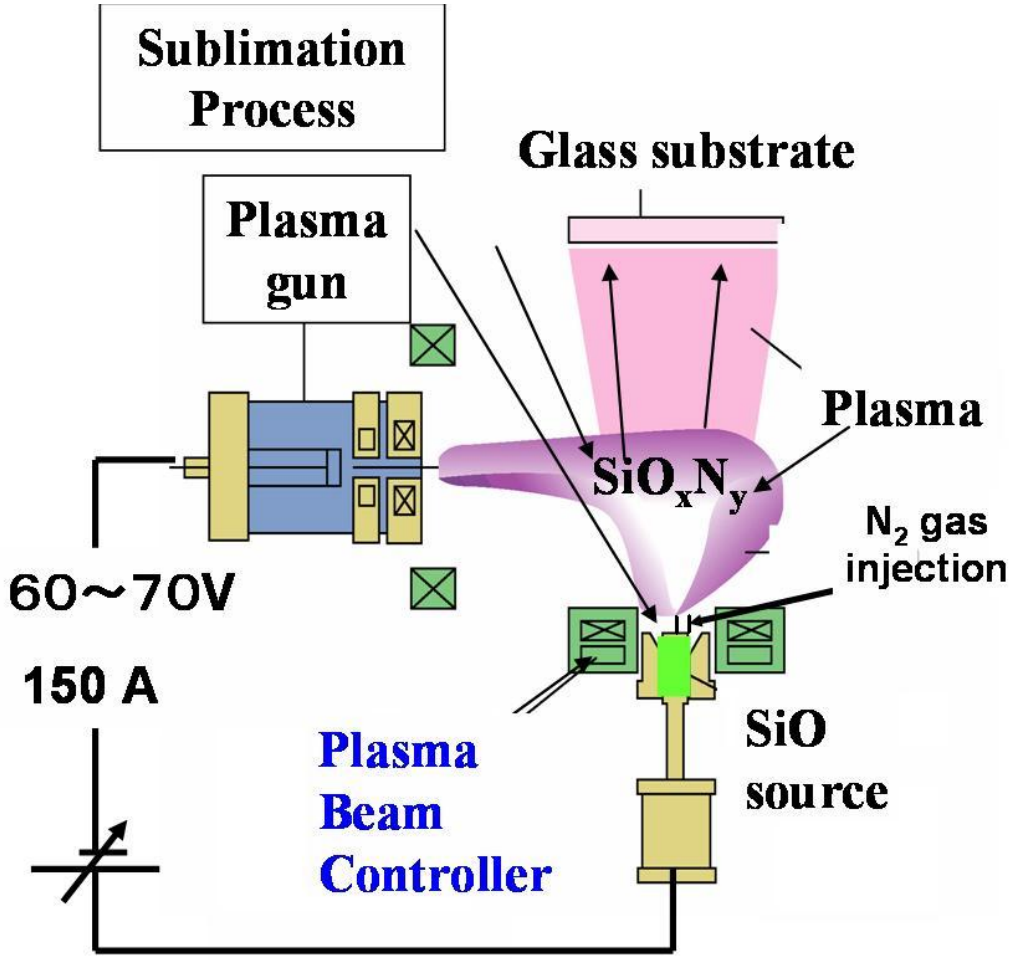

Figure 3.1 The schematic diagram of an argon ion-beam evaporation system.

(Courtesy of China Picture Tube, Inc.)

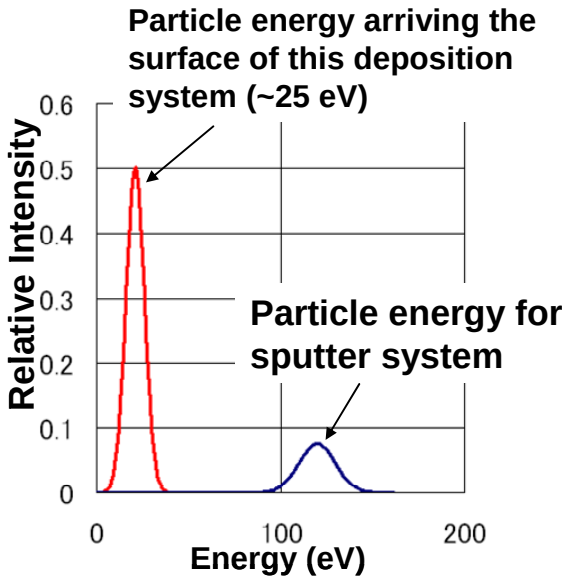

Figure 3.2 Energy distributions of the particle arriving to the substrate surface for conventional sputtering system and Ar ion beam evaporation system. (Courtesy of China Picture Tube, Inc.)

3.2 Sample Preparation

Silicon oxynitride (SiO_xN_y) passivation layers and electrode Al films were deposited by using a modified Ar ion beam evaporation technique. In our deposition system, thermally energetic silicate-containing molecules were evaporated from SiO_2 or Al crucible, which was heated by Ar ion beam bombarding the exterior of crucible, and deposited onto substrates. The deposition system was also equipped with gas lines next to SiO_2 source. For example, silicon oxynitride was formed by blowing N_2 during the evaporation of SiO_2. The deposition temperature was controlled by the distance between source and glass plate, and the moving speed of glass plate. In this study, 600 Å thick silicon oxynitrides films were deposited onto Al (2000 Å)/Alq_3 (10 Å)/glass at different substrate temperatures (60, 80 and 90 ^oC) with different N_2 flow rates from 300 sccm to 480 sccm. Specifically, 480 sccm is designated as the high flow rate condition, while 300 sccm is designated as the low flow rate condition in

this study unless stated otherwise. The film thicknesses of SiO_xN_y barrier/Al/Alq_3 /glass and the stack structure of samples used in this study were shown in Fig. 3.3. In addition, their deposition conditions were listed in Table 3.1.

The effects of substrate temperature and flow rates on the microstructures (crystallinity and grain size), morphology, defects in barrier layers and its correlation with water permeation were investigated in this thesis.

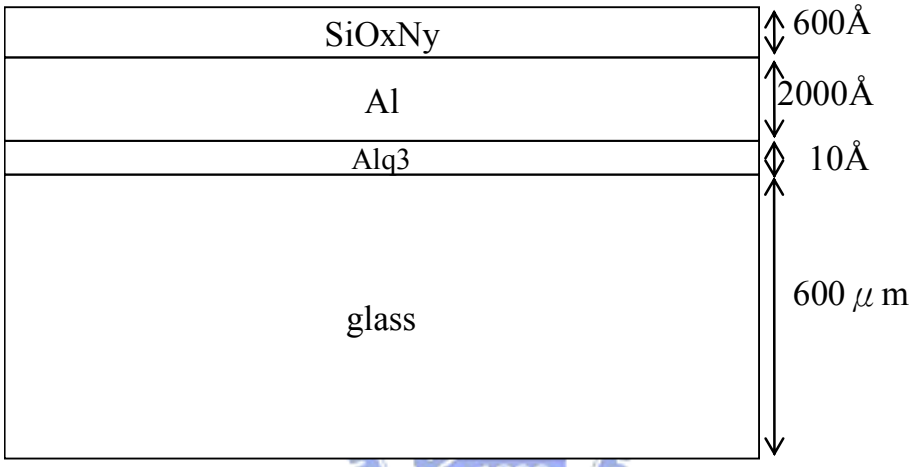

Figure 3.3 The film thickness and stack structure of samples.

Table 3.1 Deposition parameters of SiO_xN_y barrier layer.

SiOxNy barrier	**Flow rate**	**Substrate temperature**
Best Case	High N_2 (480sccm)	60 ℃、80 ℃ 、90 ℃
Worst Case	Low N_2 (300sccm)	60 ℃、80 ℃ 、90 ℃

3.3 Experimental Procedure

As illustrated by the flow chart shown in Fig. 3.4, the chemical structure and composition of the oxynitride films were investigated using x-ray photoelectron spectroscopy (XPS) (VG Scientific, Microlab 350F). The frequency of Si-O-Si bond stretching vibration was obtained by specular reflectance FTIR spectroscopy (Perkir Elmer Spectrum 100). The moisture barrier effectiveness was first measured by a calcium button test (Courtesy of China Picture Tube, Inc.). Then, the relationship between moisture resistance and the microstructure of barrier layers was investigated. The morphology and microstructures of silicon oxynitride and aluminum films were examined by a scanning electronic microscopy/EDX (SEM/EDX) (JEOL JSM-6700F) and a transmission electron microscopy (TEM) (Philips TECNAI 20), respectively. In addition, grain sizes of aluminum films were obtained from an x-ray diffraction (XRD) (Siemens D5000). Defects such as Al hillock and its densities were further quantified using an Al wet etch decoration method in conjunction with optical microscope. The surface roughness of passivation layers and the maximum height of hillocks were characterized by an atomic force microscope (AFM) (Veeco D5000). Moreover, the effect of as-deposited stress on the formation of hillock defects was examined. The stress of the multi-layer was obtained from bending beam system to measure the curvature radius of the SiO_xN_y/Al/Alq_3/glass sample.

In the following section, characterization methodologies for moisture barrier, hillock defects, residual stress, and chemical structure, and analytic instrumentation such as SEM, TEM, XRD, AFM, nanoindenter, specular reflectance FTIR, XPS and bending beam would be briefly described in the following sections.

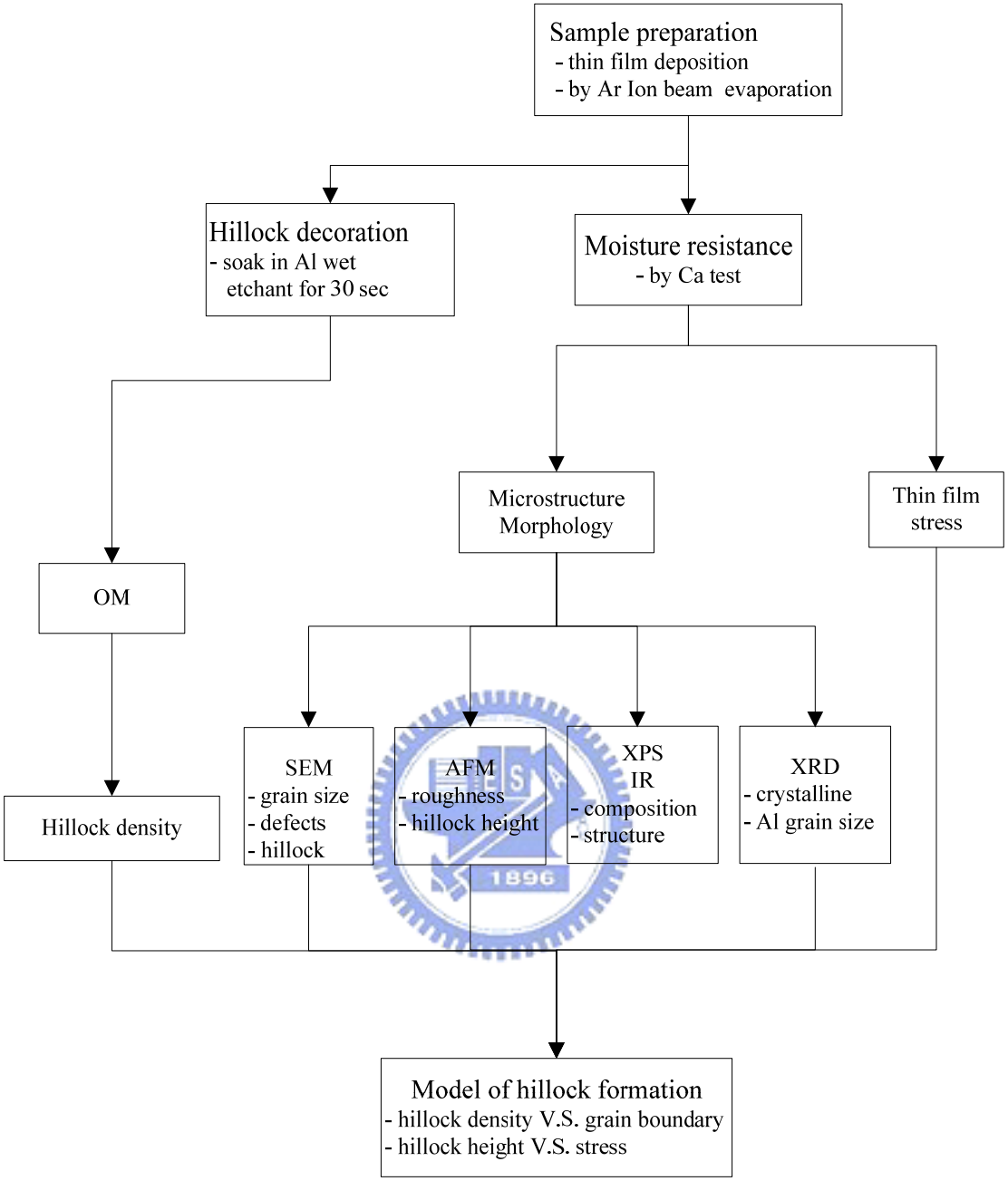

Figure 3.4 Flow-chart of experimental procedures.

3.4 Characterization Methodologies

3.4.1 Decoration of Al Hillock Defect by a Selective Etching Process

Although SEM and EDX were employed to identify the existence of Al hillock breaking through passivation layer, these techniques were not suitable to quantify the density of hillocks due to the field size, time and cost. Therefore, it was highly desirable to develop a selective, wet etching process to remove the extruded Al over the surface of passivation layer, for example, silicon oxynitride, such that hillock defects were decorated as holes, which can be detected easily using an optical microscope. The typical wet etching chemicals for SiO_2, Si_3N_4 and Al, the chemical reactions involved, and application were summarized in Table 3.2, Table 3.3 and Table 3.4, respectively. Although phosphoric acid solution could etch silicon nitride, it still required relatively high operating temperature, at 150 to 200 ℃. Therefore, aluminum wet etchant (composition: 80% phosphoric acid, 5% acetic acid, 5% nitric acid, and 10% water) was used to etch the SiO_xN_y/Al/Alq_3/glass samples at 42 to 45 ^oC to provide excellent selectivity (Al to SiO_xN_y). The typical etching time used in this study was 30 seconds and the wet etching process was schematically shown in Fig. 3.5.

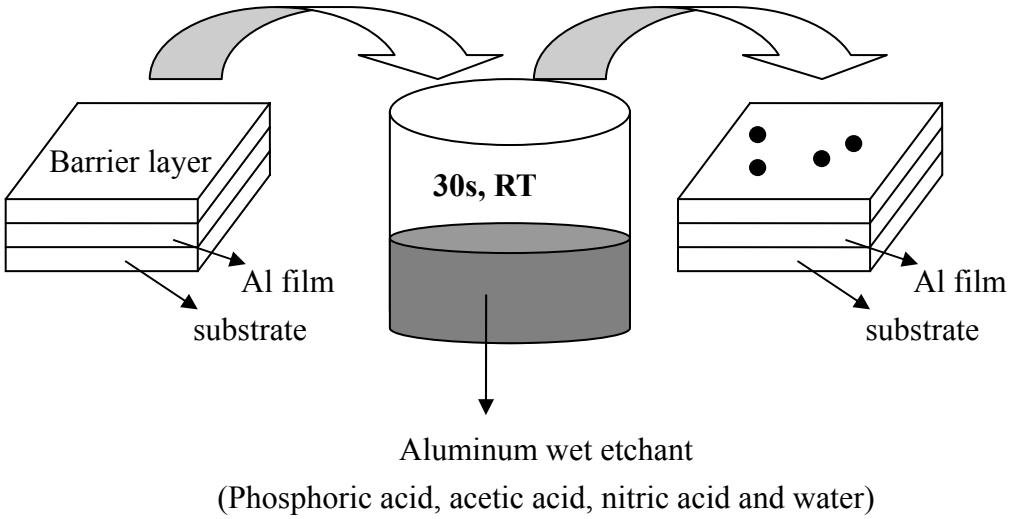

Figure 3.5 Schematic diagrams of etching process for decoration of Al hillocks.

Table 3.2 Description of wet etching SiO_2 layer. [47]

Etching material	SiO_2
Etchant	• Hydrofluoric Acid (HF) Solution • Normally diluted in buffer solution or DI water to reduce etch rate.
Reaction	$SiO_2 + 6HF \rightarrow H_2SiF_6 + 2H_2O$
Applications	• Widely used for CVD film quality control • BOE: Buffered oxide etch

Table 3.3 Description of wet etching Si_3N_4 layer. [47]

Etching material	Si_3N_4
Etchant	• Hot (150 to 200 ˚C) phosphoric acid H_3PO_4 Solution
Reaction	$Si_3N_4 + 4\ H_3PO_4 \rightarrow Si_3(PO_4)_4 + 4NH_3$
Applications	• High selectivity to silicon oxide • Used for LOCOS and STI nitride strip

Table 3.4 Description of wet etching Al layer. [47]

Etching material	Al
Etchant	• Heated (42 to 45 ˚C) solution • One example: 80% phosphoric acid, 5% acetic acid, 5% nitric acid, and 10 % water
Reaction	• Nitric acid oxidizes aluminum and phosphoric acid removes aluminum oxide at the same time. • Acetic acid slows down the oxidation of the nitric acid.
Applications	• High selectivity to silicon oxide • Used for ULSI process

3.4.2 Ca Button Test for Moisture Permeation

The moisture resistance of barrier layers was qualitatively examined by a Ca button test through the observation of the corrosion of calcium. Typically, the barrier layers such as SiO_xN_y films were deposited onto a 300Å thick calcium on a glass plate. This test was carried out in an oven at 60 ^oC and 90% relative humidity for 15 minutes or at room temperature and humility for 66 hours. Then, the reacted sites could be observed as spots on the Ca film and the permeability of different materials could be

compared. The detail of this method is mentioned in Chapter 2.1.3.

3.5 Instrumentation and Data Analysis

3.5.1 FE-SEM

Field-emission scanning electron spectroscopy (FE-SEM) (JEOL 6700F) was employed to investigate the morphologies of barrier layers. FESEM is a powerful analysis tool to characterize microstructure down to several ten nanometers.

3.5.2 HR-TEM

High resolution transmission electron microcopy (HRTEM) (Philips Tecnai 20) was used to obtain high magnification and high resolution image of cross-sectional image of SiOxNy/Al bi-layer. Information obtained from TEM is not only the high resolution image but also the crystal structure, orientations and chemical compositions.

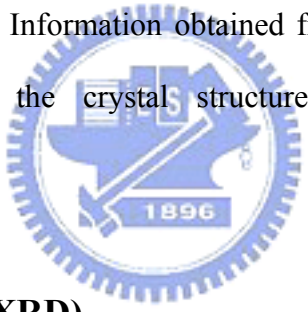

3.5.3 X-ray Diffraction (XRD)

XRD (Siemens D5000) was employed to characterize the crystallite sizes of aluminum films. The operation voltage of the XRD used in this measurement was 40 kV and the operation current was 30 mA. The X-ray was used the characteristic peak Kα of Cu (λ=1.5406Å) which was filtered by Ni-filter. The detector scanned the samples between 2θ= 10-90 degrees.

The crystallite sizes of aluminum films can be calculated by the full width at half maximum of the dominant Al (111) peak in XRD patterns schematically illustrated by Fig. 3.6, according to Scherrer's equation (3.1) [48]

$$t=0.9\lambda/B\cos\theta \qquad (3.1)$$

where t is the crystallite size, λ is the wavelength for Cu K_{α}, B is the full width at half

maximum and θ is the diffraction angle.

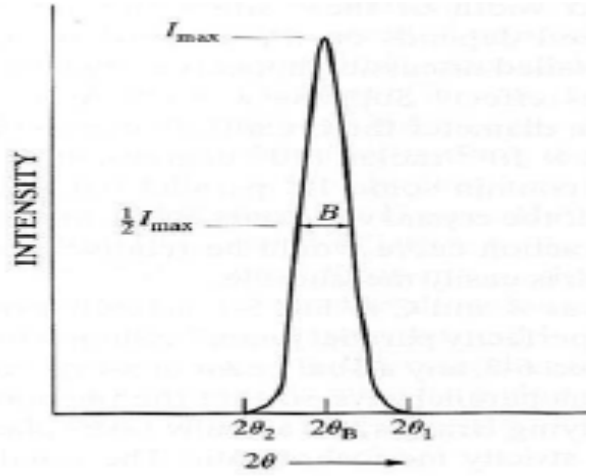

Figure 3.6 XRD patterns of crystalline film with finite crystallite size. [48]

3.5.4 Atomic Force Microscope (AFM)

AFM (Veeco D5000) was employed to quantify the surface roughness of passivation layers and the maximum height of hillocks in a tapping mode. In operation, the cantilever was biased with AC and DC voltage and sensed the distance between the tip and the sample surface by Van der Waal's force. As the interaction force changed between the cantilever tip and the surface, the deflections of the cantilever were varied. Then, the deflections were measured and derived a topographic image of the surface.

3.5.5 Nanoindentation

Young's modulus of glass substrate was measured by nanoindentation. A MTS Nano Indenter XP system in Nano-Device Lab with a three-side pyramid (Berkovich) tip was employed in a continuous stiffness mode (CSM) and at a constant strain rate 0.05 s^{-1}. The load–displacement relation was used to evaluate the mechanical properties of samples as shown by Fig. 3.7. For a single film structure, Oliver and Pharr analysis method was employed for nanoindentation measurement to derive E_f.

[49]The reduced Young's modulus, E_r can be obtained by Equation 3.2:

$$E_r = \frac{\sqrt{\pi}}{2\beta}\frac{S}{\sqrt{A}} = \frac{\sqrt{\pi}}{2\beta}\frac{1}{\sqrt{A}}\frac{dP}{dh} \tag{3.2}$$

where

E_r: reduced modulus

ß: constant depending on the geometry of the indenter

A: projected area of elastic contact

$S = \frac{dP}{dh}$: the slope of the load–displacement curve at the beginning of the unloading stage as illustrated in Fig. 3.8.

Then, E_r can be further expressed in terms of film and indenter by Equation (3.3):

$$\frac{1}{E_r} = \frac{(1-\nu_f^2)}{E_f} + \frac{(1-\nu_i^2)}{E_i} \tag{3.3}$$

where

E_i, v_i: Modulus and Poisson's ratio of the indenter

E_f, v_f: Modulus and Poisson's ratio of the specimen

Finally, the modulus of thin film (E_f) was rearranged as a function of penetration depth in our measurement and derived by combining Equation (3.3) and (3.4).

$$E_f = \frac{(1-\nu_f^2)}{\frac{1}{E_r} - \frac{(1-\nu_i^2)}{E_i}} \tag{3.4}$$

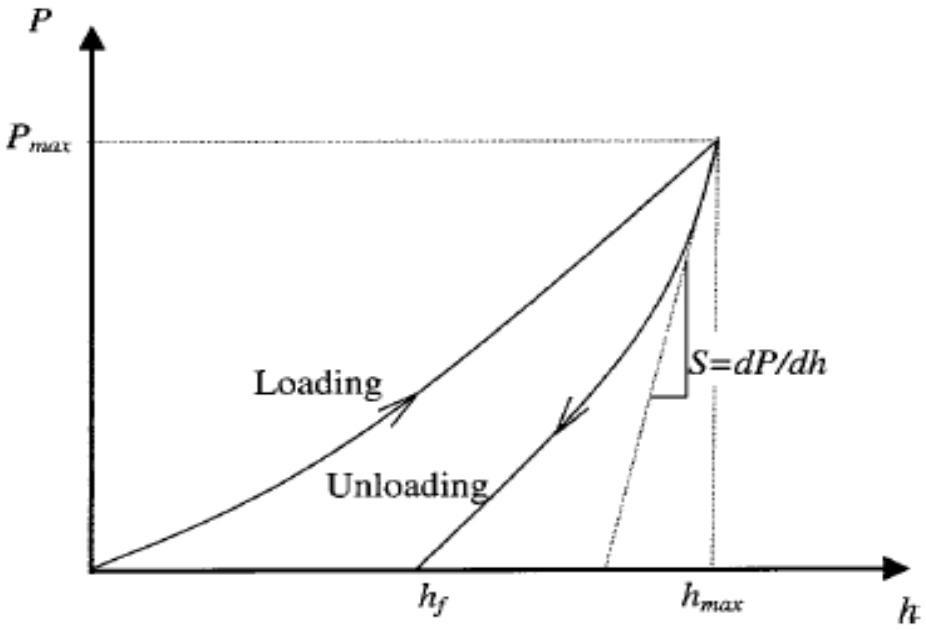

Figure 3.7 Load-Displacement of Nanoindentation. [49]

3.5.6 Specular Reflectance Fourier-Transform Infrared Spectroscopy (Specular Reflectance FT-IR)

Since Al film is a good reflective mirror in SiO_xN_y/Al/glass sample stack, specular reflectance FTIR spectroscopy (Perkir Elmer Spectrum 100) was employed to examine the chemical make and structural information of SiO_xN_y. In particular, Si-O-Si bond stretching frequency in SiO_xN_y thin film samples was measured by a specular reflectance apparatus VeeMAX [50] at 40^o incident angle as schematically shown in Fig. 3.8. The specular reflectance infrared spectra were collected in 500-4000 cm^{-1} range with a resolution of 4 cm^{-1}.

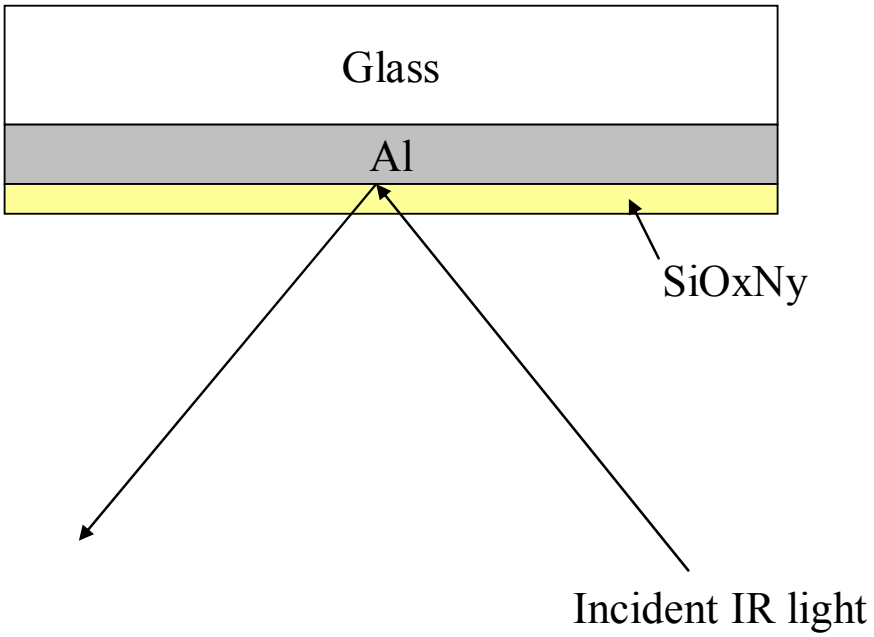

Figure 3.8 Schematic diagram of a specular reflectance infrared spectroscopy.

3.5.7 X-ray Photoelectron Spectroscopy (XPS)

The composition and chemical bonding of the oxynitride films were investigated using XPS (VG Scientific, Microlab 350F). The photoelectron emission spectra were obtained using an Mg *Kα* X-ray source (E=1253.6 eV) striking the surface of the sample. The analyzer resolution was fixed at 0.01 eV. Ar^+ ion was used to remove adsorbed surface contaminants for 5 seconds before analysis. The insulating properties of these deposits caused surface charging effects, resulting in electron lines being shifted to lower kinetic energies. [51] The peak positions were calibrated with respect to the position of C 1s carbon contamination peak usually located at about 285 eV.

3.5.8 Bending beam system

3.5.8.1 Evolution of Stoney's Equation

If the film deposited on the substrate is under stress, it will result in a bending to maintain mechanical equilibrium. And if the film is very thinner than the substrate and the stress in the film is linear related to the curvature of the substrate that the relationship was deduced by G. G. Stoney in as early as1909. [52] Stoney's equation is

$$\sigma = \frac{E_s t_s^2}{6(1-\nu_s)t_f}\frac{1}{R} \tag{3.5}$$

Since the substrate is not absolutely flat in many cases, it may have its initial curvature. Thus, Equation (3.5) should be deduced by subtracting the initial curvature $(1/R_0)$ from the measured curvature $(1/R)$. Stoney's equation becomes:

$$\sigma = \frac{E_s t_s^2}{6(1-\nu_s)t_f}\left(\frac{1}{R}-\frac{1}{R_0}\right) \tag{3.6}$$

where E_s and υ_s are the Young's modulus and Poisson's ratio of the substrate, and t_f and t_s are the thicknesses of the film and substrate. R_0 is the radius of curvature of the uncovered substrate and R is the radius of curvature with the film on the substrate.

Therefore, the stress can be determined by measuring the curvature of the sample in conjunction with the only parameter, thickness of thin film and Young's modulus and Poisson's ratio of the substrate, which can be obtained from literatures. Consequently, Stoney's equation has been extensively used for thin film stress studies through curvature measurement.

3.5.8.2 Bending Beam System

The schematic diagram of the bending beam system was illustrated in Fig.3.9. The sample (thin film/substrate) in free standing form was put inside the copper heater block, which can be heated up to 450 ^{o}C, in the vacuum chamber. Two parallel laser beams were directed onto the sample at two different positions and then were reflected to two position-sensitive detectors as shown in Fig.3.10, in which

D is the spacing of two incident laser beam.

L is the distance between the sample and position-sensitive detector.

S is the spacing of two reflected laser spots on detector.

S_0 is the spacing of the bare substrate from two reflected laser spots on detector.

1/R is the curvature of the substrate with film, and

$1/R_0$ is the curvature of the bare substrate.

Then, the change of the curvature could be derived by the following expression (Stoney's equation):

$$\sigma = \frac{E_s t_s^2}{6(1-\nu_s)t_f}\left(\frac{1}{R}-\frac{1}{R_0}\right) \tag{3.6}$$

From the geometry relationship in Fig.3.10,

$$\tan\theta \approx \frac{D/2}{R} = \frac{D}{2R} \approx \theta \text{, since } \theta \to 0 \tag{3.7}$$

$$\tan 2\theta \approx \frac{D}{R} = \frac{a}{L} \tag{3.8}$$

Hence,

$$\frac{1}{R} = \frac{a}{DL} \tag{3.9}$$

With the same principle,

$$\frac{1}{R_0} = \frac{b}{DL} \tag{3.10}$$

Equation (3.3) in substitution for (3.6) and (3.7) becomes:

$$\sigma = \frac{E_s t_s^2}{6(1-\nu_s)t_f}\left(\frac{a-b}{DL}\right) \tag{3.11}$$

In addition,

$$\Delta S = S_0 - S = 2(a-b) \tag{3.12}$$

Equation (3.11) in substitution for (3.12) becomes:

$$\sigma = \frac{E_s t_s^2}{6(1-\nu_s)t_f}\left(\frac{\Delta S}{2DL}\right) \tag{3.13}$$

Finally, thin film stress using bending beam system and Stoney's equation was derived. In order to increase the sensitivity and accuracy of the measurement, film thickness/substrate thickness needed to be less than 1/1000 and the sample size was close to 5 cm long and 1 cm wide. In our experiment, the sample was cut to 5 cm long and 1 cm wide. The total film thickness/substrate thickness is about 0.25 μm/600 μm which is less than 1/1000. In order to reduce the noise caused by sample vibration at temperature higher than 300 ^{o}C, the chamber was first evacuated to 6 mTorr, then introduced with N_2 to 50 Torr. Typically, the heating rate was 2℃/min in the heating cycle, then nature cooling as employed in the cooling cycle. Since the S_0 cannot be obtained by etching the film off the transparent glass substrate, the selected S_0 can be estimated by (positive S+ backside S)/2 in this study.

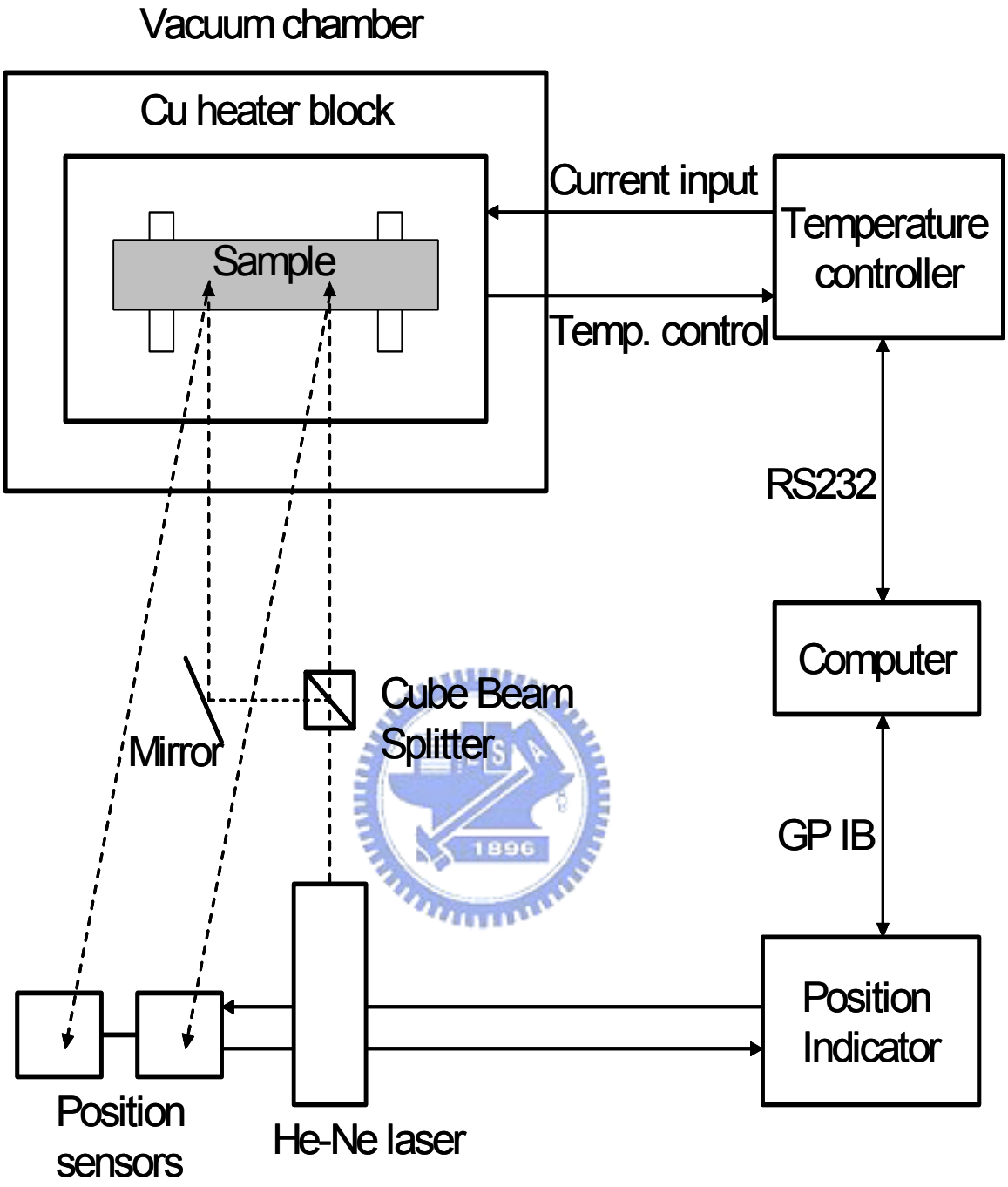

Figure 3.9 Schematic setup of a bending beam system for stress measurement.

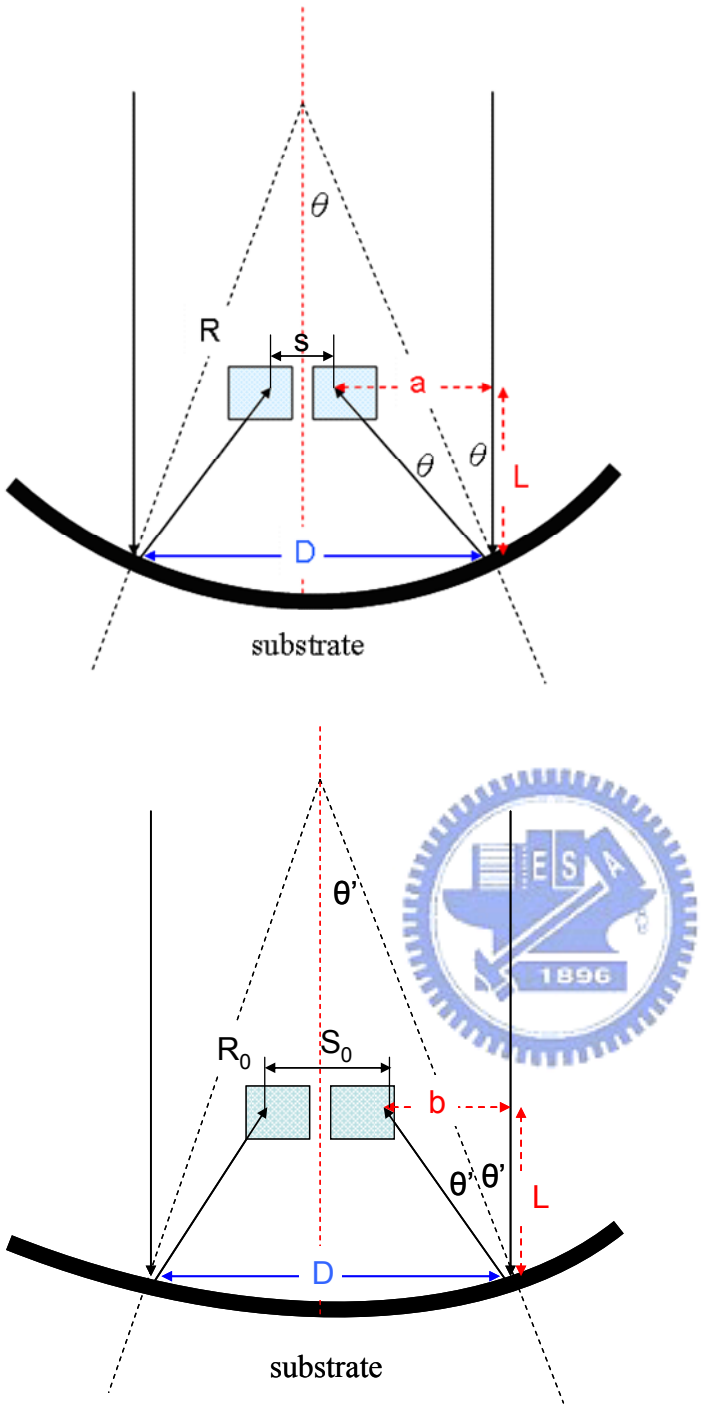

Figure 3.10 Schematic diagram of the laser routes in the bending beam system.

D is the spacing of two incident laser beam. L is the distance between the sample and position-sensitive detector. S is the spacing of two reflected laser spots on detector. S_0 is the spacing of the bare substrate from two reflected laser spots on detector. 1/R is curvature of the substrate with film. $1/R_0$ is curvature of the bare substrate.

3.6 Grain Size Analysis of Al by IMAGE J

The distribution of grain size in SEM viewgraph was analyzed and compiled using **Image J** software, which is a public domain Java image processing program available from US National Institutes of Health (NIH). [57]The procedure of grain size analysis by Image J can be detailed as follow. First, we demarcated the grain area of SEM top-view graph as shown in Fig. 3.11. Then, the contrast of image was adjusted to black and white using Image J as shown in Fig. 3.12. After enhancing the contrast, the distribution of grain size was analyzed by using Analyze➔ Analyze particles command as shown in Fig. 3.13 with result shown in Fig.3.14.

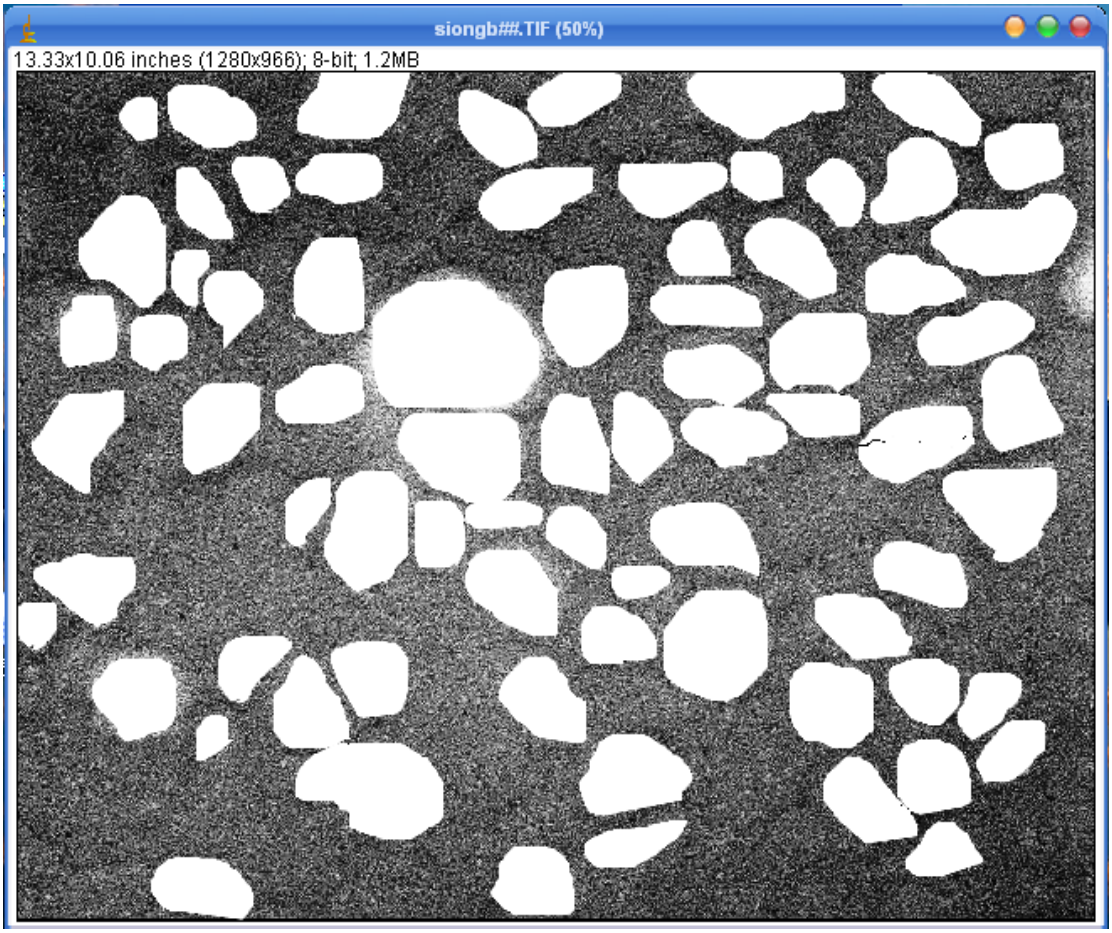

Figure 3.11 SEM image which has been demarcated the grain area.

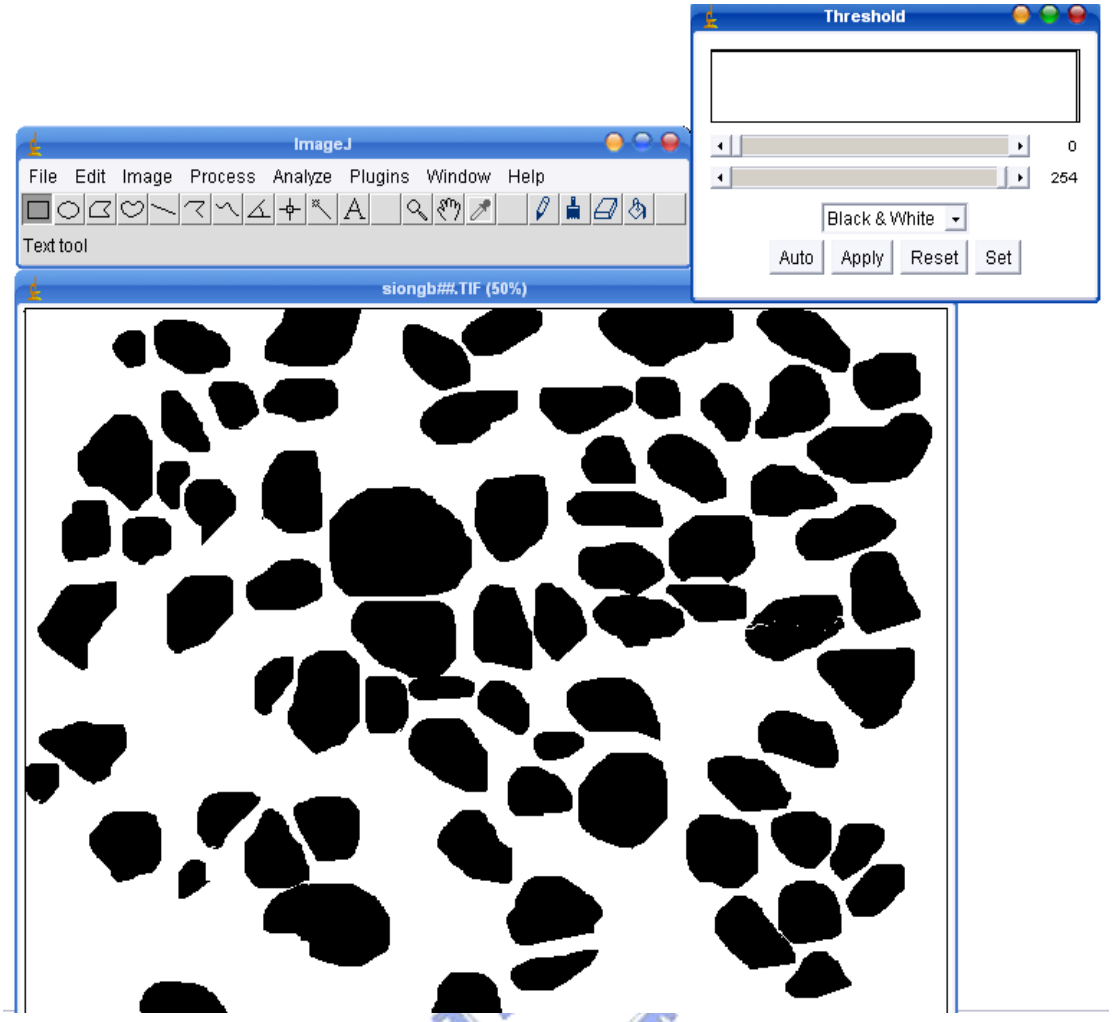

Figure 3.12 Illustration of altering interactively the brightness and contrast of the image to be relative block and white.

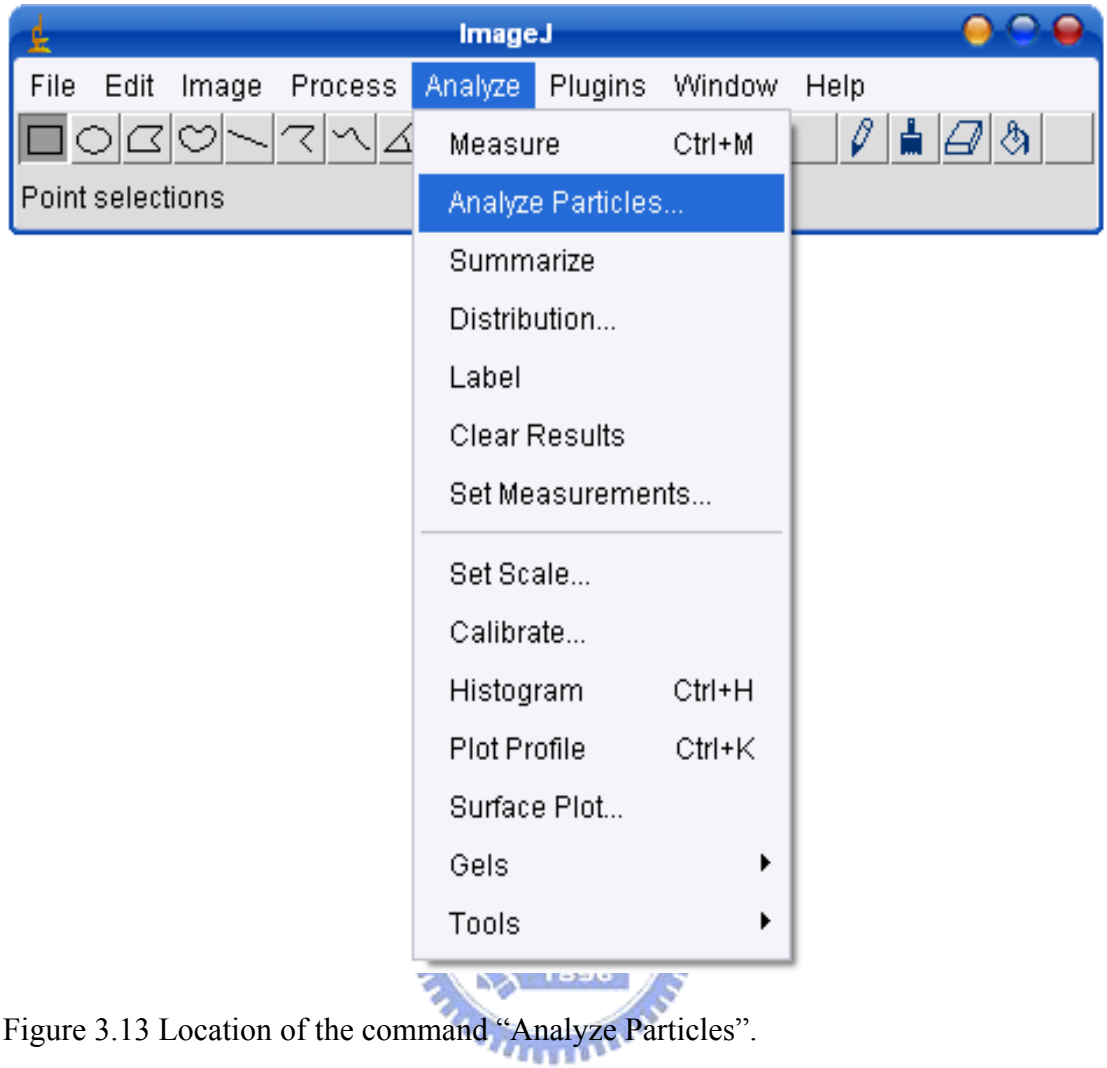

Figure 3.13 Location of the command "Analyze Particles".

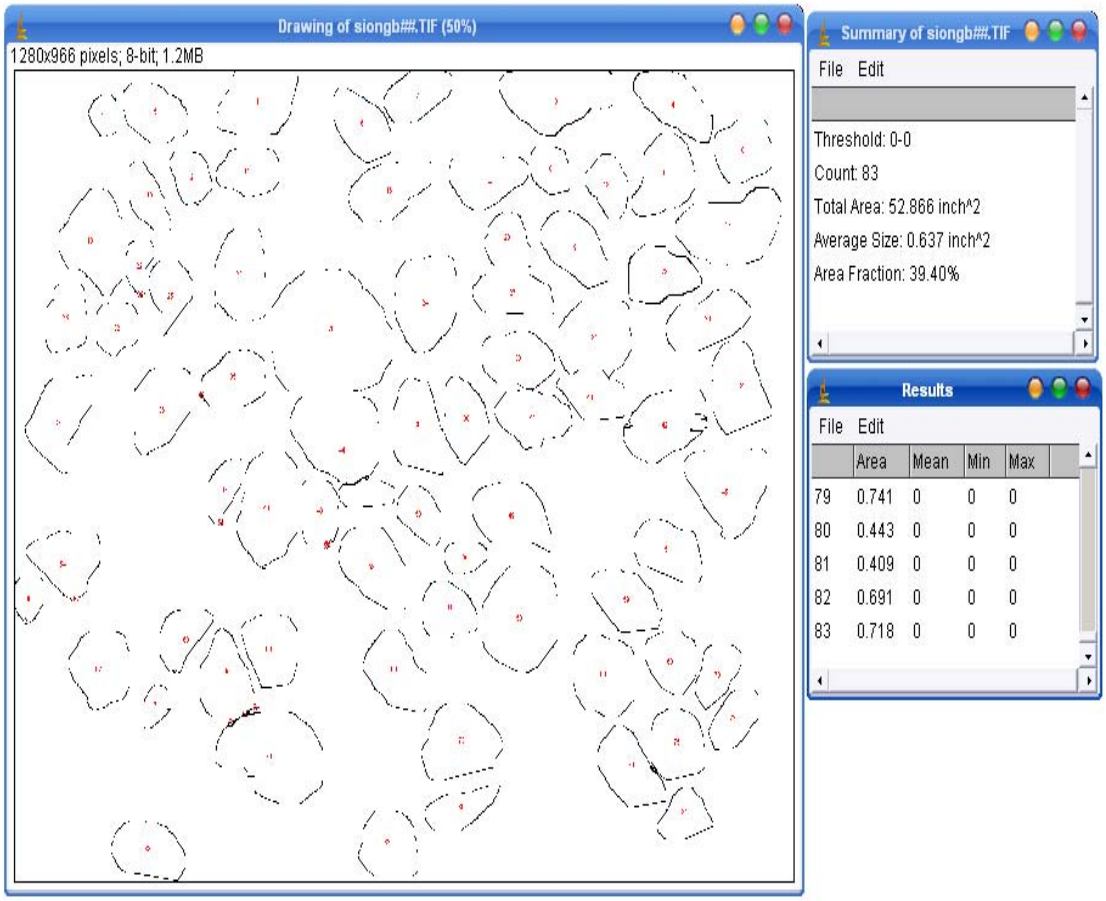

Figure 3.14 Analysis result of grain size distribution.

Chapter 4 Results and Discussion

4.1 Chemical Structure and Composition Analysis of SiO_xN_y Layers

4.1.1 Analysis by Specular Reflectance FTIR Spectroscopy

The Si-O structural information of SiO_xN_y films was first obtained from the Si-O-Si stretching vibration using specular reflectance FTIR spectroscopy. Fig. 4.1 showed Si-O-Si infrared absorption peaks of three types of passivation layer deposited at fixed substrate temperature (80 ℃): (1) pure SiO_2 (2) SiO_xN_y under low nitrogen flow rate, and (3) SiO_xN_y under high nitrogen flow rate, whose FTIR absorption peak positions were summarized in Table 4.1. The Si-O-Si absorption peak was 1208 cm^{-1} for pure SiO_2 layer, 1176 cm^{-1} for passivation films deposited under high flow rate condition, and 1171 cm^{-1} for passivation films deposited under low flow rate condition. The Si-O stretching band of SiO_xN_y films shifted to lower wavenumber with decreasing N_2 flow rate. This indicated that a change of chemical environment by the increased incorporation of Si-N bonding, whose stretching frequency was typically at 980 cm^{-1}, contributed the down-shifting of Si-O stretching bands. Moreover, it implied that the lower nitrogen flow rate generated higher nitrogen content of the oxynitride based on the Si-O infrared peak position. [56]

Table 4.1 Si-O absorption peak position of three types of passivation layer.

Passivation layer	**Absorption Peak Position (cm^{-1})**
SiO_2	1208
SiO_xN_y under high flow rate	1176
SiO_xN_y under low flow rate	1171

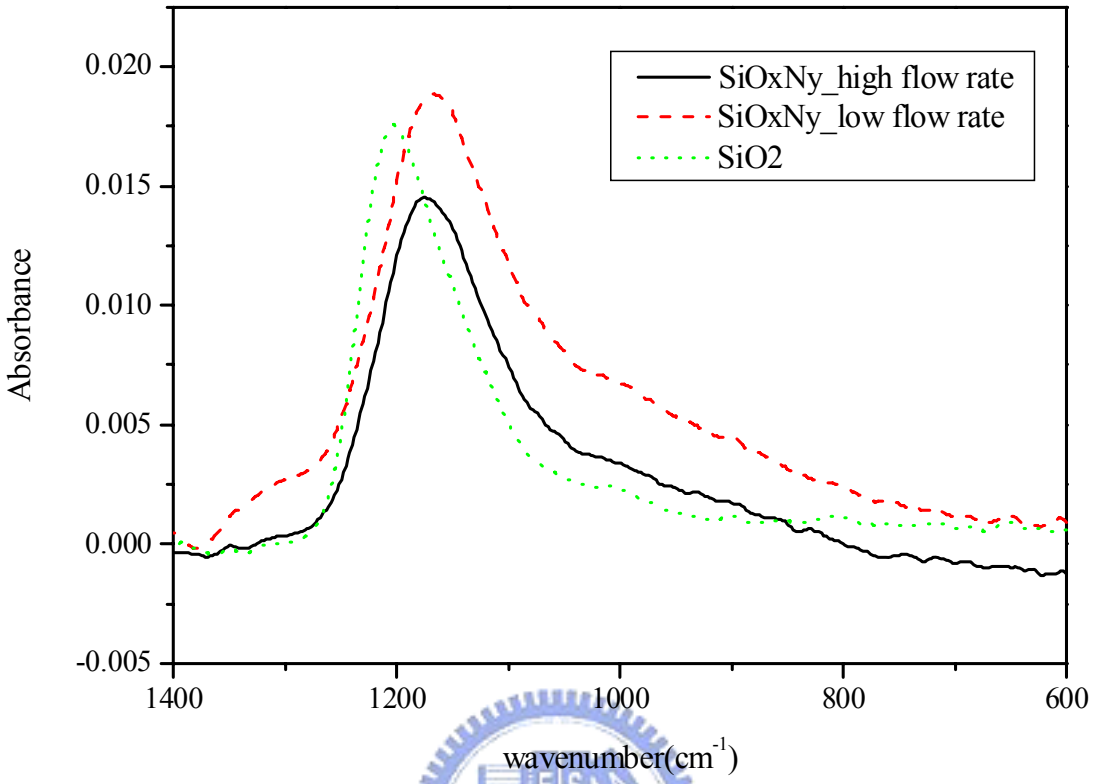

Figure 4.1 Specular reflectance FTIR spectrum of three types of passivation layer: (1) pure SiO_2, (2) SiO_xN_y under high nitrogen flow rate, and (3) SiO_xN_y under low nitrogen flow rate.

4.1.2 Composition Analysis by XPS

The XPS Si 2p, N 1s, and O 1s spectra of oxynitride films deposited under 80 ℃ and different flow rate conditions were shown in Figs. 4.2 (a) and (b). The integrated areas of these peaks, summarized in Table 4.2 and 4.3, were used to quantify the surface composition. It showed the surface composition of oxynitride films deposited under 80 ℃ and low flow rate condition was $SiO_{0.7}N_{1.9}$. In contrast, the surface composition of oxynitride films deposited under 80 ℃ and high flow rate condition was $SiO_{0.67}N_{2.0}$. Nitrogen content in films deposited under high flow rate was found to be slightly less than under low flow rate condition, which was consistent with the finding from infrared spectroscopy. It can be inferred that less N atoms could

be dissociated because the plasma energy was dispersive under high N_2 flow rate condition. Also, high flow rate yielded high chamber pressure and shorter mean free path. Hence, less N atoms could be incorporated into the passivation film. Overall, the difference in composition under various flow rate conditions was not significant.

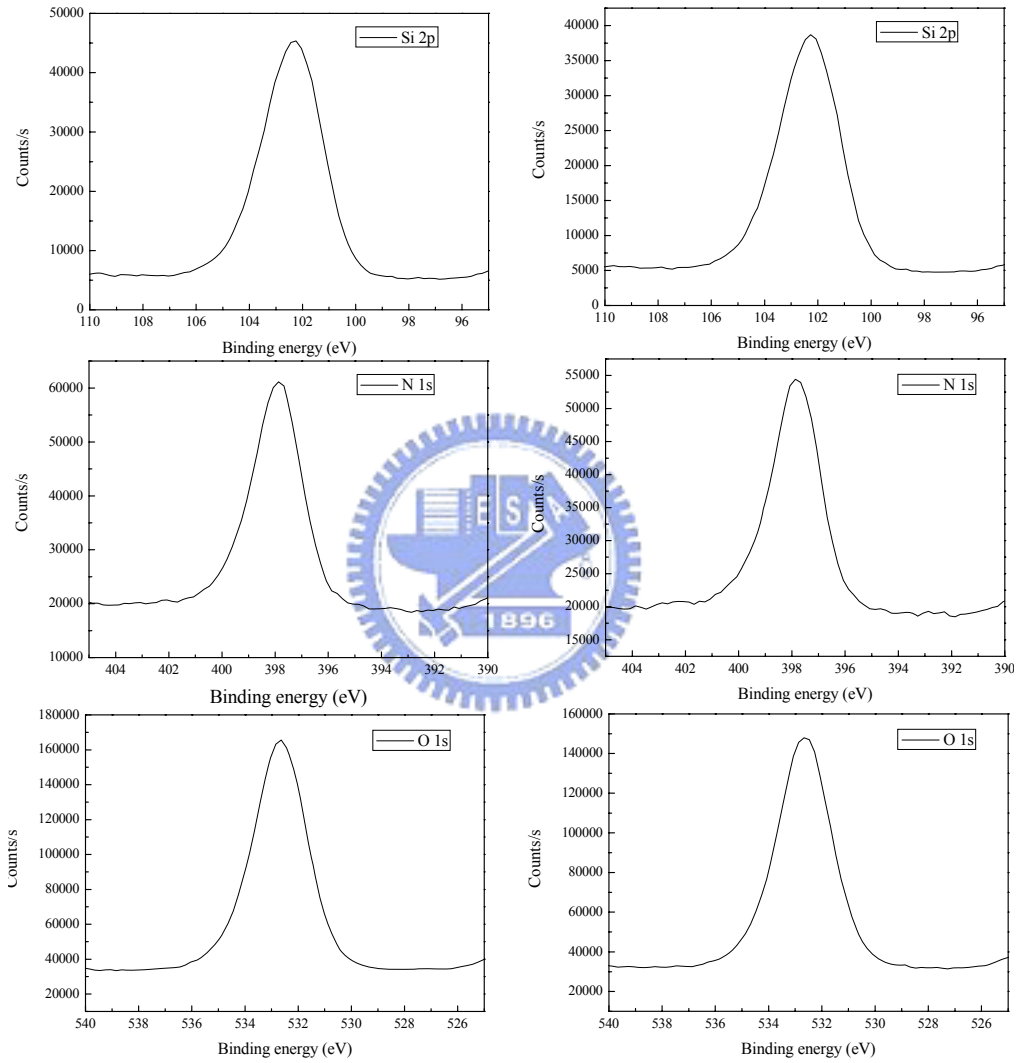

Figure 4.2 The XPS Si 2p, N 1s, and O1s spectra of oxynitride films deposited under 80 ℃ (a) low flow rate and (b) high flow rate conditions. The references of Si 2p signals: Si-Si (99.4 eV), Si-N (101.9 eV), and Si-O (103.4 eV). [58]

Table 4.2 Binding energies and composition quantification of oxynitride film deposited under 80 ℃ and low flow rate condition.

Name	Peak BE	Area	Atomic fraction (%)	Si : N : O
Si 2p	102.31	166.07	27.6	1
N 1s	397.86	114.3	19.1	0.7
O 1s	532.65	319.88	53.3	1.9

Table 4.3 Binding energies and composition quantification of oxynitride film deposited under 80 ℃ and high flow rate condition.

Name	Peak BE	Area	Atomic fraction (%)	Si : N : O
Si 2p	102.27	140.84	27.1	1
N 1s	397.80	94.98	18.2	0.67
O 1s	532.65	284.96	54.7	2.0

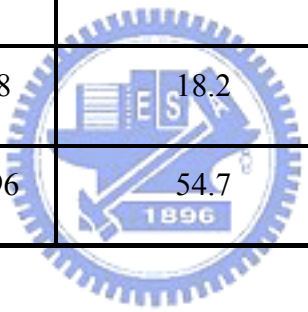

4.2 Morphology and Microstructure of Barrier Layers/Al Samples

The morphology and microstructures of silicon oxynitride/aluminum/Alq_3/glass samples were examined first by SEM. Figs.4.3 (a) and (b) showed the morphology of SiO_xN_y passivation films deposited at substrate temperature of 90℃, under high and low flow rates, respectively. Both showed not only no significant difference in the grain sizes between high and low N_2 flow rate conditions, but also no pinhole formation. However, unknown bump was observed widespread over the surface of samples by top-view SEM as shown in Fig. 4.4 (a). These widespread defects

represented by SEM in Fig. 4.5(a) were identified to be Al hillocks by electron diffraction spectrometry (EDS), whose composition was listed in Table 4.4. This indicated that large topographic changes occurred in the underlying Al film, and some of the Al hillocks broke through SiO_xN_y passivation film. These Al extrusions would cause damage in passivation layer and lead to moisture permeation. In addition, Fig. 4.4 (b) showed crack defect, which was very minor and negligible as the root-cause of moisture permeation. Thus, based on the quantity, hillock defects were the most probable root-cause for moisture permeation. In order to statistically quantify the hillock density of various SiO_xN_y films and find any correlation with moisture permeation, an Al wet etch method was employed to decorate hillock defects using aluminum wet etchant (composition: 80% phosphoric acid, 5% acetic acid, 5% nitric acid, and 10% water). Extruded Al was removed readily by Al wet etchant leaving holes as validated by SEM illustrated in Fig. 4.5 (b). Therefore, optical microscope could readily used to quantify Al hillock density together with Image J as described in Chapter 4.3.

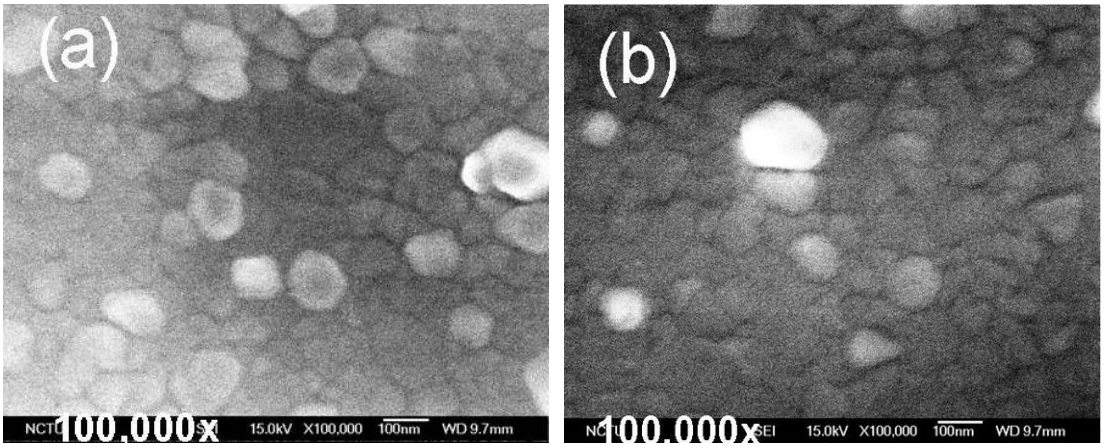

Figure 4.3 SEM top-view graphs of the SiO_xN_y films deposited at substrate temperatures 90℃: (a) under high flow rate, (b) under low flow rate.

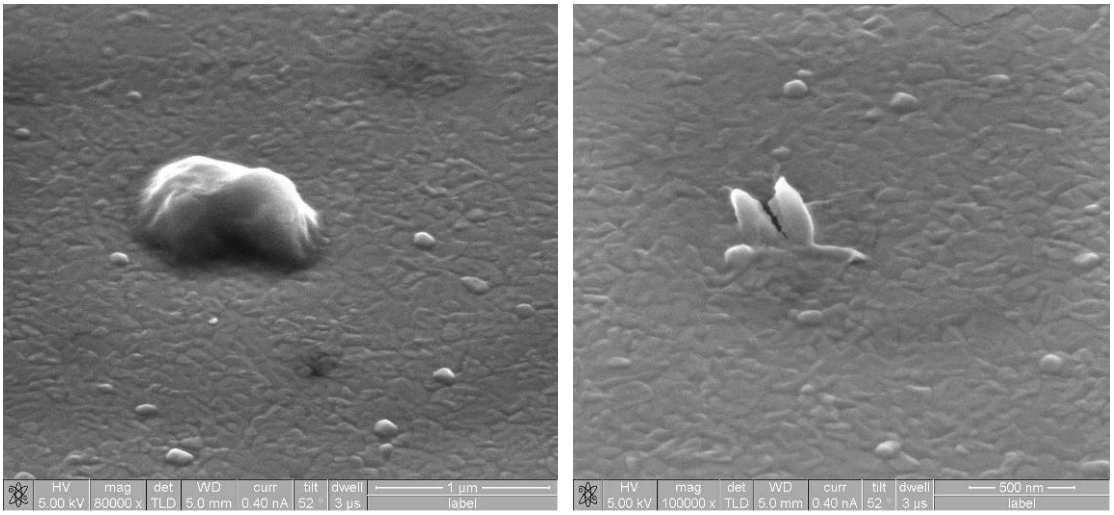

(a) (b)

Figure 4.4 SEM top-viewgraphs tilted 52º of the SiO_xN_y films: (a) unknown bump, (b) crack.

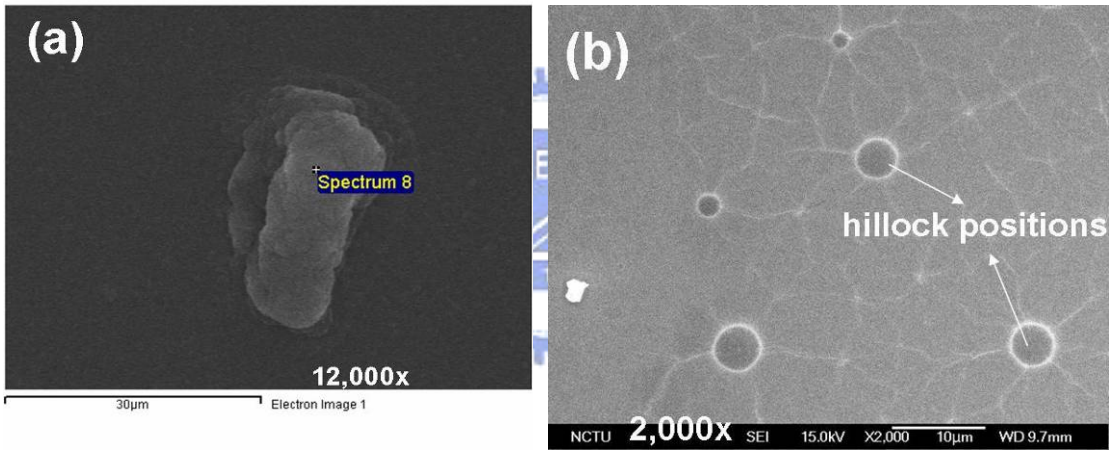

Figure 4.5 SEM photographs: (a) defects of Al hillock and (b) topography after wet etch of Al hillocks.

Table 4.4 EDS analysis of the defect shown in Fig. 4.5 (a).

Element	**Atomic %**
O K	56.03
Al K	26.09
Si K	14.34
Cl K	3.55
Total	100.00

4.3 Hillock Formation

4.3.1 Hillock Density

Hillock densities of the SiO_xN_y/Al films deposited under different flow rates and various substrate temperatures were further quantified using an Al wet etch method for defect decoration and optical microscope for inspection as shown in Figs.4.6 (a)-(f) and summarized in Table 4.5. SiO_xN_y/Al samples possessed lower Al hillock density as substrate temperature increased or flow rate increased. The correlation between hillock density and moisture permeation through SiO_xN_y/Al samples was further discussed in Chapter 4.4.

Table 4.5 Al hillock density of the SiO_xN_y/Al films deposited under different flow rate condition at various substrate temperatures.

	Hillock density (10^{-5}/μm^2)		
Substrate Temperature (℃) / **N_2 flow rate**	**60**	**80**	**90**
High	41.4	34.6	7.9
Low	74.8	40.8	14.7

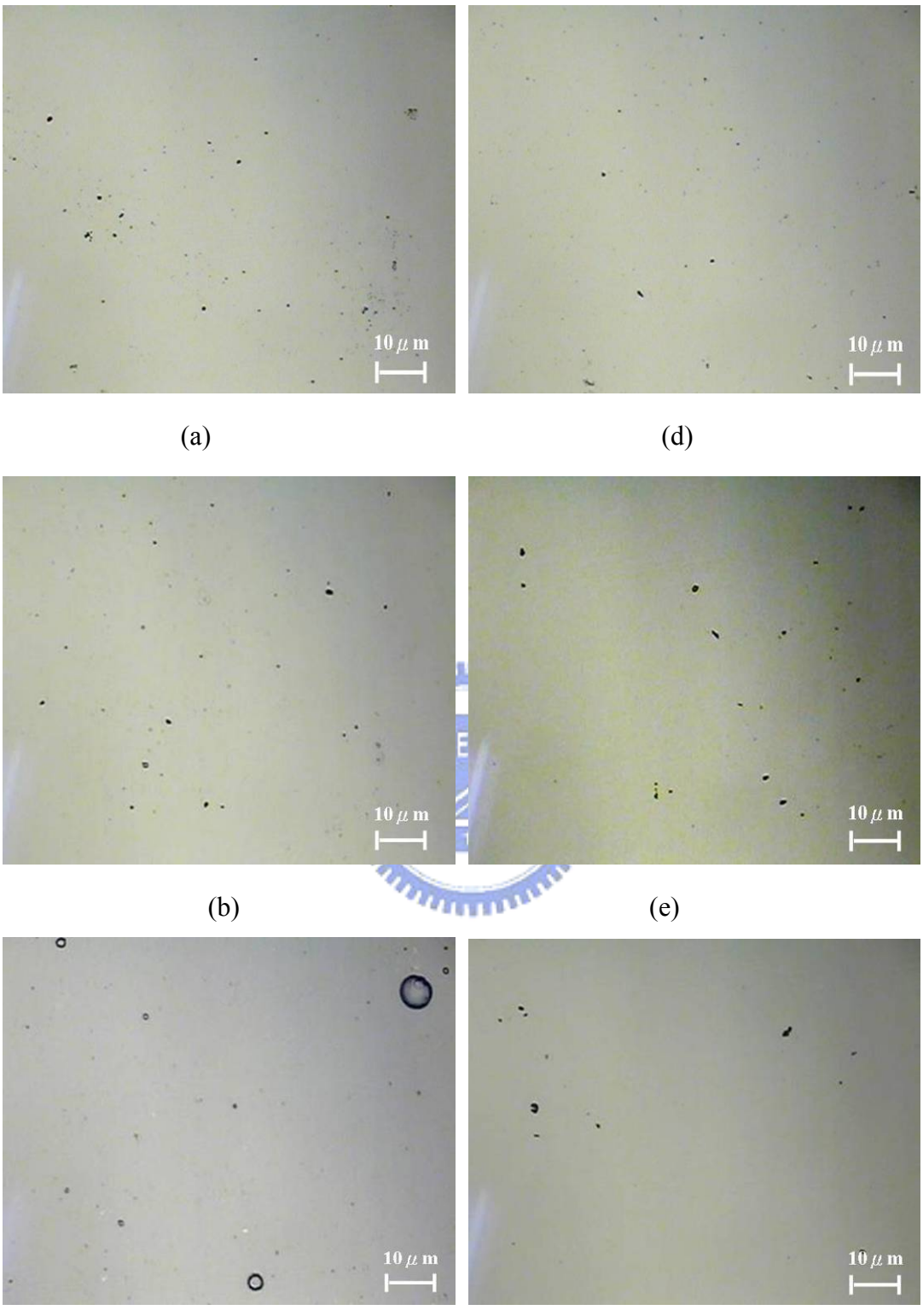

Figure 4.6 OM photographs magnified 1000x: under low flow rate at various substrate temperatures: (a) 60 ℃, (b) 80℃, and (c) 90℃ and under high flow rate at various substrate temperatures: (d) 60 ℃, (e) 80℃, and (f) 90℃.

4.3.2 Hillock Height

The maximum height of hillocks of silicon oxynitrides deposited under various deposition conditions (flow rates and deposition temperatures) were characterized by AFM as shown in Figs. 4.7 (a)-(f) and summarized in Table 4.6. As substrate temperature increased, the hillock height increased. In contrast, the maximum hillock heights in the films deposited under high flow rate conditions were slightly higher than those deposited under low flow rate conditions.

Table 4.6 The maximum height of hillock of the SiO_xN_y/Al films deposited under different flow rate condition at various substrate temperatures.

	Max. height (nm)		
Substrate Temperature (℃) / **N_2 flow rate**	**60**	**80**	**90**
High	34.8	54.2	70.6
Low	24.8	38.1	68.6

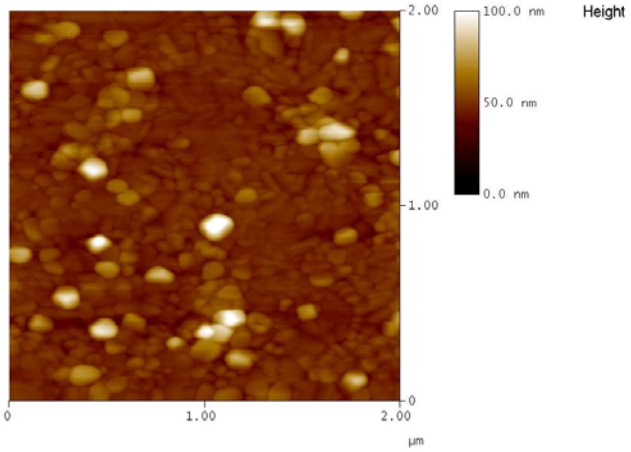

(a)

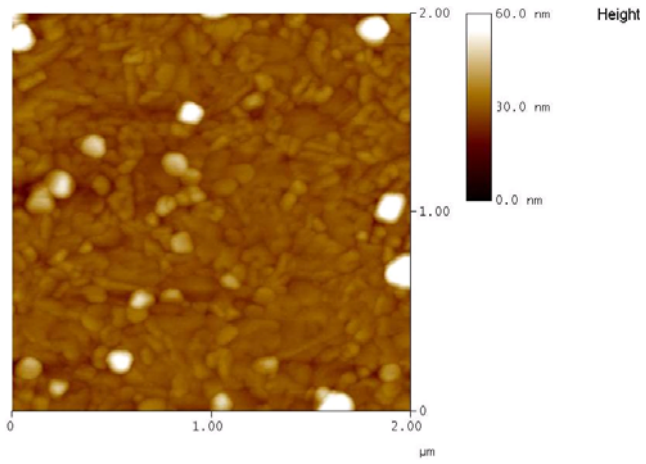
Height
60.0 nm
30.0 nm
0.0 nm
2.00
1.00
0
0
1.00
2.00
μm

(b)

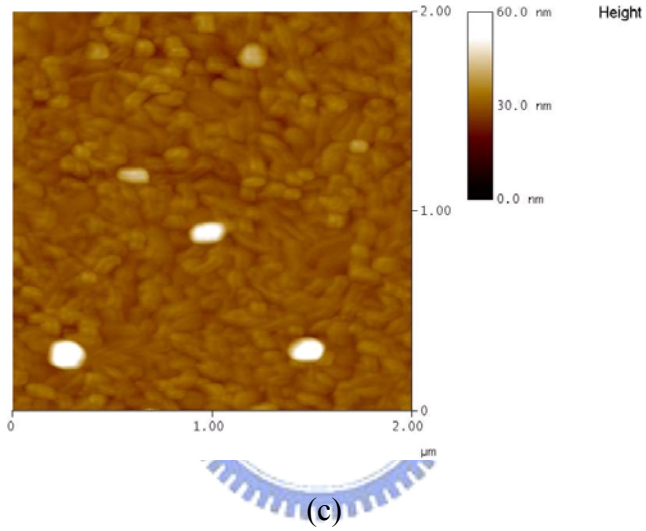
Height
60.0 nm
30.0 nm
0.0 nm
2.00
1.00
0
0
1.00
2.00
μm

(c)

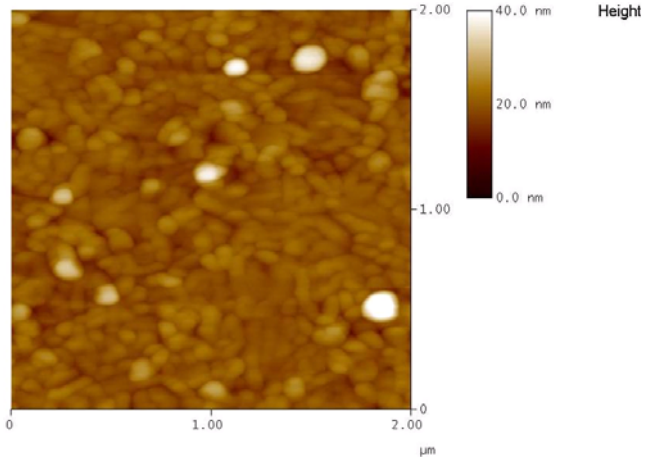
Height
40.0 nm
20.0 nm
0.0 nm
2.00
1.00
0
0
1.00
2.00
μm

(d)

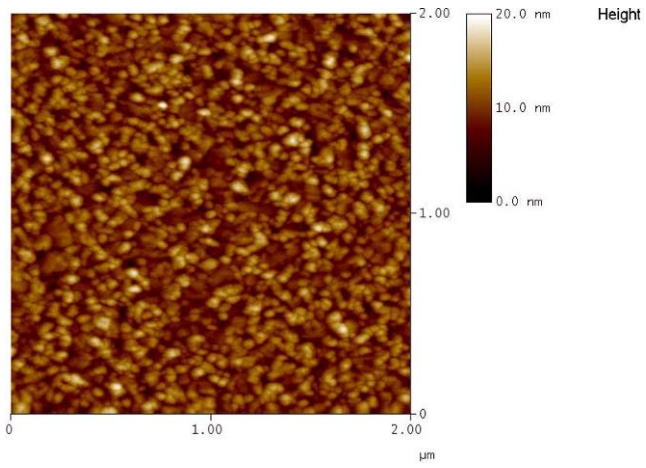

(e)

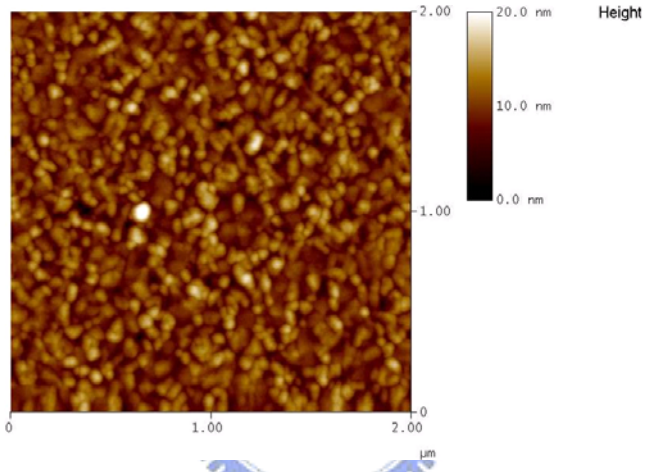

(f)

Figure 4.7 AFM 2D images (2μm×2μm): (a) substrate temperature is 90℃ under high flow rate, (b) substrate temperature is 90℃ under low flow rate, (c) substrate temperature is 80℃ under high flow rate, (d) substrate temperature is 80℃ under low flow rate, (e) substrate temperature is 60℃ under high flow rate, and (f) substrate temperature is 60℃ under low flow rate.

4.4 Correlation between Moisture Resistance and Hillock Formation

The moisture barrier effectiveness of these oxynitrides was qualitatively measured by calcium button test as shown by Figs. 4.8 (a) and (b) for films deposited under high and low flow rates, respectively. The qualities of the moisture barrier layers were determined by the amount of calcium oxidized or hydrolyzed, which turned into bright spots. It showed oxynitride films deposited under high N_2 flow rates exhibited better moisture barrier effectiveness. By combining the results of Fig. 4.8 and Table 4.5, excellent correlation between hillock density and moisture permeation through SiO_xN_y/Al samples was found. This indicated Al hillock was the culprit of moisture permeation in the passivation layer of SiO_xN_y/Al stack.

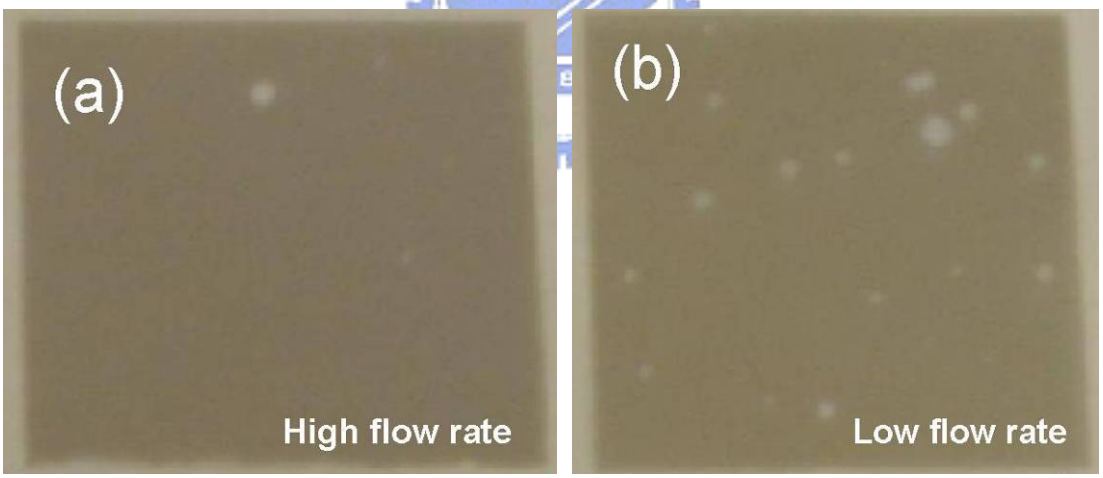

Figure 4.8 Calcium button test of SiN_xO_y barrier films deposited under (a) high flow rate and (b) low flow rate.

In summary, SiO_xN_y films prepared under high substrate temperature and high N_2 flow rate showed the lowest hillock density, but possessed the tallest Al hillock defects height. Excellent correlation between hillock density and moisture permeation through SiO_xN_y/Al samples was established, indicating Al hillock was the culprit of

moisture permeation in the passivation layer. As a result, the improved moisture resistance of SiO_xN_y deposited under high flow rate and high temperature conditions could be attributed to its lower hillock density if a single passivation layer was used. Since multiple layers were often employed to deliver the required moisture resistance, the height of hillocks should be taken into consideration for the selection of deposition conditions. For example, more number of barrier layers at fixed thickness was needed to conformally seal the hillocks in SiO_xN_y/Al deposited under high flow rate and high temperature conditions because their hillock heights were taller even though their hillock densities were lower. Therefore, the hillock height and density shall be taken into consideration in the selection of deposition conditions of SiO_xN_y onto Al layer pending on the film thickness, stress and number of layers.

In the following sections, the mechanism of Al hillock formation in SiO_xN_y/Al stack at temperature as low as 60 ^oC, would be further investigated and proposed. Grain size of Al film as cathode and the thermal stress of SiO_xN_y passivation layer would be first examined. The mechanism of hillock formation and their effects on the hillock density and height would be then discussed.

4.5 Al Grain Size

XRD was employed to characterize the crystallite sizes of aluminum films in the SiO_xN_y/Al/glass stack post SiO_xN_y deposition using the full width at half maximum of the dominant Al (111) peak and Scherrer's equation (3.1). Figs. 4.9 and 4.10 showed Al (111) peaks in SiO_xN_y/Al/glass stack for SiO_xN_y films prepared at high flow rate and low flow rate conditions, respectively. Moreover, the crystallite sizes of the Al films at various SiO_xN_y deposition conditions were summarized in Table 4.7. It showed that films prepared under high substrate temperature possessed

larger crystallite sizes (~60 nm) than the ones under low temperature conditions (~40 nm). It implied that the energy derived from SiO_xN_y deposition induced grain growth in the underlying Al film.

In this study, Al film was first deposited onto glass plate at 60 ^oC using the same modified ion beam deposition system. The microstructure of Al film was expected to be about the same as that in SiO_xN_y/Al deposited also at 60 ^oC as illustrated in Fig. 4.12.

In the modified ion beam deposition system, Al/glass substrate was kept at room temperature (~20 ^oC) prior to the deposition of SiO_xN_y layer. The deposition temperature calibrated at the top of glass plate was controlled by the lateral moving speed of glass plate. In order to avoid any damage onto the OLED devices, whose Alq_3 layer cannot survive temperature > 100 ^oC, the deposition temperatures in this study were controlled at 60, 80 and 90 ^oC. However, the surface temperature of Al film during SiO_xN_y deposition was expected to be higher due to energy transfer by the evaporated atoms and molecules. The surface temperature could be estimated by the energy conservation described by Eq. 4.1.

$$\Delta H_{Al} + \Delta H_{barrier} = 0 \quad (4.1)$$

$$\Delta H = mS\Delta T \quad (4.2)$$

where m is the mass, S is the heat of capacity, while ΔT is the difference between the final and initial temperatures for a process. In addition, S_{Al}=0.217 cal/g℃ and $S_{barrier}$=0.2 cal/g℃.

Hence, the Al surface temperature was estimated to be 247 ℃ and 361 ℃ for glass substrate temperature controlled at 60 ℃ and 80 ℃, respectively. Assuming the particle energy arriving to the surface of OLED structure was 25 eV as illustrated by Fig. 3.2 in the modified ion beam evaporation system, the temperature at Al surface was 387℃, which was in line with the estimation by Eq. 4.1. It was perceived that

these surface temperatures (T/T_m for Al ~0.32-0.55) were relative high to be able to drive additional Al grain growth during SiO_xN_y deposition.

This trend of grain size measured by XRD was closely related with the domains observed by top-view SEM as shown in Figs.4.11 (a) through (f). The cross-sectional microstructure of SiO_xN_y/Al/glass stack was further examined by a TEM as illustrated in Fig. 4.12. Al films exhibited columnar structure with width between 50 and 100 nm, while SiO_xN_y passivation showed amorphous phase and conformal coverage onto the underlying Al film. It demonstrated the morphology of SiO_xN_y passivation observed by top-view SEM was in response to the planar grain size of aluminum and, in some cases, hillocks. Then, the distribution of Al grain size in SEM image was analyzed by using IMAGE J software. The results of grain size distributions were listed in Figs. 4.13 (a) through (d). Fig. 4.13 (a) showed films deposited under 60 ℃ exhibited the smallest grain size and concentrated in 40-60 nm region. There was not much difference in different gas flow rates under 60℃. Fig. 4.13 (b) showed that the films deposited under 80℃ and high flow rate condition possessed grain size concentrated in 40-60 and 60-80 (nm) regions. However, the films deposited under 80℃ and low flow rate condition exhibited wide grain distribution in the range of 40-180 nm. Fig. 4.13 (c) showed that the films deposited under 90℃ and two different flow rate conditions exhibited the grain sizes concentrated in 80-120 nm. Fig. 4.13 (d) summarized the grain size distributions of Al films under the deposition of SiOxNy layer at different substrate temperatures but the ssme high gas flow rate. It showed there was not much difference in grain size distribution under 80 and 90℃, but it was apparently different at 60℃ compared to those at 80 and 90℃. Since the crystallite sizes of aluminum which derived from XRD is the average value, the distribution of Al grain size in SEM image, which analyzed by using IMAGE J software, can help us to analyze the Al grain boundary

size more quantitatively.

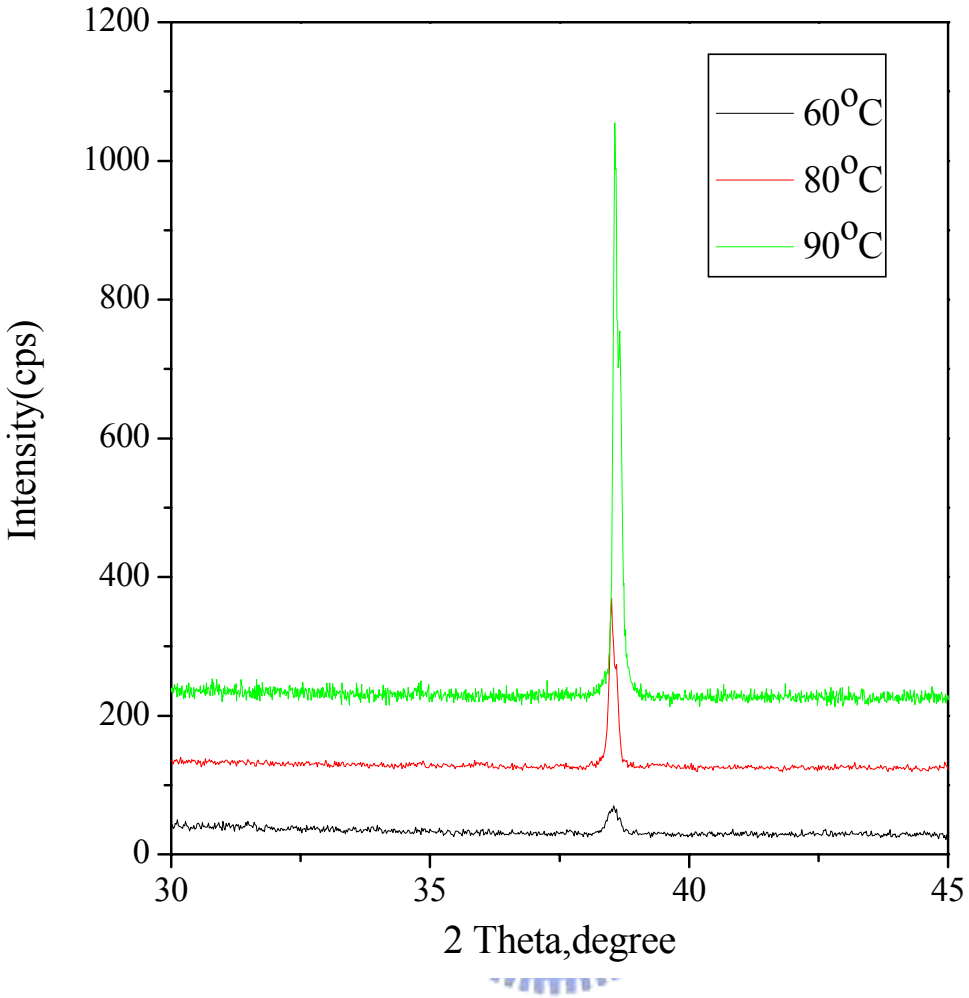

Figure 4.9 X-ray diffraction pattern of SiO_xN_y/Al/Alq_3/glass sample, where SiO_xN_y was deposited under high flow rate at various substrate temperatures.

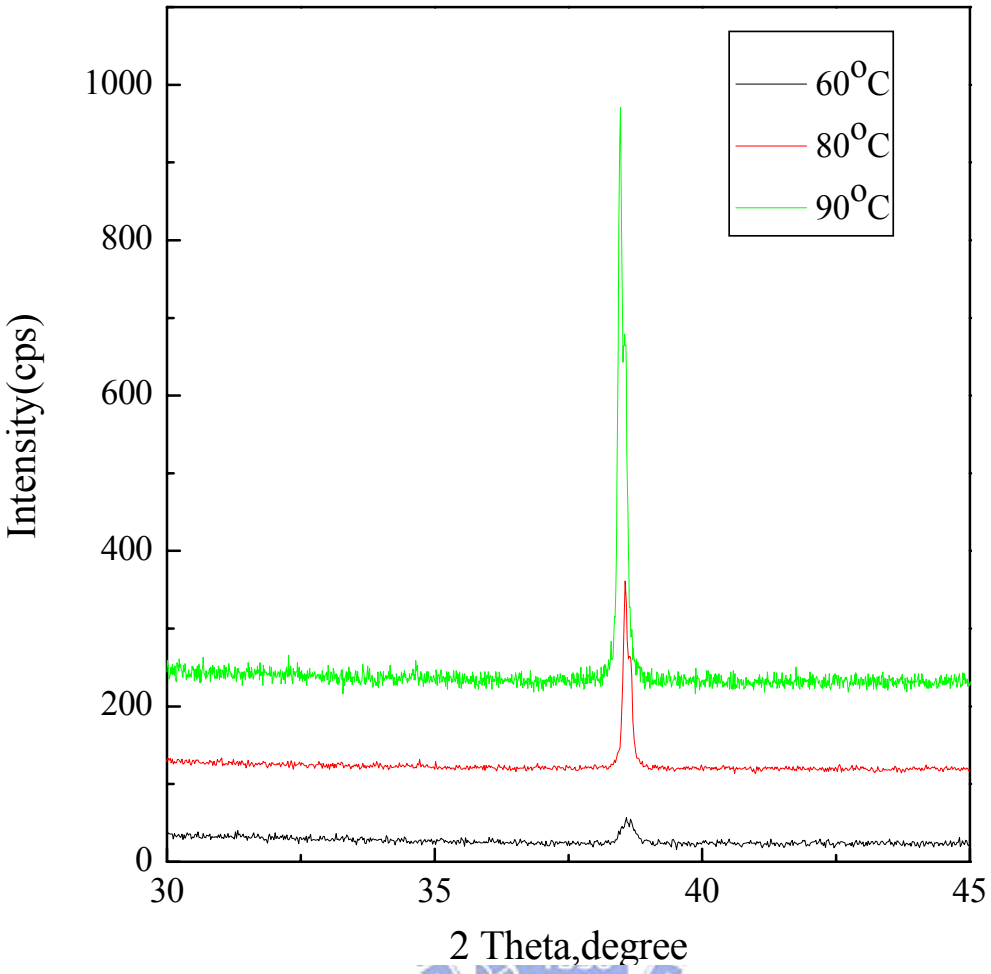

Figure 4.10 X-ray diffraction pattern of SiO_xN_y/Al/Alq_3/glass, where SiO_xN_y was deposited under low flow rate at various substrate temperatures.

Table 4.7 The crystallite sizes of Al in SiO_xN_y/Al/Alq_3/glass sample stack, where SiO_xN_y was deposited under different flow rate condition at various substrate temperatures.

λ=1.54Å		**θ**	**FWHM (B)**	**Grain size (nm)**
60 ℃	**Low flow rate**	19.33	0.203π/180	41
	High flow rate	19.27	0.228 π/180	37
80 ℃	**Low flow rate**	19.28	0.146π/180	58
	High flow rate	19.25	0.148π/180	57
90 ℃	**Low flow rate**	19.23	0.146π/180	58
	High flow rate	19.29	0.148π/180	57

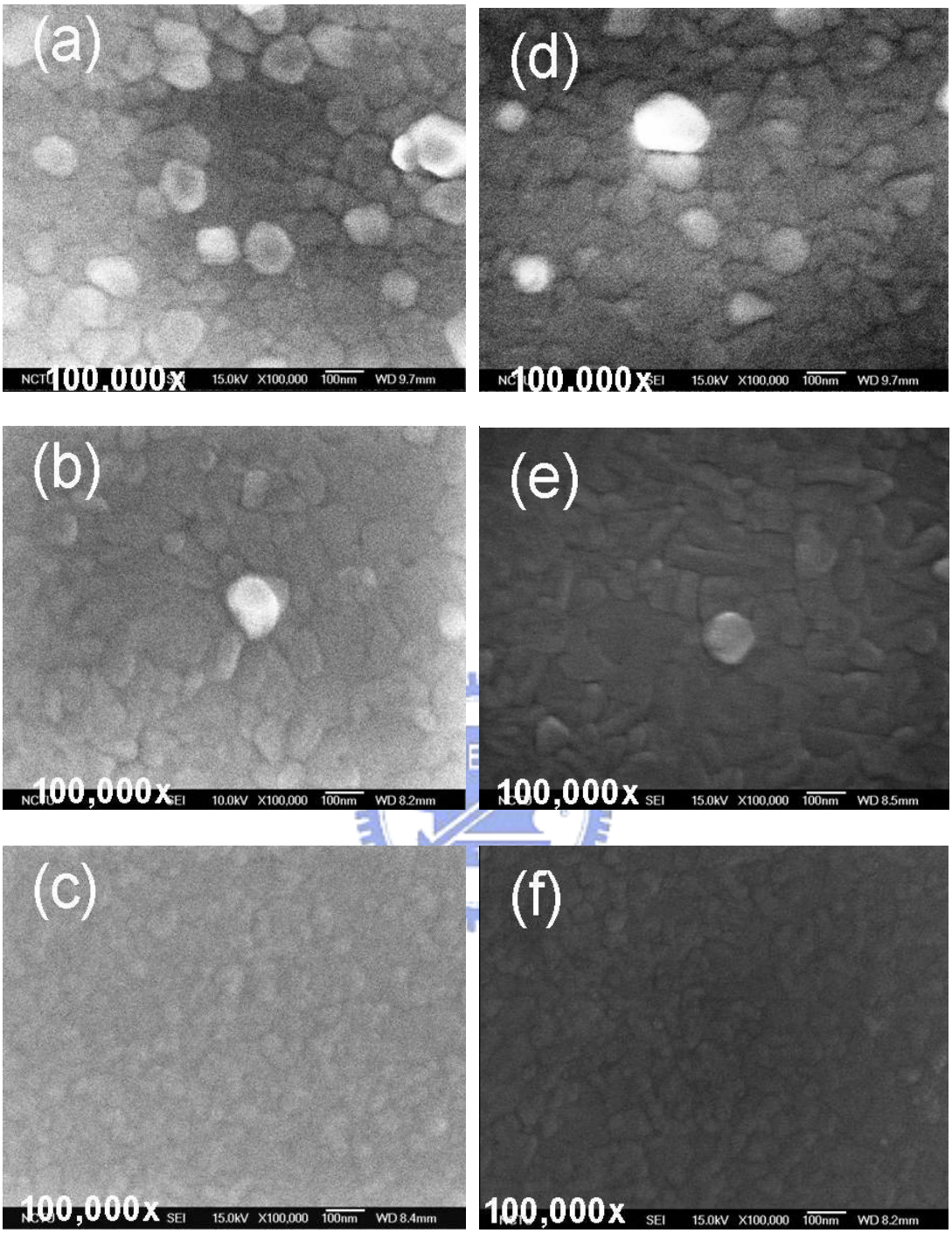

Figure 4.11 SEM top-view graphs of the SiO_xN_y films deposited under high flow rate at various substrate temperatures: (a) 90 ℃, (b) 80℃, and (c) 60℃ and under low flow rate at various substrate temperatures: (d) 90 ℃, (e) 80℃, and (f) 60℃.

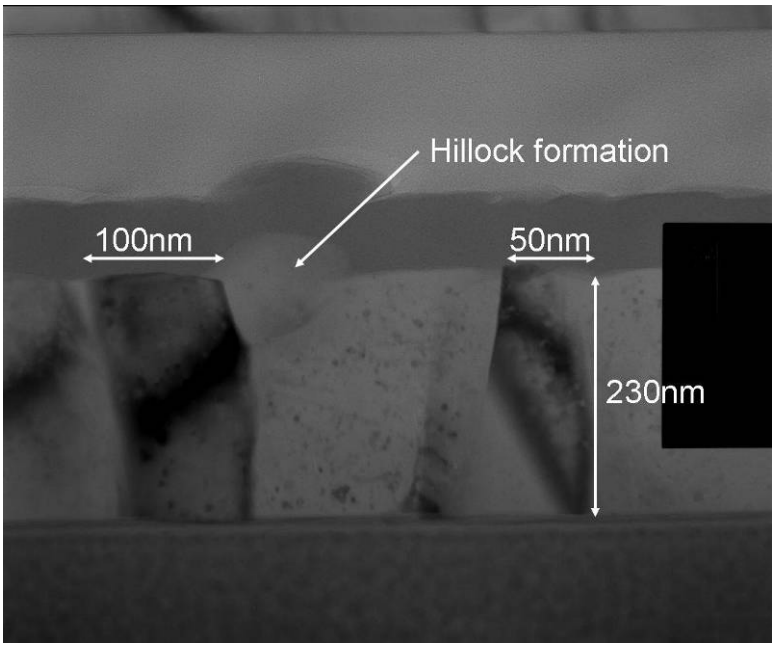

Figure 4.12 Cross-sectional TEM photograph of SiO_xN_y/Al/Alq_3/glass stack for SiO_xN_y films prepared at high flow rate and substrate temperature 60℃ condition.

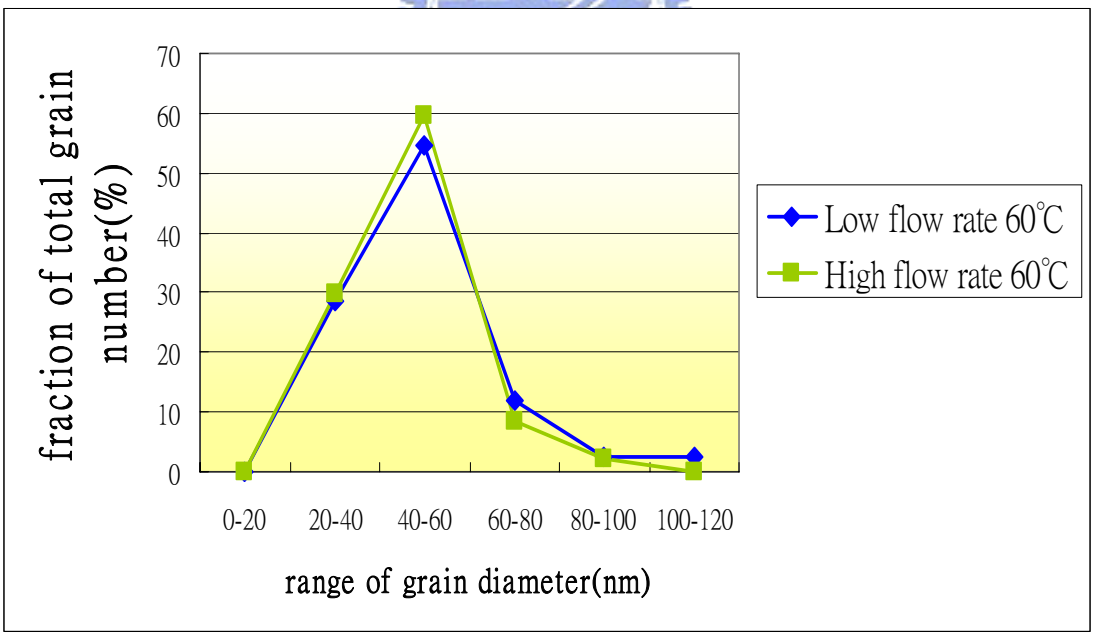

(a)

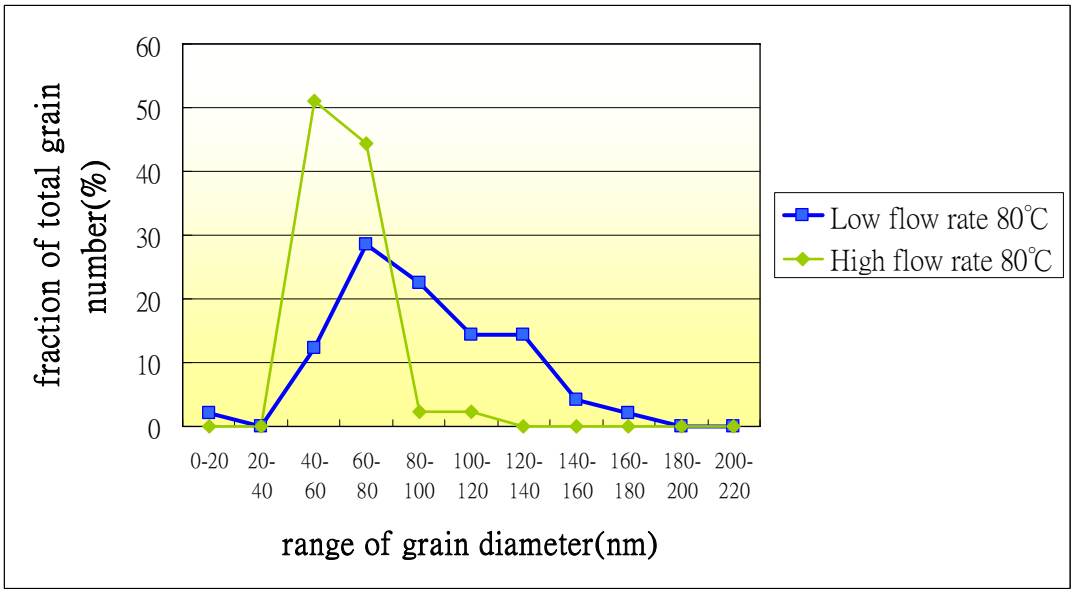
fraction of total grain number(%)
60
50
40
30
20
10
0
0-20
20-40
40-60
60-80
80-100
100-120
120-140
140-160
160-180
180-200
200-220
range of grain diameter(nm)
Low flow rate 80℃
High flow rate 80℃

(b)

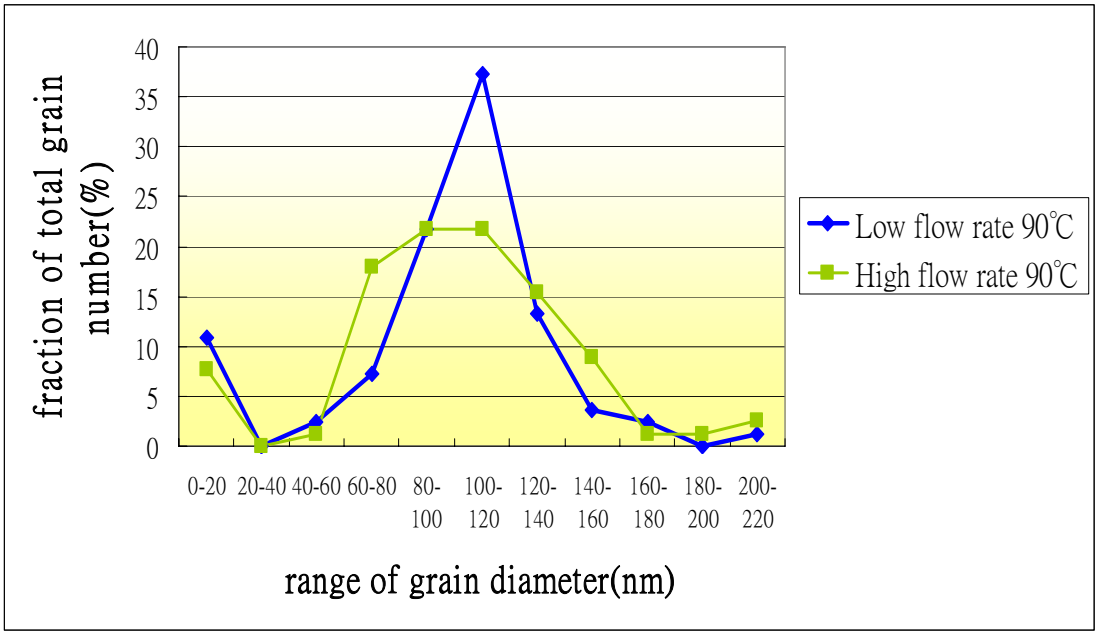
fraction of total grain number(%)
40
35
30
25
20
15
10
5
0
0-20
20-40
40-60
60-80
80-100
100-120
120-140
140-160
160-180
180-200
200-220
range of grain diameter(nm)
Low flow rate 90℃
High flow rate 90℃

(c)

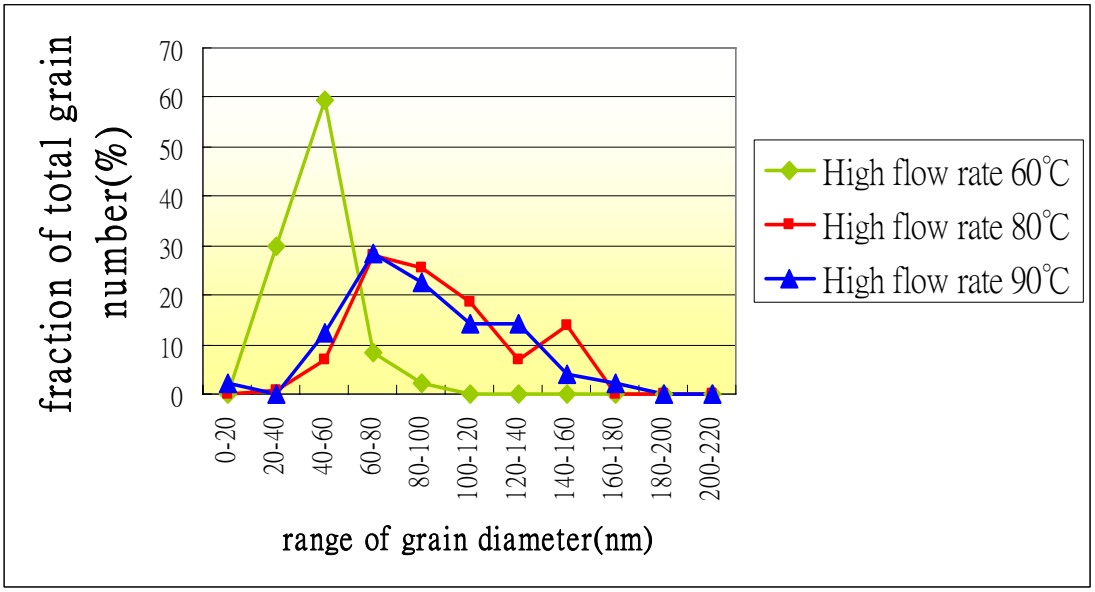

(d)

Figure 4.13 Al grain size distributions obtained fromSEM image: (a) SiO_xN_y films deposited under 60℃ and two different gas flow rate conditions. (b) films deposited under 80℃ and two gas flow rate conditions. (c) films deposited under 90℃ and two gas flow rate conditions. (d) films deposited under different substrate temperature and high flow rate conditions.

4.6 Stress Analysis

4.6.1 Young's Modulus of Substrates

Since Young's modulus of the glass substrate is a critical parameter in the Stoney's equation (3.3) for deriving the stress by bending beam system, nanoindentation was employed to measure the modulus. The modulus as function of displacement was illustrated in Fig. 4.14. The mean modulus of the glass substrate (E_s) was 79.9 GPa.

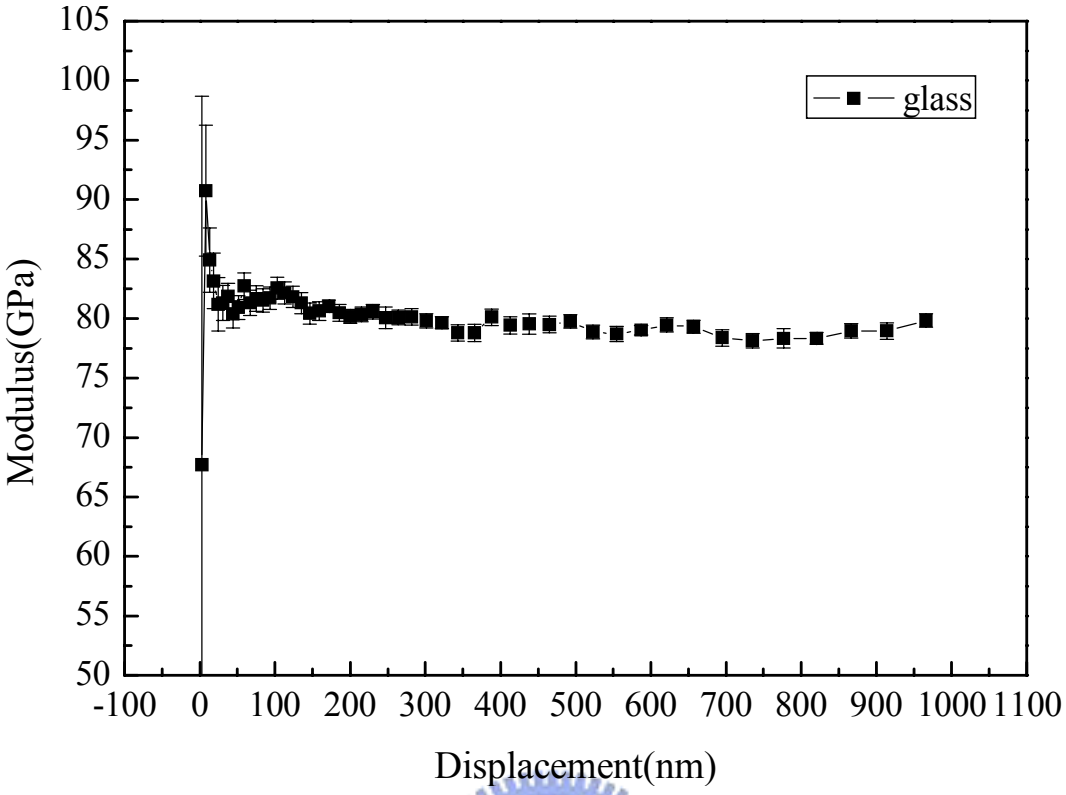

Figure 4.14 Modulus vs. displacement of the glass substrate.

4.6.2 As-deposited stress in thin film Al, SiO_xN_y/Al and SiO_xN_y

Bending beam technique has been employed to measure the stress of SiO_xN_y films as a function of temperature from room temperature to 200 ^oC based on the change of radius of the substrate and substitute to Stoney's equation (3.6). As-deposited stresses of SiO_xN_y/Al in four representative samples, which were the initial stress obtained at room temperature prior to thermal cycling, were summarized in Table 4.8. All as-deposited SiO_xN_y/Al stacked films exhibited compressive stress ranging from -40 to -180 MPa. In particular, SiO_xN_y films deposited under high flow rate conditions yielded higher compressive stress in the SiO_xN_y/Al stack than those under low flow rate conditions. In addition, films deposited at 80 ^oC yielded higher compressive stress in the SiO_xN_y/Al stack than those deposited at 60 ^oC. Our next step is to delineate the specific stress in the SiO_xN_y barrier layers. Since each

layer imposes a separate bending moment and these moments are additive, the stress of the overlaying SiO_xN_y layer can be calculated by the following equation provided the stress of aluminum film and thicknesses of SiO_xN_y and Al are known:

$$\sigma_{barrier} = \frac{\sigma_{ave}(t_{barrier} + t_{Al}) - \sigma_{Al} t_{Al}}{t_{barrier}} \quad (4.3)$$

where σ_{ave} is the average stress of the bi-layer film, $t_{barrier}$ and t_{Al} are the thicknesses of the SiO_xN_y layer and Al film, respectively.

The as-deposited stress of aluminum film, σ_{Al} was -101MPa illustrated by Fig. 4.15. The compressive stress in Al film was presumably caused by external stress during deposition and by small grain deposited at low temperatures. [10][11] As a result, the as-deposited stresses of SiO_xN_y films could be delineated using Equation (4.1) and summarized in Table 4.9. For deposition temperature at 80 ^oC, the discrete stress of SiO_xN_y layer under high flow rate was relatively high compressive stress, about -443 MPa, while low flow rate condition resulted in slightly compressive stress, about -157MPa. In contrast, the discrete stresses of SiO_xN_y layers deposited at 60 ^oC were tensile. Specifically, SiO_xN_y layer exhibited about +4 MPa tensile stress when deposited under high flow rate, and was about +204 MPa when deposited under low flow rate. It indicated that SiO_xN_y film stress changed from tensile to compressive when deposition temperature was increased from 60 ^oC to 80 ^oC. The compressive stress in SiO_xN_y film was presumably caused by dense structure which deposited at high temperature. The tensile stress in SiO_xN_y film was presumably caused by loose structure which deposited at low temperature. In general, higher substrate temperature tended to form a film with denser structure and lower substrate temperature tended to form a film with low density. [26]

Type of thin film stress and its value could be controlled by changing deposition conditions, substrate temperature and gas flow rate. In comparison, silicon

oxide films deposited by sputtering exhibited high compressive stress in the range from -0.4 to -1.5 GPa due to the extensive ion bombardment [54], while the stress of SiO_xN_y deposited by PECVD technique can control the stress to near 0 MPa by adjusting deposition conditions. [55] In this study, the as-deposited stresses of SiO_xN_y film prepared by modified ion beam evaporation technique were lower than those by sputtering, but still higher than those prepared by PECVD. Moreover, the as-deposited stresses of SiO_xN_y films could be controlled in the range of -443 to +204 MPa by adjusting the N_2 flow rates and deposition temperatures.

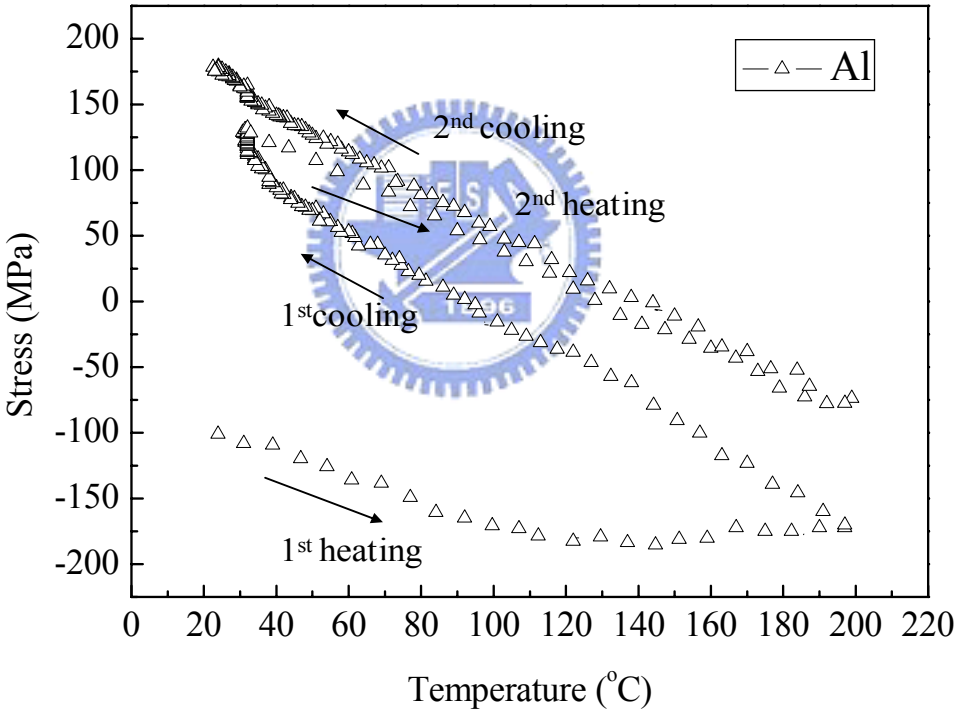

Figure 4.15 Stress vs. annealing temperature of 200 nm Al films.

Table 4.8 As-deposited stress of 50 nm SiO_xN_y/200 nm Al for SiO_xN_y films deposited under different flow rate conditions at various substrate temperatures.

	As-deposited stress (MPa)	
Substrate Temperature (℃) / N_2 flow rate	60	80
High	-80	-180
Low	-40	-114

Table 4.9 The as-deposited stress of SiO_xN_y films deposited under different flow rate conditions and various substrate temperatures.

	As-deposited stress (MPa)	
Substrate Temperature (℃) / N_2 flow rate	60	80
High	+4	-443
Low	+204	-157

4.6.3 Stress during Thermal Cycle

Thermal stresses of SiO_xN_y/Al stack as a function of temperature (20 – 200 ^oC) using bending beam technique were shown in Figs. 4.16 (a) and (b) for SiO_xN_y films deposited at 60 ^oC and 80 ^oC, respectively. For deposition temperature at 60 ^oC, the as-deposited stress at room temperature was compressive -40 and -80 MPa for high flow and low flow rate conditions, respectively. During the first heating cycle, the stress became more compressive stress because of the high thermal expansion coefficient of Al films. Furthermore, the slopes in 120 – 160 ^oC were almost the same as the 2nd cycle and gradual, due to the unstable Al structural reconstruction at high

temperature to attain dense state. The second cycle revealed elastic behavior along the decreasing temperature of the first cycle. Film stress was relaxed from -80 MPa to -43 MPa after thermal cycling between 20 and 200 ^{o}C due to relaxation of Al and SiO_xN_y films.

In contrast, films deposited at high deposition temperature, 80 ^{o}C experienced larger stress relaxation compared to the films deposited at low temperature, 60 ^{o}C. Also the extents of grain growth or hillock growth of Al in SiO_xN_y/Al stack after thermal cycling were quite different as shown in Fig.4.17 (a) for SiO_xN_y films deposited at 60 ℃ and Fig.4.17 (b) for the films deposited at 80℃, respectively. It was found that films deposited at high temperature underwent more grain growth or hillock growth toward the surface compared to the films deposited under low temperature conditions. Grain and hillock growth are both the behavior of stress relaxation. [11] Since Al films underwent more grain growth or hillock growth during the deposition of SiO_xN_y layer under high temperature, they experienced larger stress relaxation compared to the SiO_xN_y films deposited under low temperature. It indicated that the actual stress existing in thin Al film was higher than the measured value.

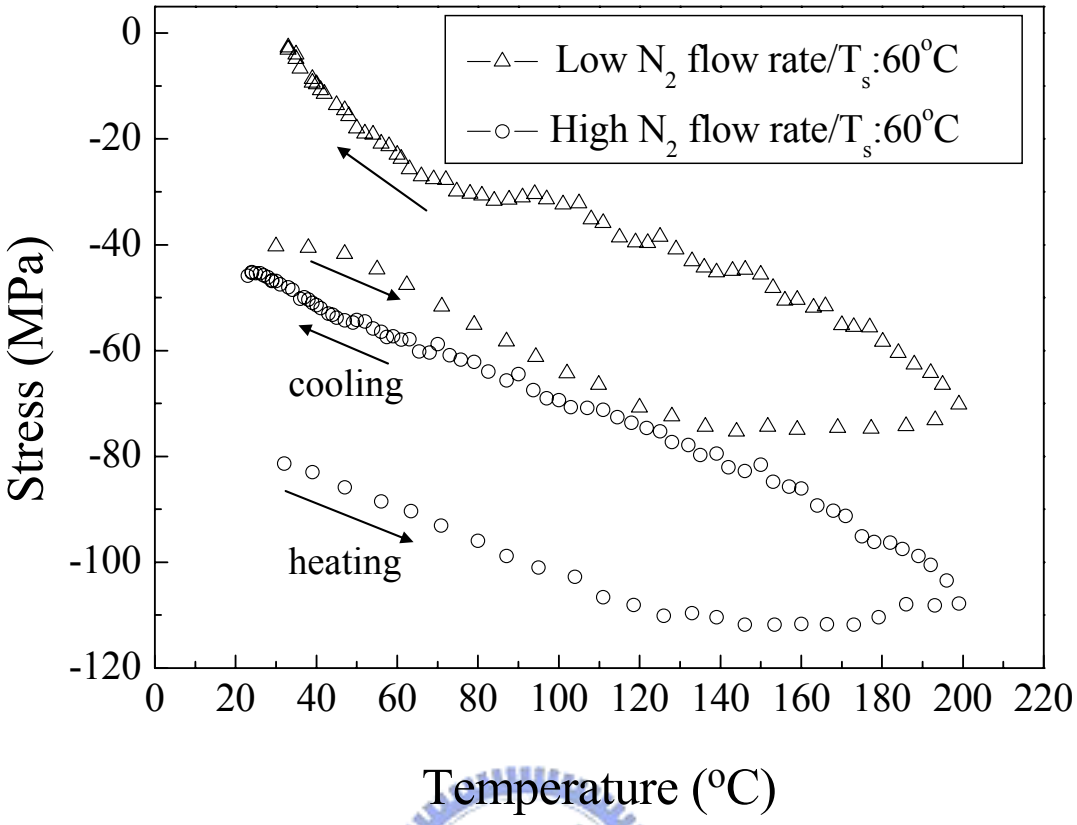
Low N2 flow rate/Ts:60°C
High N2 flow rate/Ts:60°C
cooling
heating
Stress (MPa)
Temperature (°C)
0
-20
-40
-60
-80
-100
-120
0
20
40
60
80
100
120
140
160
180
200
220

(a)

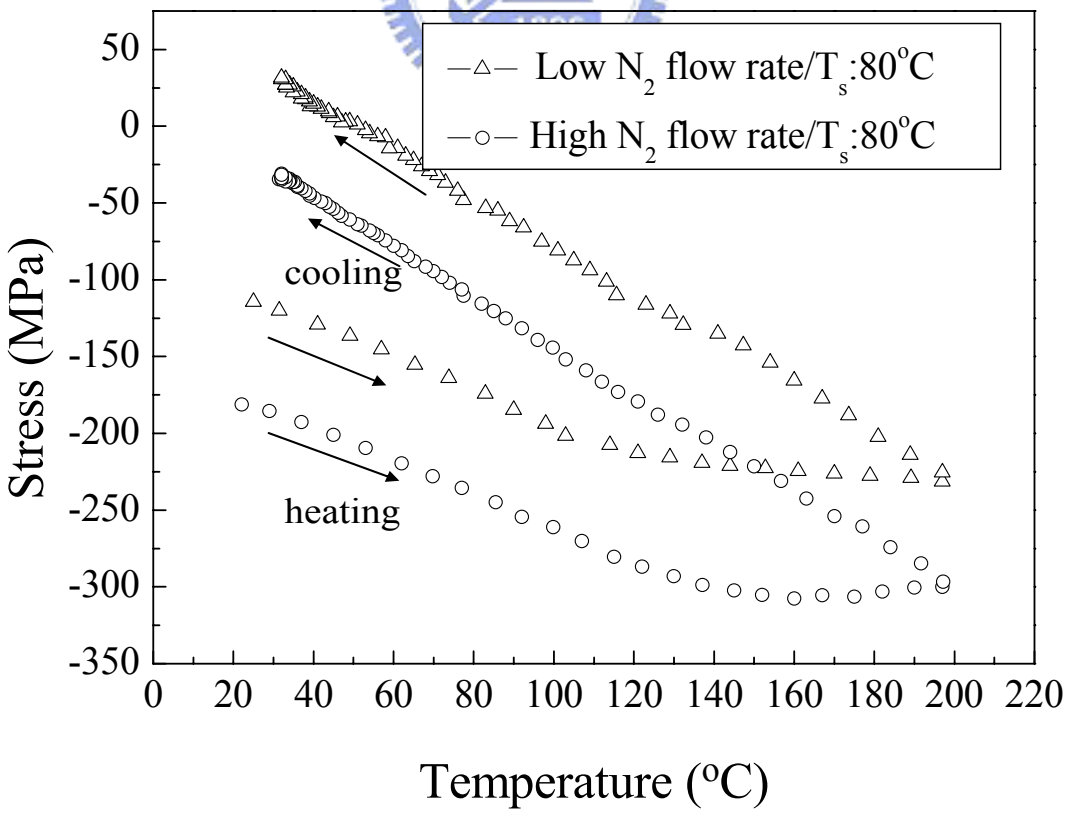
Low N2 flow rate/Ts:80°C
High N2 flow rate/Ts:80°C
cooling
heating
Stress (MPa)
Temperature (°C)
50
0
-50
-100
-150
-200
-250
-300
-350
0
20
40
60
80
100
120
140
160
180
200
220

(b)

Figure 4.16 Stress vs. annealing temperature of 50nm SiO_xN_y/200 nm Al films with different SiO_xN_y deposition conditions: (a) △ stood for the SiO_xN_y film which was deposited under low gas flow rate and 60℃. ◇ stood for the SiO_xN_y film which was deposited under high gas flow rate and 60℃. (b) △ stood for the SiO_xN_y film which was deposited under low gas flow rate and 80℃. ◇ stood for the SiO_xN_y film which was deposited under high gas flow rate and 80℃.

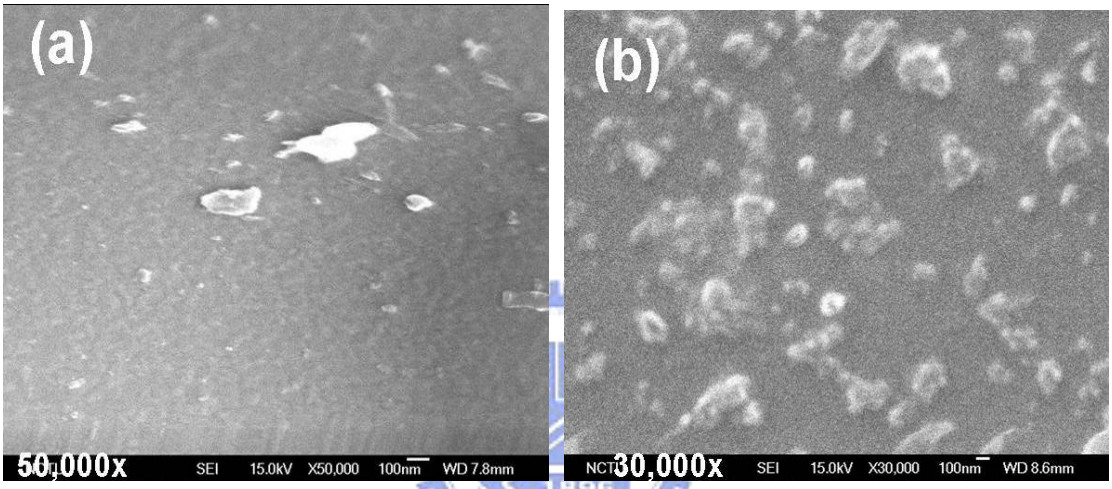

Figure 4.17 SEM top-view graphs of the SiO_xN_y films after 200℃ thermal cycle: (a) films deposited under 60℃ (b) films deposited under 80℃.

4.7 Discussion

4.7.1 Microstructure and Moisture of Barrier Layer

The microstructure of the developing film would be characterized by the shape of its grain structure. The grain structure would be affected by the growing environment such as substrate temperature, surface roughness, chamber pressure, the cleanliness levels, etc. [9, 40-42] In general, lower substrate temperature tended to form a film with lower density and more defects such as grain boundaries or pinhole due to the poor surface diffusion, which in turn would greatly affect the water vapor permeation. [26] In this case, barrier layers were all exhibited amorphous phase by

TEM. Hence, there were not grain boundaries in barrier layers and also no obvious pinhole observed by SEM. Pinhole defects were widely considered to be the main moisture permeation way. [26, 59] But more recent studies have shown that there are still permeation problems after eliminating pinhole defects. [60] Therefore, there may have other moisture permeation paths to be further studied.

4.7.2 Hillock Formation

In this thesis study, hillocks can be found even at low temperature (60 ^{o}C), which was not expected initially. Previously, hillock was formed only at high temperature, such as 300-400 ^{o}C. [61-64] There were three possible reasons that hillock could be formed under such low temperature; namely: (1) relatively small grain size in the as-deposited Al films, (2) high grain boundary migration in pure Al film, and (3) Al surface temperature of 247-361 ^{o}C imparted by the evaporated molecules and atoms.

Since hillock defects were observed for all the samples in this study, and their densities were further quantified using an Al wet etch method to decorate hillock defects. Excellent correlation between hillock density and moisture permeation through SiO_xN_y/Al samples was established, indicating Al hillock was the culprit of moisture permeation in the passivation layer.

4.7.2.1 Mechanisms of Hillock Formation

Hillocks were first observed in aluminum metallization in the semiconductor devices during deposition processing and widely discussed in the past forty years. [61-64] Hillock growth could cause metal shorting and the device breakdown. Therefore, it has been critical to understand its formation mechanism and solutions. Hillocks could be explained as extrusions or protrusions on the surface of a metallic

film. The cause of hillock formation was the existence of compressive stress in the metallic thin films as shown in Fig. 4.18. There were two kinds of hillocks, one was named growth hillock which was generated by intrinsic stress during deposition [65, 66] and the other was named annealing hillock which was due to the different thermal expansion coefficients between films and substrates when experiencing high temperature annealing process. [67-69] Hillocks were formed to relax the compressive stress.

There have been many studies and publications discussing the mechanisms about hillock formation, such as interfacial diffusion, [70] surface diffusion [71] and grain-boundary diffusion. [72-74] It was clear that diffusion played an important role in hillocking regardless the specific mechanism preciously described. In addition, the formation of hillock density and its size were also discussed. [69, 72, 74] There were two opposing view to be described below.

Iwamura *et al.* [69] proposed a model as shown in Figs. 4.19 (a)-(c). Hillocks formed on the surface as shown in Fig. 4.19 (a), which was driven and formed as result of lateral diffusion along grain boundaries for a film consisting of small grains.

Subsequently, new hillocks might grow at the edges of old hillocks as shown in Fig. 4.19 (b). For Al film with large grain sizes such as columnar structures shown in Fig. 4.19 (c), hillocks tended to be formed at the grain boundary triple points near the surface through vertical diffusion because it was more difficult for lateral diffusion in a columnar structure. Overall, smaller grains resulted in larger hillocks with low density, while larger grains yielded smaller hillocks with higher density. Furthermore, one can predict that hillock density is higher for a columnar structure with small grain size.

However, Kim *et al.* [72] and Zaborowski *et al.* [73] proposed a different view

on the hillock size and density. Both found the decrease of the hillock density and increase of hillock size as grain size [72, 73] or film thickness [73] increased.

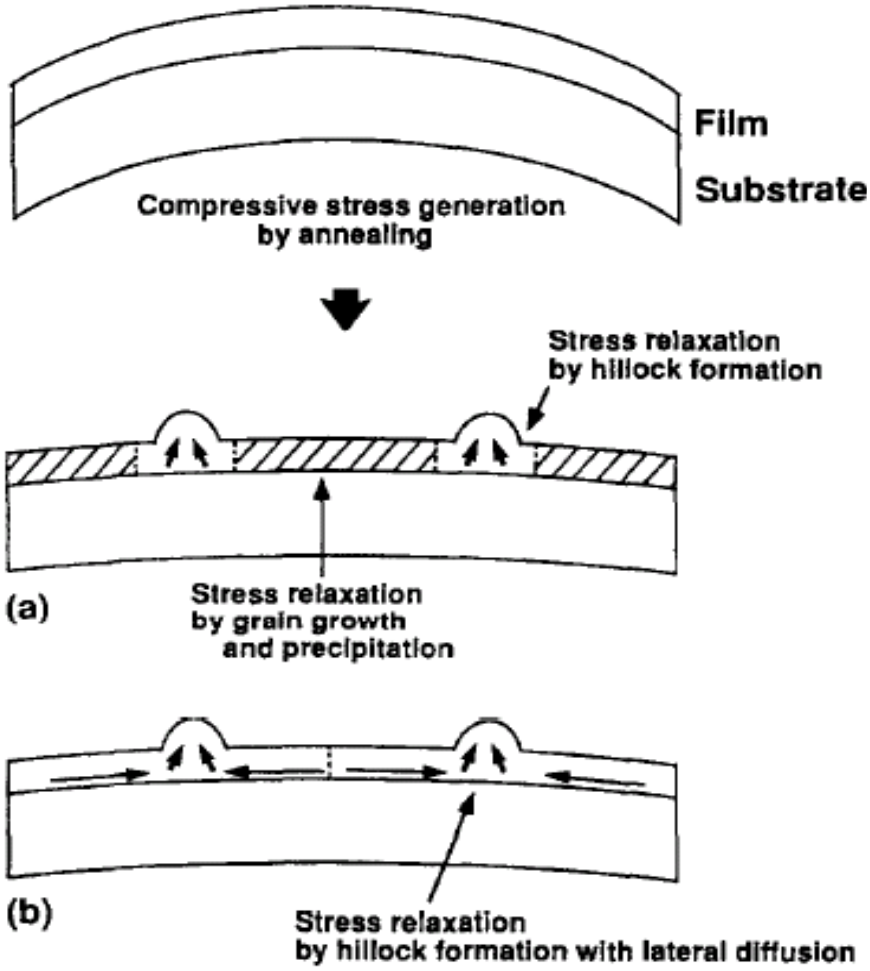

Figure 4.18 Schematic diagrams of two models correlating to the hillock formation behavior on Al thin films. [69]

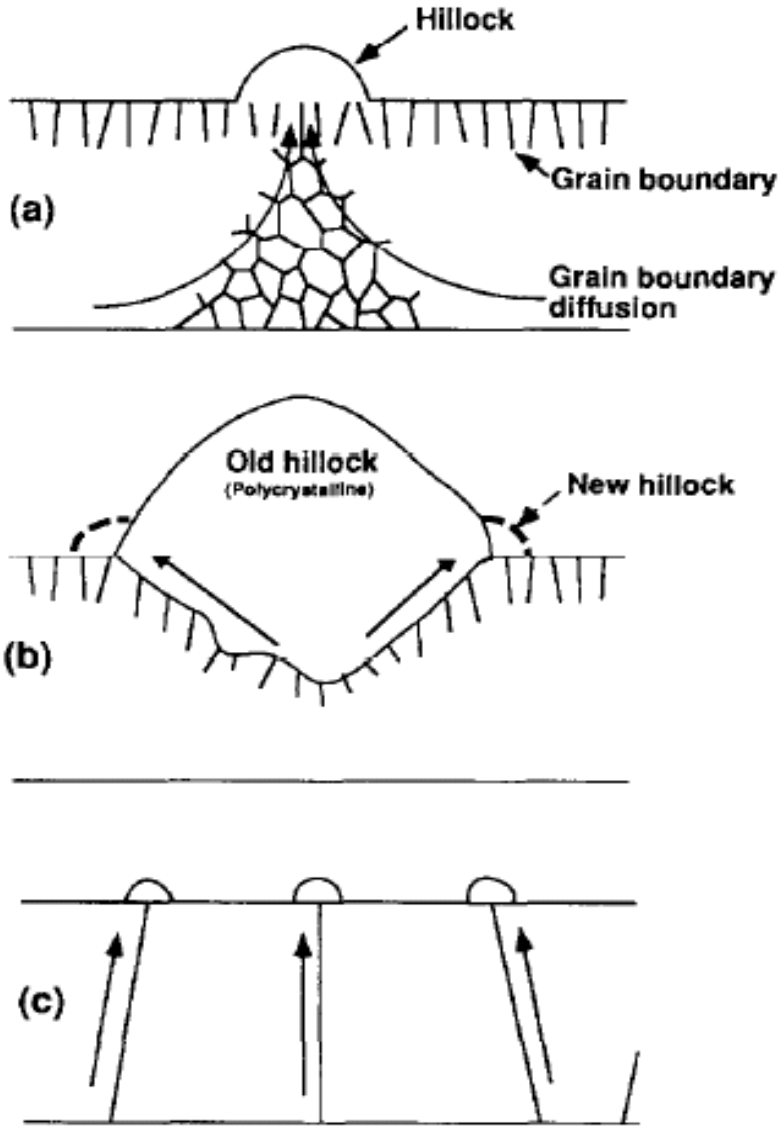

Figure 4.19 Schematic diagrams of hillock formation comparing a film with small grains to a film with large grains. [69]

4.7.2.2 Defects Caused by Stress

Fig. 4.20 illustrated two inhomogeneous deformations, either by dislocation slip or by grain-boundary sliding, to cause the passivation fracture and this sample stack was commonly present in one part of integrated circuit structure which involved a passivation or dielectric layer, such as SiO_2 and Si_3N_4, deposited on the metal layer, such as copper and aluminum. These unwanted plastic deformations occurred if the stress in the passivation thin film was too high. If the tensile stress was too high, it would result in passivation thin film cracking. If the compressive stress was too high, it would result in hillock formation extruding out of the passivation thin film. Both scenarios led to structural failure. As one of these fractures occurred in integrated circuit, it could cause electrical shorts if two metallization layers were forced to come into contact. If these failures occurred in OLED's package, it would create a wide pathway for moisture permeation and result in poor moisture resistance. Water vapor transmission rate through this pathway would be higher than the other permeation ways, such as grain boundaries, pinholes, pores, etc. The effect of stress will be discussed in the subsequent sections.

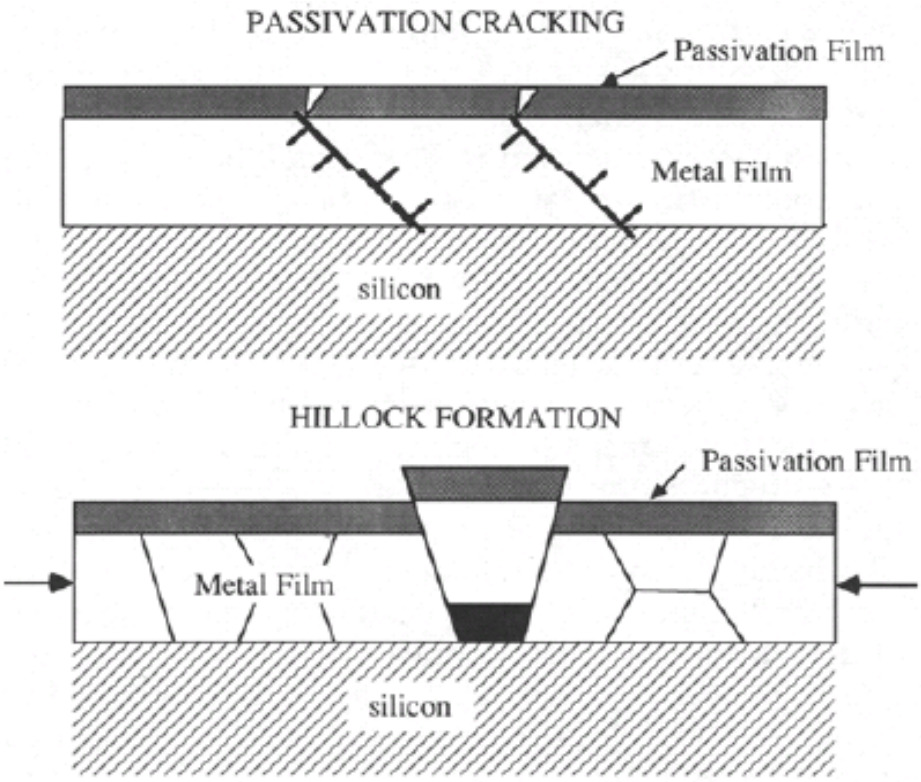

Figure 4.20 Illustration of thin film failure by the thin film stress. [10]

4.7.2.3 Suppression of Hillocking

The relevant research in recent years pointed out that adding some alloying elements in the metal thin film could improve the intensity of thin film and be able to stand more compressive stress produced during the annealing process, and then suppress the hillock growth in the thin film. [68, 69] On the one hand adding some alloying elements in the metal film can prevent dislocations from moving, and on the other the alloying elements would segregate in the grain boundaries to suppress grain growth. Both the phenomena could suppress the hillock formation.

4.7.3 Hillock Density vs. Grain Boundary

There have been many publications on this issue with quite different points of view as described in Chapter 4.7.2.1. In this study, hillock density of the sample and the corresponding Al grain size was summarized in Table 4.10. It showed SiO_xN_y/Al samples prepared at low temperatures possessed small grain size, and more grain boundaries. It meant the difference in hillock density was related to its grain boundary density, which was proportioned to grain boundary triple points, the most probable sites for hillock nucleation. And this view point was consistent with those proposed by Kim *et al.* [72] and Zaborowski e*t al.*'s. [73]

Table 4.10 Hillock density of the sample and the corresponding Al grain size.

	Hillock density ($10^{-5}/\mu m^2$)	**Al grain size (nm)**
High flow rate_80℃	34.6	58
Low flow rate_80℃	40.8	57
High flow rate_60℃	41.4	41
Low flow rate_60℃	74.8	37

4.7.4 Hillock Height vs. Stress

According to the experimental data listed in Table 4.11, the as-deposited SiO_xN_y stress was related to hillock height. The larger compressive stress yielded the higher hillock height. Therefore, SiO_xN_y/Al samples prepared at high substrate temperature and high N_2 gas flow rate deposition process resulted in higher stress in the passivation layer, in turn higher hillock height. SiO_xN_y films deposited under higher substrate temperature conditions yielded larger compressive stress than under lower

substrate temperature conditions due to the different thermal stress. Films deposited under high flow rate conditions yielded larger compressive stress than under low flow rate conditions due to the different N atomic content.

Table 4.11 As-deposited stress of the multilayer and the corresponding hillock height.

	As-deposited stress (MPa)	Hillock height (nm)
High flow rate_80℃	-180	54
Low flow rate_80℃	-114	38
High flow rate_60℃	-80	35
Low flow rate_60℃	-40	25

4.7.5 Model of Hillock Formation in SiO_xN_y/Al/glass for OLED Applications

Al films were first deposited onto glass at 60 ^oC, which corresponded to Al surface temperature of 250 ^oC. At this stage, Al film on glass exhibited a columnar structure with grain size 40-60 nm. Since pinhole defects and grain boundaries were likely introduced in the Al electrode during low-temperature deposition, a SiO_xN_y layer was deposited onto Al electrode to passivate it. In this study, amorphous SiO_xN_y films were formed on Al/glass substrates under various deposition conditions such as N_2 gas flow rates and substrate temperatures. Moreover, the hillock defects were believed to extrude through the passivation layer and degrade the moisture permeation drastically. Subsequently, moisture could permeate through Al films through the pinhole defects or grain boundaries into the underlying OLDE device resulting black

spots in the display. Hence, Al hillock was found to be the culprit of moisture permeation in the SiO_xN_y/Al stack.

The energy derived from SiO_xN_y deposition at 60-90 ^oC, which corresponded to 247-361 ^oC at Al surface, induced further grain growth in the underlying Al film. SiO_xN_y films prepared under high substrate temperature and high flow rate onto Al/glass substrate showed the lowest Al hillock density, but possessed the tallest Al hillock defects height. The difference in hillock density was related to its grain boundary density. Hence, small Al grain sizes with high grain boundary density yielded high hillock density. In contrast, large Al grain sizes with low grain boundary density resulted in low hillock density. In addition, hillock height was related to passivation thin film stress. Hillock height was proportional to the stress of passivation thin film. Hillock formation led to relieving the existing stress in thin films. SiO_xN_y films prepared under high substrate temperature and high flow rate initially produced the largest thin film stress and yielded the highest hillock height. Moreover, the shortest hillock was formed when the lowest stress relief was achieved.

A hillock formation model in SiO_xN_y/Al stack based on the above experimental results was proposed and illustrated in Figs. 4.21 (a), (b) and (c). Al films were first deposited onto glass substrate at 60 ^oC shown in Fig. 4.21 (a). As-deposited Al films possessed a columnar structure with grain size 40-60 nm. Then, SiO_xN_y barrier films deposited onto Al/glass substrate at low temperature could be illustrated by Fig. 4.21 (b). The surface temperature of Al film during SiO_xN_y deposition was estimated to be ~247 ^oC, which induced further Al grain growth to sizes in the ranges of 40-80 nm. The as-deposited stress was compressive, -40 to -80 MPa, which was relatively low as compared to that deposited at high temperature. As a result, SiO_xN_y films deposited at low temperature yielded high hillock density because of smaller grain sizes with more grain boundaries, and short hillock height due to lower level of compressive stress.

SiO_xN_y barrier films deposited onto Al/glass substrate at high temperature could be described by Fig. 4.21 (c). The surface temperature of Al film during SiO_xN_y deposition was estimated to be ~361°C, which induced further Al grain growth to sizes in the ranges of 60-140 nm. The as-deposited stress was compressive, -141 to -180 MPa, which was relatively high as compared to that deposited at low temperature. As a result, SiO_xN_y films deposited at high temperature yielded low hillock density due to relative large Al grain sizes driven by higher Al surface temperature, and tall hillock height because of high level of compressive stress.

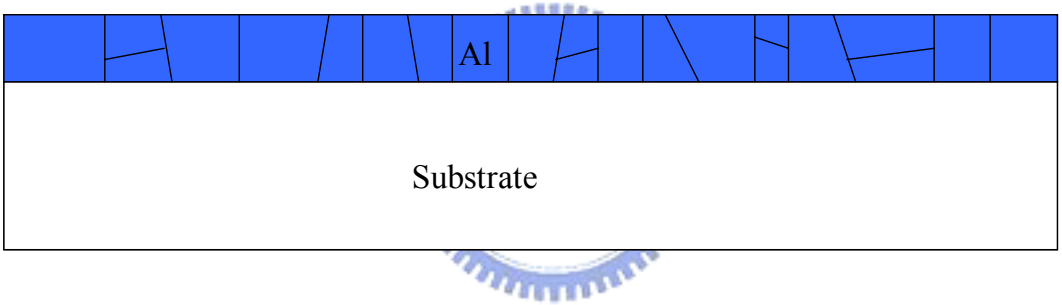

(a)

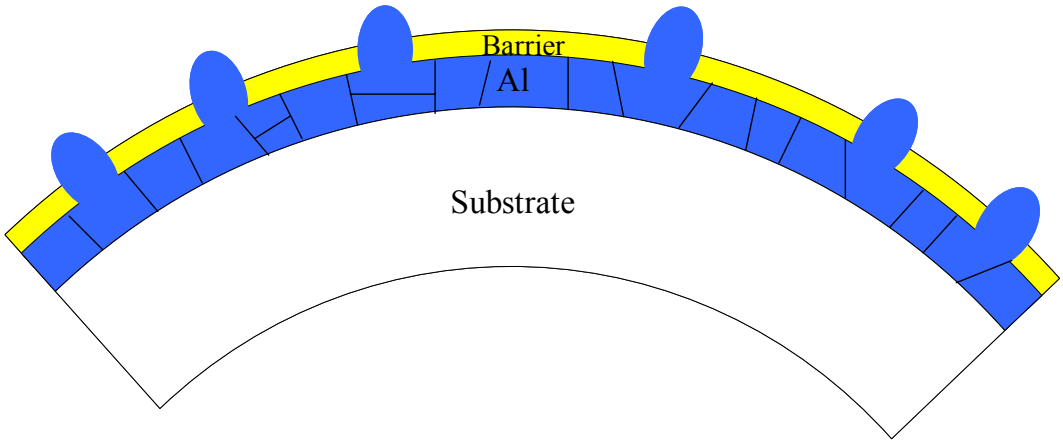

(b)

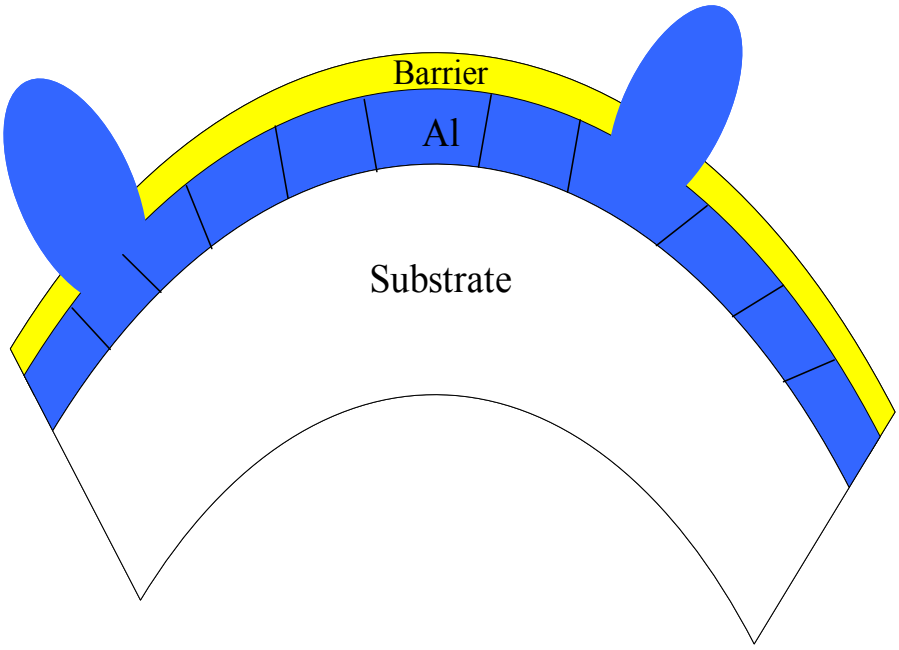

(c)

Figure 4.21 The model of hillock formation: (a) sample prepared under the same deposition conditions of Al films (b) barrier films deposited under low temperature caused less Al grain growth with lowest stress, shortest hillock height and highest hillock density (c) barrier films deposited under high temperature caused more Al grain growth with largest stress, tallest hillock height and lowest hillock density.

Chapter 5 Conclusions

The composition, microstructure and morphology of SiO_xN_y barrier and Al layers deposited by a modified Ar ion beam evaporation system were investigated as a function of substrate temperatures and gas flow rates. Furthermore, the impact of defects and stress on the moisture permeation in the inorganic SiO_xN_y/Al stack were studied for their correlation. Al films deposited at 60 ^oC exhibited a columnar structure with grain size 50-100 nm. Since pinhole defects and grain boundaries were likely introduced in the Al electrode during low-temperature deposition, an amorphous SiO_xN_y passivation layer was deposited onto Al electrode. It was found that Al hillock was formed even at low temperature, such as 60 ℃ because of its high purity of Al films and small grains. During the deposition of SiO_xN_y passivation layer, the energy imparted by evaporated atoms and molecules raised the Al surface temperature to 250-361 ^oC resulting in further Al grain growth. Moreover, SiO_xN_y films prepared under high substrate temperature and high flow rate showed the lowest Al hillock density, but possessed the tallest Al hillock height. Excellent correlation between hillock density and moisture permeation through SiO_xN_y/Al samples was established, indicating Al hillock was the culprit of moisture permeation in the passivation layer.

A model of hillock formation in SiO_xN_y/Al was proposed in this thesis to illustrate the causes for their difference in hillock density and height. The hillock density related to the initial Al grain size, while the hillock height was primarily derived by SiO_xN_y stress. The tallest height of hillock affected greatly on the numbers of barrier layers for complete sealing of defects. Therefore, high substrate temperature and high N_2 gas flow rate deposition process yielded barrier films with less hillocks and improved moisture resistance if single layer of passivation was employed, while

lower deposition temperature and low N_2 gas flow rate were preferred for least number of layers if multiple-layer structure was adopted. In summary, defect control of Al hillocks was essential for controlling the moisture barrier performance in the practical OLED stack.

References

[1] C. H. Chen, OLED/Organic Electroluminescent Materials and Devices, Wunan, Taipei (2005).

[2] H. Aziz and Z. D. Popovich, Chem. Mater. **16**, 4522 (2004).

[3] P. Melpignano and A. Baron-Toaldo, Appl. Phys. Lett. **86**, 041105 (2005).

[4] P. E. Burrows, V. Bulovic, S. R. Forrest, L. S. Sapochak, D. M. McCarty, and M. E. Thompson, Appl. Phys. Lett. **65**, 23 (1994).

[5] M. S. Weaver, L. A. Michalski, K. Rajan, M. A. Rothman, J. A. Silvernail, J. J. Brown, P. E. Burrows, G. L. Graff, M. E. Gross, P. M. Martin, M. Hall, E. Mast, C. Bohnam, W. Bennett, and M. Zurnhoff, Appl. Phys. Lett. **81**, 2929 (2002).

[6] P. E. Burrows, G. L. Graff, M. E. Gross, P. M. Martin, M. K. Shi, M. Hall, E. Mast, C. Bonham, W. Bennet, and M. B. Sullivan, Displays **22**, 65 (2001).

[7] Barix™, Vitex Systems Inc., 3047 Orchard Parkway, San Jose, CA 95134.

[8] P. E Buows, G. L. Graffa, M. E. Gross, P. M. Martin, M. Hall, E. Mast, C. Bonham, W. Bennett, L. Michalskit, M. Weaver, J. J. Brown, D. Fogartyc, and L. S. Sapochak, Proc. SPIE **4105**, 75 (2001).

[9] J. A. Thornton, Ann. Rev. Mater. Sci. **7**, 239 (1977).

[10] W. D. Nix, Metall. Trans. A **20A**, 2217 (1989).

[11] D. S. Gardner and P. A. Flinn, IEEE Trans. Devices **ED-35**, 2160 (1988).

[12] S. Miyata and S. Nalwa, Organic Electroluminescent Materials and Devices, Gordon and Breach, Japan (1997).

[13] H. Aziz, Z. D. Popovic, S. Xie, A. M. Hor, N. X. Hu, C. Tripp, and G. Xu, Appl. Phys. Lett. **72**, 756 (1998).

[14] Y. Sato and H. Kanai, Mol. Cryst. Liq. Cryst. **253**, 143 (1994).

[15] F. Papadimitrakopoulos, X. M. Zhang, D. L. Thomsen, and K. A. Higginson,

Chem. Mater. **8**, 1363 (1996).

[16] J. McElvain, H. Antoniadis, M. R. Hueschen, J. N. Miller, D. M. Roitman, J. R. Sheets, and R. L. Moon, J. Appl. Phys. **80**, 6002 (1996).

[17] M. Schaer, F. Nüesch, D. Berner, W. Leo, and L. Zuppiroli, Adv. Funct. Mater. **11**, 2 (2001).

[18] H. Aziz and G. Xu, J. Phys. Chem. B **101**, 4009 (1997).

[19] H. C. Langowski, in 46th Annual Technical Conference Proceedings of the Society of Vacuum Coaters, San Francisco, CA, 559 (2003).

[20] G. Nisato, P. C. P. Bouten, P. J. Slikkerveer, W. D. Bennett, G. L. Graff, N. Rutherford, and L. Wiese, Proc. Asia Display/IDW01, 1435 (2001).

[21] R. Paetzold, A. Winnacker, D. Henseler, V. Cesari, and K. Heuser, Review of Scientific Instruments **74**, 12 (2003).

[22] R. Dunkel, R. Bujas, A. Klein, and V. Horndt, Journal of Society for Information Display **13**, 7 (2005).

[23] John McMahon，「Barix技術帶來OLED顯示器的性能和應用突破」，電子工程專輯，2003年11月。

[24] K. M. Harris, M. F. Hogge, and D. E. Jones, U.S. Patent 105906 (2002).

[25] S. Q. Shi, H. C. Lee, and C. P. Wei, U.S. Patent 6888632 (1996).

[26] A. S. da Silva Sobrinho, G. Czeremuszkin, M. Latreche, and M. R. Wertheimer, J. Vac. Sci. Technol. A **18**,149 (2000).

[27] A. S. da Silva Sobrinho, N. Schuhler, J. E. Klemberg-Sapieha, M. R. Wertheimer, M. Andrews, and S. C. Gujrathi, J. Vac. Sci. Technol. A **16**, 2021 (1998).

[28] B. M. Henry, A. G. Erlat, A. McGuigan, C. R. M. Grovenor, G. A. D. Briggs, Y. Tsukahara, T. Miyamoto, N. Noguchi, and T. Niijima, Thin Solid Films **382**, 194 (2001).

[29] G. L. Graff, M. E. Gross, J. D. Affinito, M. K. Shi, M. Hall, and E. Mast, U.S.

Patent 6522067 (2003).

[30] T. G. Krug, Proc. 33th Soc. Vacuum Coaters Annual Conference, 163 (1990).

[31] M. Izu, B. Dotter, and S. R. Ovshinski, Proc. 36th Society of Vaccuum Coaters Annual Conference, 333 (1993).

[32] M. Schaepkens, T. W. Kim, A. G. Erlat, M. Yan, K. W. Flanagan, C. M. Heller, and P. A. McConnelee, J. Vac. Sci. Technol. A, **22**, 1716 (2004).

[33] A. G. Erlat, B. M. Henry, J. J. Ingram, C. R. M. Grovenor, G. A. D. Briggs, R. J. Chater, and Y. Tsukahara, J. Phys. Chem. B **108**, 883 (2004).

[34] S. Takeda, M. Fukawa, Y. Hayashi, and K. Matsumoto, Thin Solid Films **339**, 220 (1999).

[35] R. M. Barrer, Diffusion In and Through Solids, Cambridge University Press, New York (1941).

[36] B. E. Deal and A. S. Grove, J. Appl. Phys. **36**, 3770 (1965).

[37] M. Yanaka, B. M. Henry, A. P. Roberts, C. R. M. Grovenor, G. A. D. Briggs, A. P. Sutton, T. Miyamoto, Y. Tsukahara, N. Takeda, and R. J. Chater, Thin Solid Films **397**, 176 (2001).

[38] P. B. Barna and M. Adamik, Thin Solid Films **317**, 27 (1998).

[39] I. Petrov, P. B. Barna, L. Hultman, and J. E. Greene, J. Vac. Sci. Technol. A **21**, 5 (2003).

[40] R. Messier, A. P. Giri, and A. R. Roy, J. Vac. Sci. Technol. A **2**, 500 (1984).

[41] C. R. M. Grovenor, H. T. G. Hentzell, and D. A. Smith, Acta Metall. **32**, 773 (1984).

[42] D. A. Smith and A. Ibrahim, Mater. Res. Soc. Proc. **317**, 401 (1994).

[43] V. Bulovic, P. Tian, P. E. Burrows, M. R. Gokhale, S. R. Forrest, and M. E. A. Thompson, Appl. Phys. Lett. **70**, 2954 (1997).

[44] S. Han, X. Feng, Z. H. Lu, D. Johnson, and R. Wood, Appl. Phys. Lett. **82**, 715

(2003).

[45] L. S. Hung, C. W. Tang, M. G. Manson, P. Raychaudhuri, and J. Madathil, Appl. Phys. Lett. **74**, 544 (2001).

[46] T. Matsue, T. Hanabusa, Y. Ikeuchi, K. Kusaka, and O. Sakata, Vacuum **80**, 836 (2006).

[47] J. D. Plummer, M. D. Deal, and P. B. Griffin, Silicon VLSI Technology, Prentice Hall, New Jersey (2000).

[48] B. D. Cullity and S. R. Stock, Elements of X-ray Diffraction, Prentice-Hall, New Jersey (2001).

[49] W. C. Oliver and G. M. Pharr, J. Mater. Res. **7**, 1564 (1992).

[50] P. R. Griffiths and J. A. deHaseth, Fourier Transform Infrared Spectrometry, Wiley, New York (1986).

[51] J. C. Vickerman, Surface Analysis: The Principle Techniques, John Wiley & Sons, New York (1997).

[52] G. Stoney, Proc. R. Soc. London, Ser. A **82**, 172 (1909).

[53] A. Gladkikh, Y. Lereah, E. Glickman, M. Karpovski, A. Palevski, and J. Schubert, Appl. Phys. Lett. **66**, 10 (1995).

[54] A. F. Jankowski, J. P. Hayes, T. E. Felter, C. Evans, and A. J. Nelson, Thin Solid Films **420**, 43 (2002).

[55] P. Temple-Boyer, B. Hajji, J. L. Alay, J. R. Morante, and A. Martinez, Sensors and Actuators **74**, 52 (1999).

[56] F. Rebib, E. Tomasella, M. Dubois, J. Cellier, T. Sauvage, and M. Jacquet ,Thin Solid Films **515**, 3480 (2007).

[57] http://rsb.info.nih.gov/ij/

[58] J. A. Taylor, Appl. Surf. Sci. **7**, 168 (1981).

[59] H. Chatham, Surf. Coat. Technol. **78**, 1 (1996).

[60] A. G. Erlat, R. J. Spontak, R. P. Clarke, T. C. Robinson, P. D. Haaland, Y. Tropsha, N. G. Harvey, and E. A. Vogler, J. Phys. Chem. B **103**, 6047 (1999).

[61] F. d'Heurle, L. Berenbaum, and R. Rosenberg, Trans. Metall. Soc. AIME **242**, 502 (1968).

[62] D. S. Herman, M. A. Schuster, and R. M. Gerber, J. Vac. Sci. Technol. **9**, 15 (1971).

[63] A. J. Learn, J. Vac. Sci. Technol. B **4**, 3 (1986).

[64] A. F. Puttlitz, J. G. Ryan, and T. D. Sullivan, IEEE Trans. on Components Hybrids and Manufacturing Technol. **12**, 619 (1989).

[65] C. Y. Chang and R. W. Vook, J. Vac. Sci. Technol. A **9**, 559 (1991).

[66] R. AberMann, Thin Solid Films **186**, 233 (1990).

[67] U. Smith, N. Kristensen, F. Erison, and Jan-Ake Schweitz, J. Vac .Sci. Technol. A **9**, 2527 (1991).

[68] T. Ohnishi, E. Iwamura, and K. Takagi, J. Vac. Sci. Technol. A **15**, 2339 (1997).

[69] E. Iwamura, T. Ohnishi, and K. Yoshikawa, Thin Solid Films **270**, 450 (1995).

[70] P. Chaudhari, J. Appl. Phys. **45**, 4339 (1974).

[71] C. Y. Chang and R. W. Vook, Thin Solid Films **228**, 205 (1993).

[72] D. K. Kim, W. D. Nix, R. P. Vinci, M. D. Deal, and J. D. Plummer, J. Appl. Phys. **90**, 781 (2001).

[73] M. Zaborowski, M. Adamiec, and A. Barcz, Appl. Surf. Sci. **91**, 246 (1995).

[74] S. J. Hwang, J. H. Lee, C. O. Jeongb, and Y. C. Joo, Scripta Mater. **56**, 17 (2007).